Minimize the Aerodynamic Effect of a Strut on the Wing

Optimization of Strut-Braced Wing Configuration for Conceptual Design using Low-fidelity CFD Models and Optimization Algorithms

Master's thesis in Mobility Engineering

ANDRES FELIPE SANTOS BLAIR
MERT UTKU

DEPARTMENT OF MECHANICS AND MARITIME SCIENCES

CHALMERS UNIVERSITY OF TECHNOLOGY
Gothenburg, Sweden 2023
www.chalmers.se

Master's thesis 2023

Minimize the Aerodynamic Effect of a Strut on the Wing

Optimization of Strut-Braced Wing Configuration for Conceptual Design using Low-fidelity CFD Models and Optimization Algorithms

ANDRES FELIPE SANTOS BLAIR & MERT UTKU

CHALMERS
UNIVERSITY OF TECHNOLOGY

Department of Mechanics and Maritime Sciences
Division of Fluid Dynamics
Chalmers University of Technology
Gothenburg, Sweden 2023

Minimize the Aerodynamic Effect of a Strut on the Wing
Optimization of Strut-Braced Wing Configuration for Conceptual Design using Low-fidelity CFD Models and Optimization Algorithms
ANDRES FELIPE SANTOS BLAIR & MERT UTKU

Supervisor: Alexandre Antunes, Heart Aerosapce AB
Examiner: Carlos Xisto, Department of Mechanics and Maritime Sciences

Master's Thesis 2023
Department of Mechanics and Maritime Sciences
Division of Fluid Dynamics
Chalmers University of Technology
SE-412 96 Gothenburg
Telephone +46 31 772 1000

Cover: Picture of the ES-30.

Typeset in LaTeX
Printed by Chalmers Reproservice
Gothenburg, Sweden 2023

Minimization of the Aerodynamic Effect of a Strut on the Wing
ANDRES FELIPE SANTOS BLAIR & MERT UTKU
Department of Mechanics and Maritime Sciences
Chalmers University of Technology

Abstract

The field of aircraft design is continuously advancing through the utilization of scientific techniques and empirical methods. The incorporation of computational methods has facilitated the design process of new and complex aircraft, enabling more efficient conceptual design and optimization. These advancements have the potential to significantly reduce fuel consumption and emissions, making a positive impact on the environment, a critical global concern. The development of battery-electric airplanes represents a significant step towards creating a more sustainable aviation sector. Among the various emerging concepts, the Strut-Braced Wing (SBW) has shown great promise in enhancing aerodynamic efficiency while reducing wing weight.

However, the implementation of new concepts and technologies also presents new challenges and limitations that must be addressed, particularly the impact of aerodynamics on the aircraft's range, which can impose limitations on its maximum travel distance. The primary objective of this thesis is to minimize the aerodynamic effects of a strut and wing configuration by reducing total drag and increasing the Oswald efficiency of the Strut-Braced Wing during the conceptual design phase.

To achieve this goal, Sequential Quadratic Programming (SQP) and Genetic Algorithm (GA) optimization algorithms are employed, utilizing low-fidelity Computational Fluid Dynamics (CFD) methods. The airfoil data utilized in the study is obtained from the XFOIL tool, which provides important viscous aerodynamic characteristics.

By implementing these methodologies, it is anticipated that the aerodynamic performance of the Strut-Braced Wing configuration can be optimized, leading to improved efficiency and weight reduction. The results obtained from this research will contribute to the advancement of aircraft design and promote the development of more environmentally friendly and efficient aircraft during the conceptual design phase.

Keywords: SBW, CFD, aerodynamics, optimization, SLSQP, SGA, VLM, weight estimation

Acknowledgements

First and foremost, we would like to extend our heartfelt thanks to the Heart Aerospace team for their unwavering support and for providing us with the opportunity to collaborate on this master's thesis. Their guidance and collaboration have been invaluable throughout the entire process.

We would also like to express our deep appreciation to Alexandre Antunes, our supervisor, for his exceptional advice, guidance, and expertise during this thesis work. His extensive knowledge has played a pivotal role in our personal and professional growth. We are grateful to have had the privilege of working with him and for making this journey both enjoyable and enlightening.

Furthermore, we extend our warmest gratitude to our examiner, Carlos Xisto, for his invaluable guidance and support during these past months. His insightful feedback has greatly contributed to the quality of our work.

We also want to express our sincere thanks to Chalmers University of Technology and all the professors who have educated and nurtured us over the past two years. Their dedication and passion for teaching have made this journey both enjoyable and intellectually stimulating.

Finally, we want to offer a special heartfelt thank you to our family and friends for their unconditional support and belief in us. Her şey için teşekkür ederim. ¡Gracias a todos los que me acompañaron en este viaje!

In conclusion, we are immensely grateful to everyone who has contributed to our academic journey and made it a truly enriching experience. Thank you for your unwavering support, and for making this adventure fun and captivating!

Andres Felipe Santos Blair & Mert Utku, Gothenburg, June 2023

List of Acronyms

Below is the list of acronyms that have been used throughout this thesis listed in alphabetical order:

2D	Two dimensional
3D	Three dimensional
AC	Aerodynamic Center
ARAC	Aviation Rulemaking Advisory Committee
AoA	Angle of Attack
AVL	Anthena Vortice Lattice
BMX	Bending moment in x axis
CO_2	Carbon Dioxide
CAD	Computer-Aided Design
CFD	Computational Fluid Dynamics
CoP	Center of Pressure
EASA	European Union Aviation Safety Agency
FN	Surface Forces file
FS	Strip Forces file
FT	Total Forces file
FVM	Finite Volume Method
GA	Genetic Algorithm
HWB	Hybrid Wing Body
I/O	Input - Output
IATA	International Air Transport Association
JSON	JavaScript Object Notation
LE	Leading Edge
LLT	Lifting Line Theory
MAC	Mean Aerodynamic Chord
MGC	Mean Geometric Chord
MTOW	Maximum Take-Off Weight
NACA	National Advisory Committee for Aeronautics
NASA	National Aeronautics and Space Administration
N-S	Navier-Stokes
OOP	Object Oriented Programming
RANS	Reynolds-averaged Navier–Stokes equations
SBW	Strut Braced Wing

SGA	Simple Genetic Algorithm
SLSQP	Sequential Least Squares Programming
TE	Trailing Edge
VLM	Vortex Lattice Method
WS	Wing-Strut

Nomenclature

Below is the nomenclature of parameters,variables and coefficients that have been used throughout this thesis.

Lowercase greek letters

α	Angle of attack
α^*	Angle of attack value for non-linear behaviour in C_l vs AoA graph
α_ϕ	Shift value for cambered airfoils in Angle of attack axis
γ	Strut dihedral angle
η_z	Ultimate load factor
θ	Angle between pressure vector and the shear stress vector angle vs chord line
λ	Taper ratio
λ_W	Wing taper ratio
μ	Freestream dynamic viscosity
ν	Kinematic viscosity
ρ	Density
ρ_∞	Freestream density
τ	Shear stress
τ_l	Shear stress in the airfoil's lower surface (2D)
τ_u	Shear stress in the airfoil's upper surface (2D)

Uppercase greek letters

Γ	Circulation
Λ	Sweep angle

$\Lambda_{c/4}$	Sweep angle at quarter MAC

Lowercase latin letters

a	Speed of sound
a	Axial force in airfoil (2D)
a_l	Axial force in the airfoil's lower surface (2D)
a_u	Axial force in the airfoil's upper surface (2D)
b	Span
c	Chord
c_{root}	Chord in the wing root
c_{tip}	Chord in the wing tip
c_{MGC}	Mean geometric chord
d	Drag force in airfoil (2D)
e	Oswald efficiency factor
l	Lift force in airfoil (2D)
m	Moment in airfoil (2D)
n	Normal force in airfoil (2D)
n_l	Normal force in the airfoil's lower surface (2D)
n_u	Normal force in the airfoil's upper surface (2D)
p	Static pressure
p_∞	Freestream static pressure
p_l	Static pressure in the airfoil's lower surface (2D)
p_u	Static pressure in the airfoil's upper surface (2D)
q	Dynamic pressure
q_∞	Freestream dynamic pressure
s	Distance alongside airfoil's surface from the LE
s_l	Distance alongside airfoil's lower surface from the LE
s_u	Distance alongside airfoil's upper surface from the LE
r	Resultant force in airfoil (2D)
t	Thickness
t	Time
t	Parametric value for Bezier curve
t/c	thickness/chord ratio

y	Spanwise axis
y	Position in spanwise axis
y_{motor_1}	Spanwise location of motor 1
y_{motor_2}	Spanwise location of motor 2

Uppercase latin letters

A	Axial force in body (3D)
AoA	Angle of Attack
A_{inc}	Incidence angle
AR	Aspect ratio
AR_W	Wing aspect ratio
C_d	Drag coefficient (2D)
C_f	Skin friction coefficient (2D)
C_l	Lift coefficient (2D)
C_m	Moment coefficient (2D)
C_p	Pressure coefficient
C_r	Resultant force coefficient (2D)
C_D	Drag coefficient (3D)
C_{D_i}	Induced drag coefficient
C_{D_f}	Skin friction drag coefficient
$C_{D_{ff}}$	Induced drag from Trefftz plane analysis
$C_{D_{tot}}$	Total drag coefficient
$C_{D_{vis}}$	Viscous drag coefficient
C_L	Lift coefficient (3D)
C_{L_ϕ}	Shift value for cambered airfoils in lift coefficient axis
C_M	Moment coefficient (3D)
C_R	Resultant force coefficient (3D)
D	Drag force in body (3D)
D_n	Drag force for the n-th body (3D)
E	Young‘s modulus
F	Factor for secondary structures
I	Geometrical inertia
K	Effective length factor

L	Lift force in body (3D)
L	Strut length
M	Mach number
M	Moment in body (3D)
M_∞	Freestream Mach number
M_{local}	Local Mach number
N	Normal force in body (3D)
O	Sample space
P_0	Left control point for bezier curve construction
P_1	Middle control point for bezier curve construction
P_2	Right control point for bezier curve construction
P_{0_x}	Left control point horizontal coordinate for bezier curve construction
P_{1_x}	Middle control point horizontal coordinate for bezier curve construction
P_{2_x}	Right control point horizontal coordinate for bezier curve construction
P_{0_y}	Left control point vertical coordinate for bezier curve construction
P_{1_y}	Middle control point vertical coordinate for bezier curve construction
P_{2_y}	Right control point vertical coordinate for bezier curve construction
P_{cr}	Critical load for buckling
R	Resultant force in body (3D)
Re	Reynolds number
$S_{i,n}$	Cell in the i-th row and n-th column in the LHS cell matrix
S_{ref}	Reference area
S_W	Wing reference area
T	Target space
V	Flow velocity
V	Volume
V_∞	Freestream flow velocity
W	Weight
W_0	Maximum Take-Off Weight
W_{FW}	Fuel stored in wing weight

W_{motor_1}	Weight of motor 1
W_{motor_2}	Weight of motor 2
W_{FW}	Fuel stored in wing weight
W_W	Wing weight
X_i	Input variables
Y_n	n-th strata in LHS method

Contents

List of Figures

List of Tables

1
Introduction

This master's thesis was conducted in collaboration between Chalmers University of Technology and Heart Aerospace, a Swedish aviation startup with the goal of electrifying regional air travel. The collaboration lasted for five months. This chapter provides a brief background and description of the problem and aims of the study. Additionally, the section defines the specific airplane type that is the focus of this work.

Heart Aerospace ES-30 is a reserve-hybrid airplane designed for commercial short-haul flights [1]. The aircraft is specifically designed to accommodate short takeoff and landing operations in regions with complex topography and short runways and is capable of performing steep approaches. Furthermore, ES-30 is a high-wing, T-tailed airplane with strut-braced wings. Such configuration is commonly used for this type of aircraft [2]. The airplane will be certified under Aviation Safety Agency (EASA) CS-25 certification standards. The focus of this thesis, written for Heart Aerospace, is to create and analyze a generic optimization process for wing-strut configuration design.

1.1 Background

The aviation industry is constantly evolving, but it faces a significant challenge in reducing its carbon footprint to address the global climate crisis. Commercial air travel has been steadily increasing over the years, with projections indicating continued growth in the future, despite the impact of the COVID-19 pandemic as seen in Figure 1.1. Unfortunately, this growth is expected to lead to higher CO_2 emissions as shown in Figure 1.2, with short-haul flights accounting for a significant portion of these emissions [3].

Studies show that 2% of all man-made CO_2 emissions are generated by the aviation industry [4]. To address this challenge, the International Air Transport Association (IATA) and National Aeronautics and Space Administration (NASA) have set ambitious goals to reduce global net aviation carbon emissions by 50% by 2050 relative to 2005 as indicated in Figure 1.3. Some countries, such as Sweden and Norway, have even more ambitious targets [3, 5, 6].

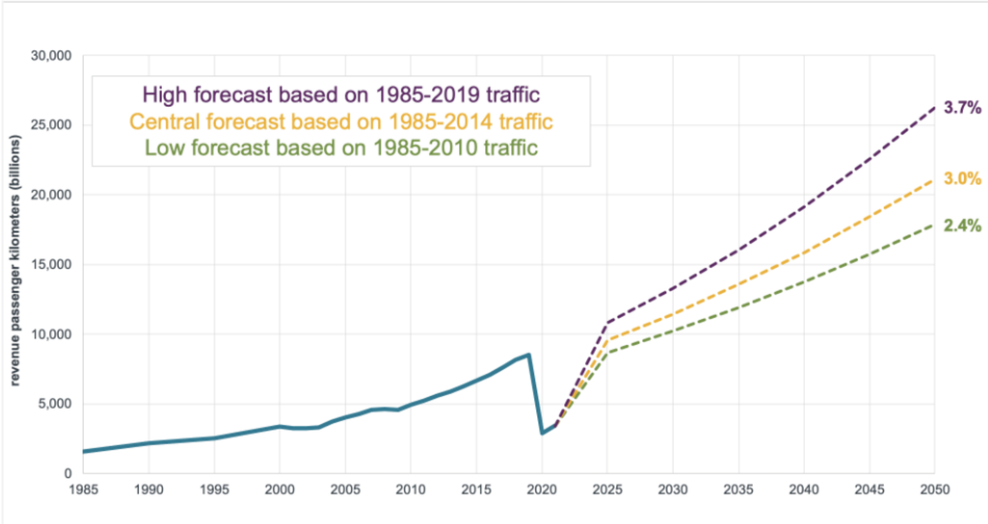

Figure 1.1: Air Travel between 1985-2050 [3]

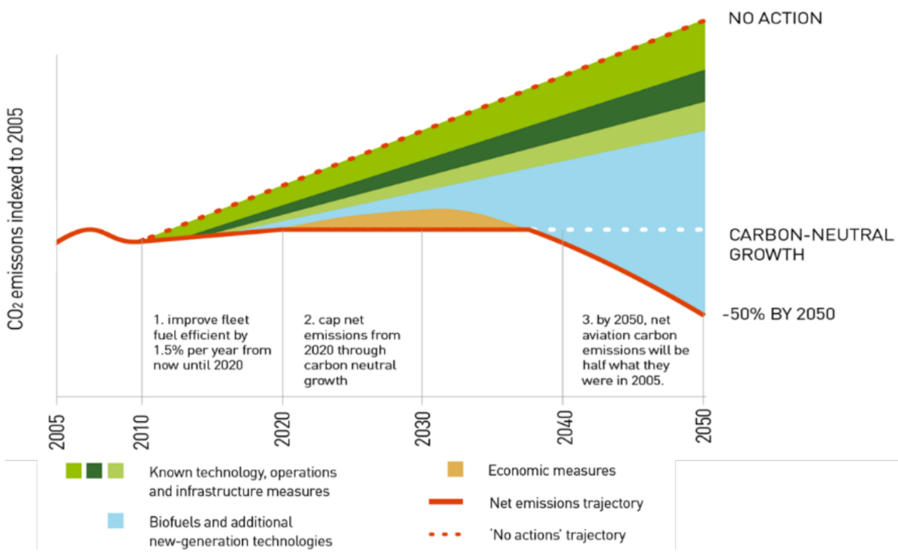

Figure 1.2: CO_2 emissions between 2005-2050 [7]

Corners of the Trade Space	N+1 (2005 Entry Into Service) Generation Conventional Tube and Wing (Relative to B737/CFM56)	N+2 (2020 Initial Operating Capability) Generation Unconventional Hybrid Wing Body (Relative to B777/GE90)	N+3 (2030 -2035 Service Entry) Advanced Aircraft Concepts (Relative to User -Defined Reference)
Noise (Cum Below Stage 4)	-32 dB	-42 dB	-71 dB
LTO NOx Emissions (Below CAEP 6)	-60%	-75%	Better than -75%
Performance: Aircraft Fuel Burn	-33%	-40%	Better Than -70%
Performance: Field Length	-33%	-50%	Exploit Metroplex Concepts

Figure 1.3: CO_2 emission goals for 2050 [8]

In this context, new technologies and concepts are crucial to achieving these goals. The IATA predicts that they will contribute 13% to the route to net-zero emissions as can be observed in Figure 1.4. One of the promising solutions to achieve low emissions and high performance for regional flights in the aviation industry is electric aircraft.

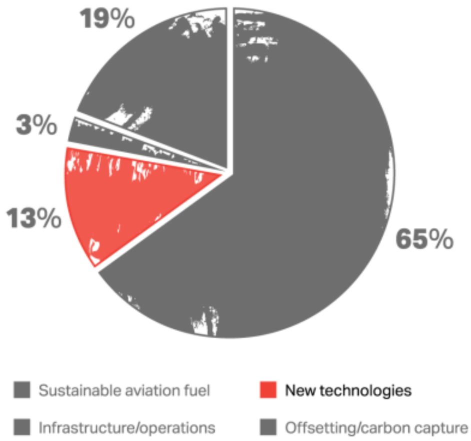

Figure 1.4: Expected contribution of new technologies in CO_2 emissions [3]

In recent years, various designs have emerged with the goal of reducing fuel consumption, emissions, and noise, in line with the target of achieving net-zero emissions by 2050 or NASA's HR2454 Goals [9]. IATA has summarized different concepts under 'The Revolutionary Aircraft Technologies', which includes innovative designs such as Joined Wings (Box Wing), Hybrid Wing Body, and Strut-braced wings [3] as seen in Figure 1.5, Figure 1.6 and Figure 1.7. This thesis will concentrate on the Strut-braced wings design concept, which has the potential to bring a step-change in sustainability for the aviation industry, especially in the transonic flow regime.

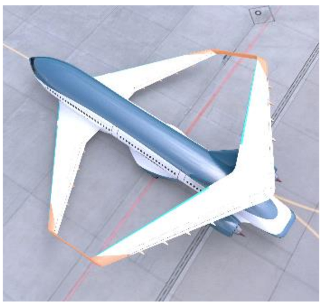

Figure 1.5: Joined Wings (Box Wing) configuration [3]

Figure 1.6: Hybrid Wing Body configuration designed by DLR [3]

Figure 1.7: Strut-braced Wing designed by NASA/Boeing [3]

1.1.1 Strut-braced wings

Improving the aerodynamic efficiency of the aircraft leads to reductions in fuel consumption, emissions, and noise [10]. One approach to improve aerodynamic efficiency is through the design of a high aspect ratio wing. Previous studies have shown that increasing the aspect ratio can reduce induced drag by up to 75% [20]. However, high aspect ratio wings imply higher bending moments as the wings are longer. Engineers are faced with a trade-off between increasing stiffness, which would result in a heavier wing, or adopting a wing-strut configuration to decrease the bending moment. The maximum bending moment using a wing-strut configuration can lead to a reduction of up to 50% experienced by the wing when compared to an equivalent cantilever wing.[11].

The design of strut-braced wings has a long history in aviation, dating back to the Hurel-Dubois HD-31 aircraft in 1956 which utilized strut-braced wings to achieve higher aerodynamic efficiency, as can be seen in Figure 1.8. At first, designers favored wing-bracing over wing-box design. However, the use of wing-braced concept resulted in an increase in profile drag from the struts, leaving space for the development of the wing-box concept with thicker profiles to define the wing shape.

Figure 1.8: Hurel-Dubois HD31 [12]

In recent years, strut-braced wings have once again gained attention as a way to improve efficiency by increasing the aspect ratio of the wing while maintaining a lower thickness which allows for decreasing wave drag and induced drag. This reduction in wave drag during transonic flight, combined with a lower sweep angle and natural laminar flow, leads to improved overall efficiency [13]. Moreover, the lighter weight of strut-braced wings which can reach a decrease of 70% in comparison with cantilever wings [20], and the advancements in computational power and numerical methods, have enabled the optimization of these wings for both transonic and subsonic flight. As a result, there has been a trend towards the use of strut-braced wings in subsonic flights to reduce induced drag with higher aspect ratios and improve fuel efficiency towards net-zero emission goals [14, 15]. Moreover, strut-braced wings have certification benefits in CS 25.25 Weight Limits and CS25.305 Strength and deformation [16]. The Aviation Rulemaking Advisory Committee (ARAC) has issued a report on a new airframe crash-worthiness rule that mandates adequate fuselage resistance to loads during emergency landings or survivable crash events [17]. A Wing-Strut configuration can help satisfy this certification requirement, as the struts distribute the load onto the fuselage and prevent the structural deformation caused by the wing, as illustrated in Figures 1.9 and 1.10.

Figure 1.9: ATR-42 FAA drop test [18]

Figure 1.10: Shorts 3-30 FAA drop test [19]

Prior research has shown that various methods can be used for the aerodynamic analysis of wing-strut configurations, including semi-empirical formulas [20, 21], low-to-medium fidelity models [13], high-fidelity models [15, 22, 23], and multi-fidelity methods [24]. While high-fidelity methods are capable of capturing flow separations and details, they are computationally expensive and their accuracy is relatively more sensitive to mesh quality than low-fidelity methods, as discussed in Section 4.3. On the other hand, low-fidelity methods are generally less accurate in capturing details and separations but still provide accurate results depending on the simulation objective. Additionally, during the conceptual or preliminary design phase of an aircraft, design variables are not fully defined, and investing significant engineering time in high-fidelity methods may not be practical since the design is not mature enough. Therefore, in the optimization process of this thesis, low-fidelity methods have been utilized, as they offer a time-efficient and reliable approach to achieving the objective described in Section 1.2.

1.2 Objective

The objective of this Master's thesis project is to explore various integration strategies for implementing a Wing-Strut configuration while reducing the computational cost of designing strut-braced wings. An optimization process has been established using low-fidelity methods for airfoils and planforms, a panel method with a transition model to include viscous effects for the former, and Vortex-Lattice method for the latter. Such a combination sets the aerodynamic analysis tool for the optimization process. The optimization process employs both gradient-based algorithms and stochastic algorithms, to achieve the best results. The optimization process will be conducted using XFOIL [25], AVL [26], and the SciPy [27] library module for optimization algorithms in the Python programming language [28]. The optimization process will be implemented in Python, and the results will be evaluated against the design requirements. To assess the effectiveness of the low-fidelity tool, the optimization process was compared to high-fidelity tools available in the market using a generic wing as a benchmark. The optimization process considered various constraints and factors, with the objective of achieving the most optimal and realistic wing, while maximizing the benefits of the strut-braced wing concept within the given scope. The ultimate goal is to achieve increased aerodynamic efficiency, decreased weight, and reduced fuel consumption, thereby aligning with sustainability goals.

1.3 Scope

This thesis focuses on the investigation and optimization process of wing-strut configurations for aircraft operating in subsonic flow regime conditions during the conceptual design phase. The study is limited to a duration of five months, which affected the complexity of the defined variables, constraints, and optimization algorithms. Additionally, due to cost in terms of time constraints, high-fidelity RANS simulations were not included. However, the investigation and optimization conducted in this study are adequate for the conceptual design phase. This thesis provides valuable insights into the design and optimization process of wing-strut configurations, which can inform future research in this area.

2

Theory

2.1 Fluid dynamics

2.1.1 Governing equations

The governing equations are fundamental equations used to describe the motion of fluids. The accuracy of the numerical solutions obtained from solving these equations depends on the underlying assumptions and theoretical frameworks employed.

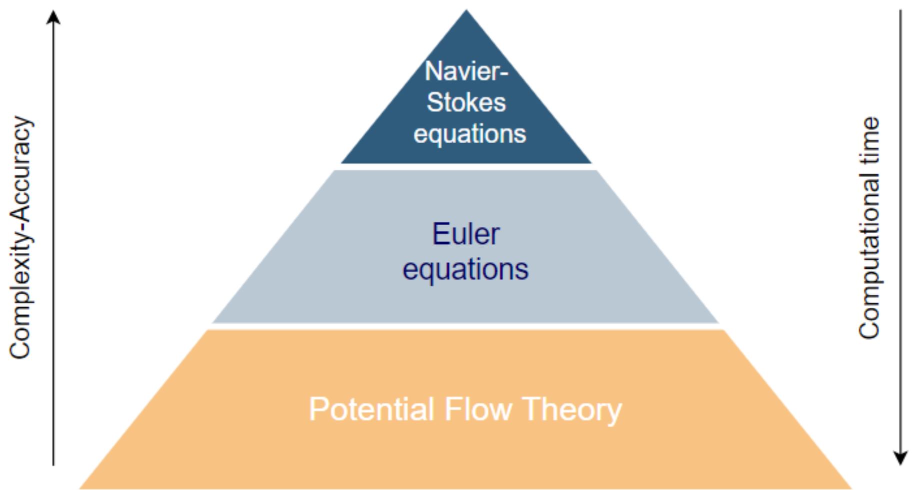

Figure 2.1: Comparison of different governing equations

2.1.1.1 Navier-Stokes

Velocity and pressure field are found with Navier Stokes equations where the flow is incompressible. Continuity equation is given in [29, Equation 2.1] which ensures the mass conservation.

$$\frac{\partial v_i}{\partial x_i} = 0 \tag{2.1}$$

The momentum equation as index notation is given in [29, Equation 2.2] for constant viscosity (incompressible).

$$\frac{\partial v_i}{\partial t} + \frac{\partial v_i v_j}{\partial x_j} = -\frac{1}{\rho}\frac{\partial p}{\partial x_i} + \nu \frac{\partial^2 v_i}{\partial x_j \partial x_j} \tag{2.2}$$

Where x_i and v_i are the positions and velocity in the direction i, ρ is density, ν is the kinematic viscosity, and p is the static pressure.

Euler equations are the Navier-Stokes equations with inviscid assumption.

2.1.1.2 Potential Flow theory

Potential flows use the inviscid Euler equations, along with irrotational assumptions, which state that the flow velocity is equal to the gradient of the velocity potential as shown in equation 2.3.

$$\vec{V} = \nabla\phi \tag{2.3}$$

The main idea behind potential flow theory is to calculate the forces acting on a given geometry by modelling the circulation using the velocity potential ϕ [30, 31]. The circulation Γ is defined as the closed loop integral of velocity over the geometry. The continuity equation, also known as Laplace's equation, is given as:

$$\nabla^2\Phi = 0 \tag{2.4}$$

The velocity potential can be solved numerically by implementing the boundary conditions. These boundary conditions ensure that the flow does not penetrate the geometry and that the velocity normal to the surface is zero [31].
The circulation can be converted into a force by using the Kutta-Joukowski theorem, as shown in equation 2.5.

$$L = \rho_\infty V_\infty \times \Gamma \tag{2.5}$$

Where L is the Lift force, v_∞ is the free stream velocity and Γ is the circulation.

Potential flow theory is valid in situations where vorticity is not important, such as in thin boundary layers or where there are no wakes. Additionally, the theory does not consider viscous effects due to the inviscid assumption, which assumes no viscous drag over the geometry [30].

Furthermore, the Kutta condition is enforced to ensure that the solution has a "physical sense." The Kutta condition states that an airfoil creates lift by deflecting the flow, which adds a velocity field to the free-stream velocity. The deflection of the flow is such that the total flow should leave the trailing edge smoothly.

For more details and an extensive explanation of the methodology, refer to [30] and [32]. The sections below will focus on the applicability of these methods.

2.1.2 Subsonic flow and compressiblity

The fluid flow can be separated into five regimes due to free-stream Mach number and local Mach number as seen in Table 2.1.

Flow regime	Description
Incompressible	$M_\infty < 0.3$
Subsonic	$M_\infty < 1$ and $M < 1$
Transonic	case 1: $M_\infty < 1$ and $M > 1$ locally case 2: $M_\infty > 1$ and $M < 1$ locally
Supersonic	$M_\infty > 1$ and $M > 1$
Hypersonic	$M_\infty > 5$ and $M > 5$

Table 2.1: Flow regimes for compressible flow [33].

Mach number is defined as in equation 2.6

$$M = \frac{V}{a} \tag{2.6}$$

Where V is local velocity, a is the speed of sound as a function of flow density, temperature, and molar gas constant.

2.1.3 Reynolds number

Free stream Reynolds number is defined as :

$$Re = \frac{\rho_\infty V_\infty c}{\mu_\infty} \tag{2.7}$$

Where c is the reference length, μ_∞ is the freestream dynamic viscosity, ρ_∞ is the freestream density, V_∞ is the freestream velocity. Typically, the reference length for the airfoil is the chord for lifting bodies.

Reynolds number symbolizes the ratio between the inertial forces and viscous forces.

2.2 Numerical Models

Various methods exist to predict the aerodynamic performance of a wing, each with different levels of complexity and accuracy. It is crucial to choose a methodology that matches the required accuracy for a given phase in the development process. For example, during the conceptual phase, the selected methodology should keep up with the design changes and ensure accuracy.

Most of the commercial finite volume codes are based on Navier-Stokes (N-S) equations, providing the ability to analyze fully described fluid flow. However, using N-S based finite volume tools comes at a higher computational cost compared to low-fidelity methods.

2.2.1 Low-fidelity models

Low-fidelity methods mentioned in this Section are based on Potential Flow theory.

2.2.1.1 Vortex sheet and horseshoe vortex

The concept of a vortex sheet plays a big role in the analysis of flow around airfoils and finite wings. A vortex sheet contains an infinite number of straight vortex filaments with infinitesimally small strength. A vortex filament is a line with the same strength (Γ) along it, and the filament's tangent vector is aligned with the direction of the local vorticity vector. According to Hermann von Helmholtz's theorem, the circulation (Γ) of a vortex filament is constant through time, and the vortex filament should end up at a solid surface or in a closed form. Therefore, Helmholtz's theory suggests that there will be the presence of tip vortices and induced drag in a three-dimensional fluid flow, but in a two-dimensional fluid flow, there will be no tip vortices and no induced drag [30, 32, 34].

A vortex filament is fixed in location and experiences a force due to the Kutta-Joukowski theorem (bounded vortex). For this reason, Prandtl modified a wing with a bounded vortex, where the length of the vortex is equal to the span. However, the vortex filament should be continued with two free vortices that move fluid elements through the flow. The shape that contains a bounded vortex and two free vortices is named a horseshoe vortex, as seen in Figure 2.2.

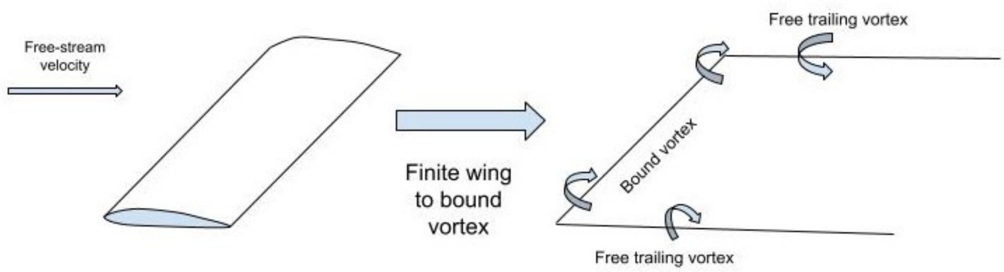

Figure 2.2: Replacement of finite wing with horseshoe vortex

2.2.1.2 Lifting Line theory

Lifting Line Theory (LLT) is a three-dimensional application of potential flow theory, incorporating multiple horseshoe vortices to predict the spanwise lift distribution across the wing as seen in Figure 2.3. The circulation is modeled as a velocity potential in the horseshoe vortices using the Biot-Savart law [30]. The strength of the trailing vortex is directly proportional to the variation in circulation along the lift line [30]. The trailing edge vortices create downwash which reduces circulation in the spanwise direction, resulting in a non-uniform spanwise lift distribution as circulation must be conserved along the wing [31].

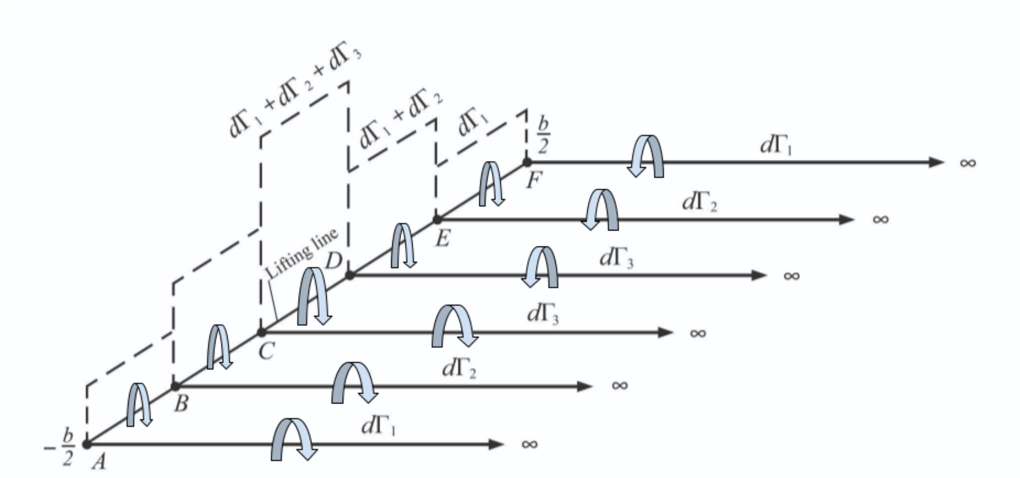

Figure 2.3: Superposition of a finite number of horseshoe vortices along the lifting line. Source: [30]

2.2.1.3 Vortex Lattice Method (VLM)

In VLM, the geometry is discretized with quadratic panels by dividing it into finite spanwise and chordwise elements. Each panel has a ring or horseshoe vortex that enables analysis of the camber, sweep, and dihedral of the wing, which is not possible with LLT as the wing is modeled as a straight lift line [31]. Additionally, VLM allows for the calculation of moment coefficients by determining the pressure distribution over the wing [30]. The panels in VLM are placed on the mean chamber line, which means that if the static pressure distributions on the suction and pressure side are of interest, VLM cannot capture this effect. The wake is created using only chordwise vortices, as the spanwise vortices are not effective downstream through the trailing edge [30]. The strength of the trailing vortices is defined by the trailing edge vortices and remains constant in the longitudinal direction [30]. The total lift force is calculated by adding up the lift force in each panel. The main limitations of VLM are that trailing vortices should not intersect with other vortices, and panels should not intersect with each other. AVL [26] and OpenVSP [35] are some of the commercial tools that use the VLM method [32].

Trefftz plane analysis is an alternative method for calculating induced drag, which provides more accurate results than the wake integral method [26]. Trefftz plane analysis calculates induced drag by tracing the wake from far downstream while integrating kinetic energy. More information and details about Trefftz plane analysis can be found in [26, 36, 37]. AVL uses Trefftz plane analysis to calculate induced drag as an alternative method.

Moreover, AVL uses slender body theory, which enables the modelling of the fuselage, unlike other commercial VLM solvers. Further details about slender body theory are not introduced in this chapter, as the point of interest of this thesis is the Wing and Wing-strut combination. More details about slender body theory can be found in [37, 38].

2.2.1.4 3D Panel Method

The 3D panel method is an advanced form of VLM that covers the entire geometry (including top and bottom surfaces) with panels, enabling it to capture thickness changes through the chord in airfoils. In thicker airfoils, thickness across the chord and camber have a significant effect on the static pressure distribution, which can be captured in panel methods but not in VLM [31]. Additionally, the panel method allows the modelling of the fuselage, which also generates lift. However, as with VLM, the panels in panel methods must not coincide [32].

2.2.1.5 Viscous Drag Prediction with XFOIL

XFOIL is a popular well-known tool for analyzing airfoil characteristics, particularly for low Reynolds number flows. It utilizes the panel method coupled with a boundary layer subroutine with transition prediction [39]. The software incorporates 2D Boundary Layer Integral equations as a transition model, which can capture turbulence and laminar separation bubbles [40]. This enables XFOIL to calculate the pressure distribution over the airfoil [40]. In addition, XFOIL can estimate limited trailing edge flow separation and predict the maximum lift coefficient [25]. The software also separates skin friction drag and pressure drag contributions for a given airfoil [25].

2.2.1.6 Summary of low-fidelity models

The VLM method has a huge advantage in conceptual design due to its low computational cost and relative ease of adapting to geometry changes compared to CAD and high-fidelity CFD. These two factors make VLM suitable for optimization in the conceptual design phase. However, the VLM method cannot model viscous effects, which is its main limitation. As a result, VLM tools cannot capture boundary layer effects and wing stall. In AVL, the VLM method can be extended with skin friction correlations and form factors for viscous drag. However, this extension still cannot fully capture the effect of boundary layer and viscous drag. To address this limitation, the extension can be made with interpolation of viscous drag from two-dimensional flow codes such as XFOIL.

2.2.2 High-fidelity models

In this section, high-fidelity models refer to those based on the numerical solution of Navier-Stokes equations in discretized form using computational mesh. These models are capable of capturing complex flow phenomena such as turbulence, boundary layer effects, and flow separation, but they are computationally expensive and require significant computational resources.

2.2.2.1 Finite Volume Method (FVM)

The governing equations shown in Section 2.1.1 are discretized with Finite Volume Method (FVM). Moreover, differencing scheme is utilized to calculate the convective and diffusive effects that result from neighboring cells for the cell that is considered in the computation. Furthermore, a pressure-velocity coupling is needed as the pressure term is only found in momentum equation but velocity is found in both of the equations.

2.3 Geometric Parameters

As stated in Chapter 1, the wing-strut design is the core of this thesis, as all the parametric studies were carried out for a particular setup of both surfaces. In this section, the relevant concepts and parameters will be covered and briefly explained to the reader.

2.3.1 Airfoil

The most relevant geometric parameters for this surface will be briefly introduced to the reader, as explained by [39, 41, 43]. Figure 2.4 depicts an NACA6409 airfoil, exhibiting the specified parameters.

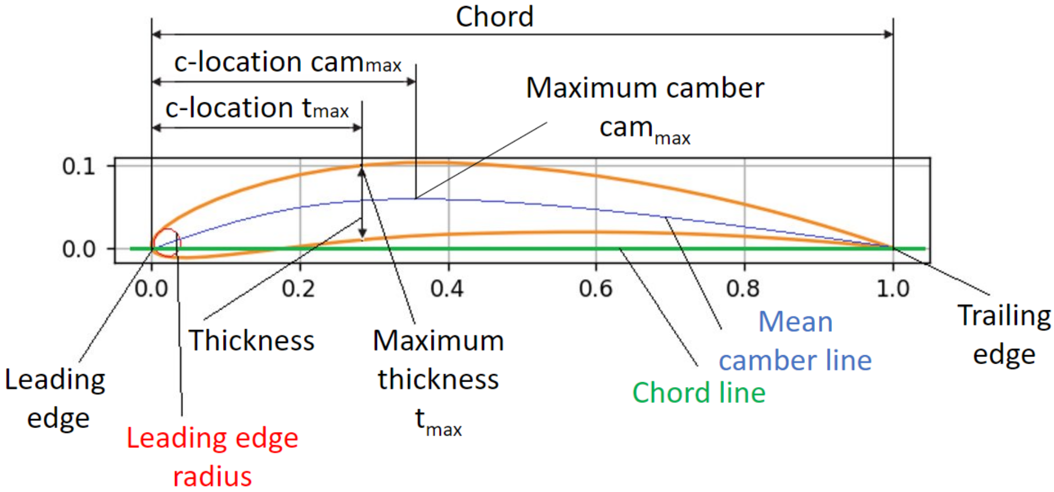

Figure 2.4: Airfoil geometric parameters.

- **Leading Edge:** is the foremost point of an airfoil. It serves as the reference point for the coordinate system used to define the airfoil geometry.
- **Trailing Edge:** is the after-most point of an airfoil.
- **Chord (chordline):** it is commonly defined as the shortest distance between the leading edge and the trailing edge. The *chord* is known as the length of the chord line Can be seen as in Figure 2.4, and as 'c' in Figure 2.5.
- **Thickness (maximum thickness):** defined as the distance between the lower and upper surface perpendicular to the chordline of the airfoil. Specifically, the *thickness* of the airfoil is commonly defined as its *maximum thickness*, and it is accompanied by the corresponding location along the chordline denoted as t_{max}.
- **Camber (mean line):** determined by calculating the average of the lower and upper surfaces coordinates along the thickness axis at each point along the

chordline. The *camber* is defined as the maximum computed value of the mean line, and similar to the thickness, its location along the chordline is commonly indicated and defined as cam_{max}.

2.3.2 Wing Planform

In conceptual aircraft design, four main parameters should be estimated in the earlier stages to size up the aircraft; takeoff weight (MTOW), Thrust, reference area, and aerodynamic efficiency [41]. The wing is the main driver of aerodynamic efficiency, as it is usually the only or the main lifting surface of the aircraft. The aerodynamic properties of the wing are defined by its geometry. This geometry is typically defined as joining two different shapes; the airfoil and the planform [39].

The wing has a large number of parameters, as throughout history the design complexity has been considerably increased in order to achieve higher aerodynamic efficiencies for specific purposes. Therefore, the need to establish several parameters was raised looking forward to addressing, identifying, defining, and estimating the effects in the aircraft design stages. The information given in this subsection was summarized in concordance with the objective, scope and theoretical background of the project, which are defined in subsections 1.2, 1.3, and 2.1.2 respectively.

2.3.2.1 Planform parameters

- **Span:** it is defined as the measured distance perpendicular to the flight direction of the aircraft between both tips. Can be seen as 'b' in the figure 2.5.

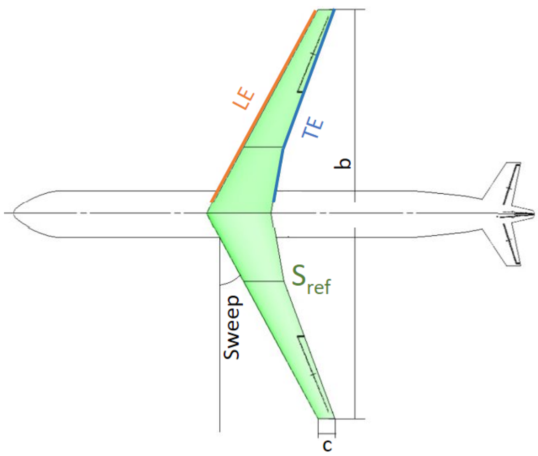

Figure 2.5: Wide-body aircraft scheme with basic wing parameters labeled.

- **Reference area:** this parameter is often referred in the literature as one of the initial drivers for the conceptual design stage [41], as it is the base parameter used to define important aerodynamic properties such as Lift, Drag and moment coefficients [39]. The reference area is defined as the sum of the area of the simplified surfaces that compose the wing, including a virtual section which is made by extending the geometries of the left and the right sections that are joined with the fuselage as shown in Figure 2.5. Alternatively, it can be defined in its integral form as [39, Equation 2.8].

$$S_{ref} = \int_{-b/2}^{b/2} c(y)dy \tag{2.8}$$

- **Aspect ratio:** it is used to infer conceptual design parameters such as induced drag, maneuverability, structural weight, flutter speed, etc [39, 41]. It is defined as the ratio of the squared span to the reference area as in [39, Equation 2.9].

$$AR = \frac{b^2}{S_{ref}} \tag{2.9}$$

- **Taper ratio:** denoted as the ratio between the tip chord and the root chord, plays a significant role in aerodynamic design. It is mathematically expressed as shown in [41, Equation 2.10]. Figure 2.10 in Section 2.3.2.2 depicts a tapered wing planform. The taper ratio is commonly employed to define the lift distribution characteristics during the conceptual design phase of an aircraft. This is partially shown in Figure 2.6. However, it is crucial to analyze and consider its behavior in conjunction with the sweep angle, as emphasized in references such as [39, 41].

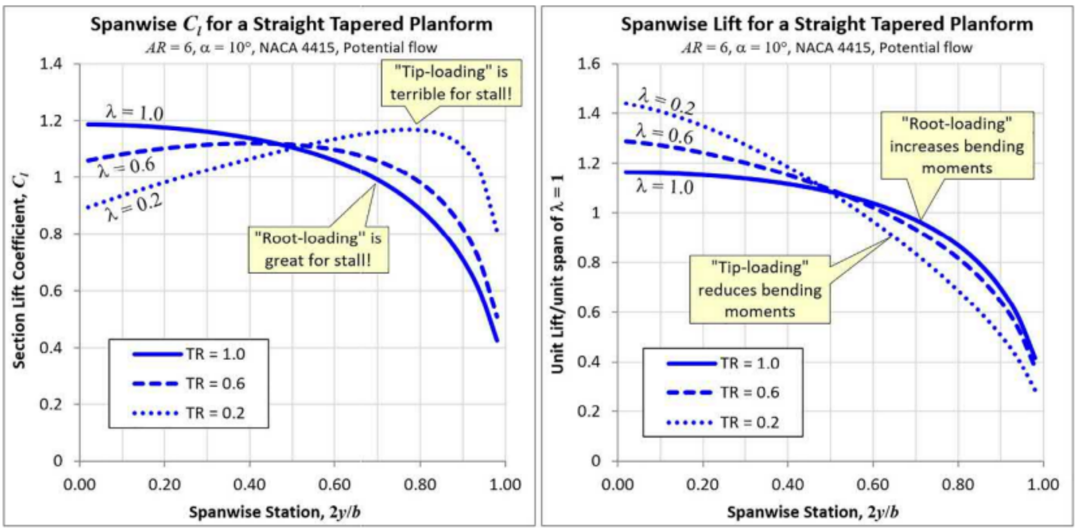

Figure 2.6: Taper ratio effects in lift distribution. Source: adapted from [39]

$$\lambda = \frac{c_{tip}}{c_{root}} \tag{2.10}$$

- **Wing sweep:** it is defined as the angle formed by the line perpendicular to the airflow and the leading edge. However, in the industry, the latter is replaced by the quarter chord line. Both definitions of this property can be seen in figure 2.7. A sweep angle different than 0 affects negatively weight, lift and the control surfaces properties [41]. Nonetheless, it is required for high-speed flights starting in the subsonic regime to mitigate adverse effects from shock generation, and is useful to correct CG displacement of an aircraft [39].

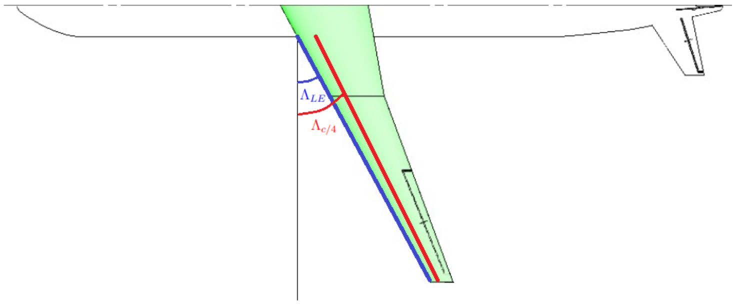

Figure 2.7: Wing sweep in planform.

- **Dihedral angle:** it is defined as the angle formed between the surface of the wing and the horizontal plane. It is usually considered positive if the tip is located higher than the root and is named 'dihedral'. Alternatively, if the tip is located in a lower position than the root the angle is considered negative and named 'anhedral' [41, 39]. It is a crucial property influencing the stability behavior of aircraft, and is intricately tied to the vertical position of the wing, as its value is determined based on this parameter [39]

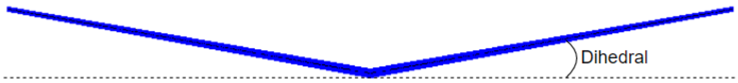

Figure 2.8: Wing with positive dihedral angle, front view.

- **Incidence angle:** used to establish the lowest drag configuration for the aircraft, typically for cruise conditions [39]. It is defined as the difference between root wing chord pitch angle, and the longitudinal axis of the fuselage. [41].
- **Twist:** defined as the difference of the local incidence angles of the wing's surface. Typically defined between the tip and the root sections. Frequently used to prevent the stall of the wing area close to the tip, and its consequences to the maneuverability capabilities of the aircraft [41]. It could be used to slightly modify the lift distribution if required [39]. If the angle of attack of the root is higher than the tip is called 'washout'. Alternatively, if the angle of attack of the tip is higher than the one of the root is called 'washin' [39, 41].

2.3.2.2 Planform types

In this subsection, a typical set of wing planforms will be introduced to the reader, alongside the equations for the most relevant properties.

- **Constant chord:** for this planform type the most relevant geometric properties are defined in the set of equations in [39, Equation 2.11], and the geometrical layout can be seen in figure 2.9.

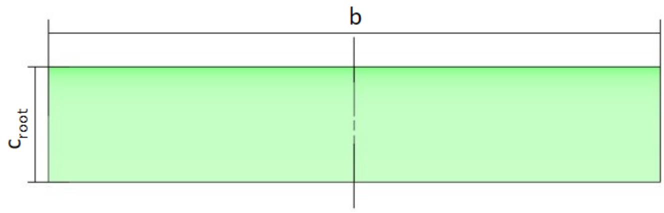

Figure 2.9: Constant chord planform

$$\begin{aligned} S =& b \cdot c_{root} \\ AR =& \frac{b}{c_{root}} \\ c_{MGC} =& c_{root} \end{aligned} \tag{2.11}$$

- **Trapezoidal-straight:** for this planform type the most relevant geometric properties are defined in the set of equations in [39, Equation 2.12], and the geometrical layout can be seen in figure 2.10.

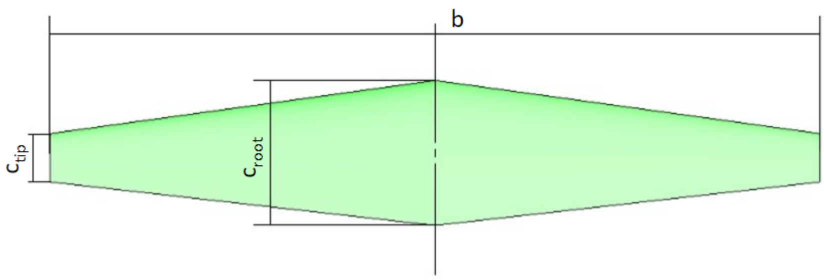

Figure 2.10: Trapezoidal-straight planform

$$\begin{aligned} S =& \frac{b}{2} \cdot (c_{root} + c_{tip}) \\ AR =& \frac{2b}{(c_{root} + c_{tip})} \\ c_{MGC} =& \frac{2}{3} c_{root} \frac{1 + \lambda + \lambda^2}{1 + \lambda} \end{aligned} \tag{2.12}$$

- **Elliptical:** for this planform type the most relevant geometric properties are defined in the set of equations in [39, Equation 2.13], and the geometrical layout can be seen in figure 2.11.

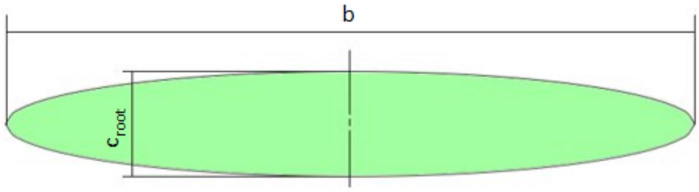

Figure 2.11: Elliptic planform

$$
\begin{aligned}
S =& \frac{\pi}{4} \cdot b \cdot c_{root} \\
AR =& \frac{4b}{\pi \cdot c_{root}} \\
c_{MGC} =& 0.9055 c_{root}
\end{aligned}
\tag{2.13}
$$

By adjusting variables such as aspect ratio, taper ratio, and twist, the spanwise lift distribution can be approximated as an elliptical wing, which can help to reduce induced drag. The Oswald efficiency factor can be used as a metric for optimizing the geometry of the wing to minimize induced drag.

2.3.3 Strut and strut braced wing

The idea behind the strut braced wing (SBW) is to have additional airfoil-shaped trusses for supporting the Wing. This configuration comes with coupled aerodynamic effects and weight effects.

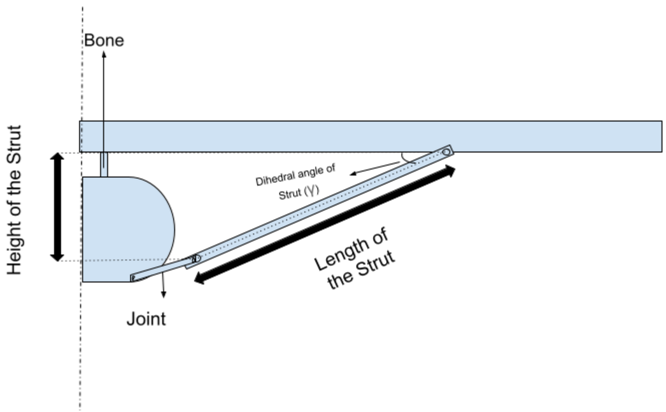

Figure 2.12: Strut braced wing

One of the advantages of the strut-braced wing is the relief of bending moment on the wing. When the bending moment is reduced, the weight of the wing can be decreased since lighter reinforcements can be used. Additionally, the strut-braced wing enables a higher aspect ratio and span which increases aerodynamic efficiency (refer to Section 2.4.5) and lowers induced drag. These benefits lead to lighter aircraft and lower fuel consumption or longer range for electric aircraft [2].

On the other hand, the strut-braced wing has disadvantages. Although the strut reduces the weight of the wing, the strut's own weight is significant. If the decrease in weight of the wing is lower than the strut's own, the aircraft will be heavier. If the dihedral angle of the strut decreases, the bending moment relief in the wing will increase, but as the length of the strut increases, the weight of the strut will also increase. Moreover, the strut causes a drag penalty due to its existence, which can be optimized with lift contributions of the wing and strut as well as their position. If the dihedral angle decreases, the skin friction drag contribution from the strut increases as the length of the strut increases. For these reasons, the position of the strut has significant importance in the design.

Furthermore, the strut creates a negative pressure on the lower surface of the wing as the airflow accelerates between strut and wing which creates a Laval nozzle effect. Previous studies show this effect could create a significant negative effect on Lift [42].

In summary, strut braced wing designs have a coupled effect on aircraft design, which can be both advantageous and disadvantageous. The additional strut structure adds complexity and weight to the aircraft, potentially creating an overall disadvantage. However, on the other hand, the strut-braced wing design has the potential to significantly improve aerodynamic efficiency, allowing for weight reduction through optimized design. Therefore, a thorough investigation and optimization of strut-braced wing designs could lead to a substantial improvement in aircraft performance and design methodology.

2.4 Aerodynamics

This section provides an overview of the fundamental aerodynamic principles related to wing design. Subsection 2.4.1 covers basic airfoil concepts, including the physics based on inviscid and incompressible flow assumptions. Subsection 2.4.2 introduces the basic concepts for aerodynamic forces. Subsections 2.4.3 and 2.4.4 define the aerodynamic Lift and Drag forces for 3D bodies. The contents of this section are limited to the scope of the project as detailed in Subsection 1.3.

2.4.1 Airfoil

The airfoil plays a critical role in aeronautics, as it is the core concept used to define the cross-section of the lifting, and control surfaces [41]. The primary function of an airfoil in a lifting surface is to generate lift with the lowest associated drag [43]. The pressure distribution is created due to the airfoil's shape. This can be explained by the concept of a streamline, which refers to the path that a massless particle follows in a region of interest [44]. The airfoil's shape creates a physical constraint that alters the streamlines of the incoming airflow compared to the freestream direction [34]. As a result, a difference in velocity occurs in the airflow that follows these streamlines on both surfaces of the airfoil, which generates a static pressure difference [31].

The direction of the incoming airflow, or freestream direction, has a significant impact on the airfoil's pressure distribution. When the angle between the freestream direction and the chord line of the airfoil changes, the streamlines are considerably modified, as illustrated in Figures 2.13 and 2.14. This angle is known as the angle of attack and is a key parameter for aerodynamic coefficients [37, 39, 41, 43]. In addition to the angle of attack, the freestream velocity also plays a crucial role in determining the airfoil's pressure distribution, as it drives the magnitude of the pressure on both surfaces of the airfoil according to Bernoulli's principle applied to streamlines [41]. The Bernoulli equation for low-speed flows is shown in [37, Equation 2.14], and the Bernoulli equation for every point on a streamline for low-speed flows is given in [37, Equation 2.15].

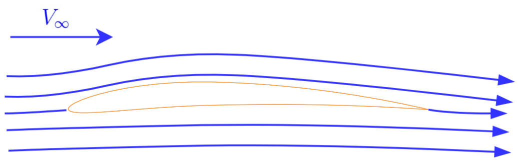

Figure 2.13: Streamlines scheme in a NACA 6409 airfoil with an angle of attack of 0 degrees.

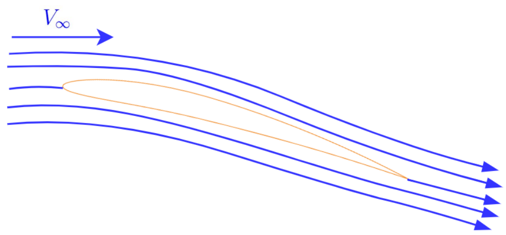

Figure 2.14: Streamlines scheme in a NACA 6409 airfoil with an angle of attack of 15 degrees.

$$p_1 + \frac{1}{2}\rho v_1^2 + \rho g z_1 = p_2 + \frac{1}{2}\rho v_2^2 + \rho g z_2 \tag{2.14}$$

$$p_\infty + \frac{1}{2}\rho v_\infty^2 = constant \tag{2.15}$$

2.4.2 Aerodynamic forces

The flow around the body gives rise to two distinct types of forces: the pressure force and the skin friction force. The pressure force is a consequence of the variations in fluid pressure around the body, while the skin friction force is attributed to the adherence of the flow to the body surface due to the no-slip condition, or shear stress. This can be seen in Figure 2.15.

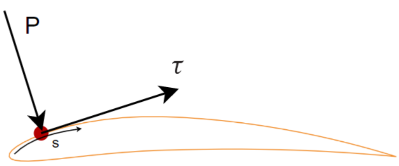

Figure 2.15: Pressure and shear stress in an airfoil. Source: adapted from [30]

These forces can be mathematically expressed as presented in [37, Equation 2.16]. The resulting forces from this interaction can be defined as the integration of both sources over the body surface [30]. These equations take into account the geometry of the body, the properties of the air, and the velocity of the air mass relative to the body.

$$R_{total} = R_{pressure} + R_{friction} \tag{2.16}$$

Typically, the resulting aerodynamic force (R) exerted on a body is concentrated at a specific location known as the center of pressure (CoP). This force can be divided into two distinct sets, each comprising two components. The first set separates the resulting force into a normal force (N), which acts perpendicular to the chord, and an axial force (A), which acts parallel to the chord. The second set represents the resulting force as the lift force (L), which acts perpendicular to the freestream direction, and the drag force (D), which acts parallel to the freestream direction. To establish a connection between the two sets, the angle of attack is defined as the angle formed between the freestream direction and the chord of the airfoil. Consequently, the angle of attack also corresponds to the angle between N and L, as well as A and D. This relation can be seen in [30, set of equations 2.17].

$$\begin{aligned} L &= N\cos\alpha - A\sin\alpha \\ D &= N\sin\alpha + A\cos\alpha \end{aligned} \tag{2.17}$$

However, in the aerospace industry, it is more customary to consider the resulting force to be located at the aerodynamic center (AC). In this representation, a pitching moment (M) arises from the displacement of the resulting force. This concept has been defined in literature [39, 43]. Figure 2.16 depicts a free-body diagram illustrating the acting forces on the airfoil, with the forces positioned at the center of the AC.

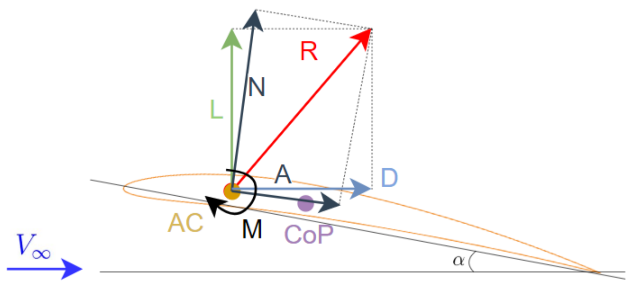

Figure 2.16: Airfoil free body diagram. Source: adapted from [30]

To compute the resultant force acting on an airfoil, it is necessary to integrate the pressure and shear stress distributions along its surface. Figure 2.17 presents a schematic representation of the variables and parameters involved in determining the aerodynamic forces. The pressure distribution (p) and shear stress distribution (τ) are considered functions of the distance 's' measured from the leading edge (LE) to a specific point of interest (A) along the airfoil surface. Furthermore, an angle θ is defined to denote the orientation between the pressure vector and the shear stress vector with respect to lines perpendicular and parallel to the chord, respectively.

This angle is employed to project the magnitudes of both pressure and shear stress in the directions of the normal and axial forces, thereby contributing to the overall resultant force computation [30].

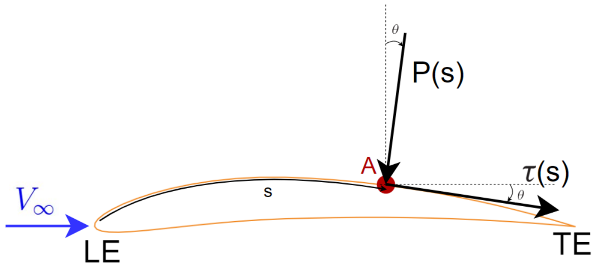

Figure 2.17: Scheme for pressure and shear stress integration over an airfoil. Source: adapted from [30]

The process of calculating the aerodynamic forces on an airfoil is commonly divided into two sets: the upper surface and the lower surface. For each set, the values of the normal force and axial force are determined for every point along the respective surface, starting from the leading edge and extending to the trailing edge. The mathematical expressions, presented in equations [30, set of equations 2.18 and 2.19], provide the per-unit-span formulation of these forces for each surface.

$$\begin{aligned} dn_u &= -p_u ds_u \cos\theta - \tau_u ds_u \sin\theta \\ da_u &= -p_u ds_u \sin\theta + \tau_u ds_u \cos\theta \end{aligned} \tag{2.18}$$

$$\begin{aligned} dn_l &= p_l ds_l \cos\theta - \tau_l ds_l \sin\theta \\ da_l &= p_l ds_l \sin\theta + \tau_l ds_l \cos\theta \end{aligned} \tag{2.19}$$

Let dn_u represent the elemental normal force acting on the upper surface, while p_u and τ_u denote the elemental pressure and shear stress at point A on the upper surface. Additionally, ds_u represents the elemental distance measured from the leading edge along the upper surface to point A. The same notation applies to the corresponding quantities for the lower surface.

The total normal and axial forces per unit span can be determined by integrating the expressions given in sets of equations 2.18 and 2.19 from the leading edge (LE) to the trailing edge (TE). The integration yields the desired values of the normal and axial forces, as demonstrated in [30, set of equations 2.20]. Consequently, the lift and drag values per span unit are calculated using the set of equations 2.17.

$$\begin{aligned} n &= -\int_{\mathrm{LE}}^{\mathrm{TE}} (p_u \cos\theta + \tau_u \sin\theta)\, ds_u + \int_{\mathrm{LE}}^{\mathrm{TE}} (p_l \cos\theta - \tau_l \sin\theta)\, ds_l \\ a &= \int_{\mathrm{LE}}^{\mathrm{TE}} (-p_u \sin\theta + \tau_u \cos\theta)\, ds_u + \int_{\mathrm{LE}}^{\mathrm{TE}} (p_l \sin\theta + \tau_l \cos\theta)\, ds_l \end{aligned} \tag{2.20}$$

Alternatively, the aerodynamic forces can be computed using the models presented in 2.2.

2.4.2.1 Aerodynamic coefficients in 2D surfaces

Dimensionless aerodynamic coefficients are fundamental parameters that hold greater significance than the aerodynamic forces alone [30]. These coefficients provide a standardized representation of aerodynamic forces and can be expressed in relation to various factors, including the target force, airfoil chord, air density, freestream velocity, and angle of attack [39, 43]. The set of equations in [39, Equation 2.21] defines each resulting force and the moment in terms of the previously discussed parameters and properties. Figure 2.18 shows a free-body diagram of the acting forces of interest on the airfoil according to the most common representation.

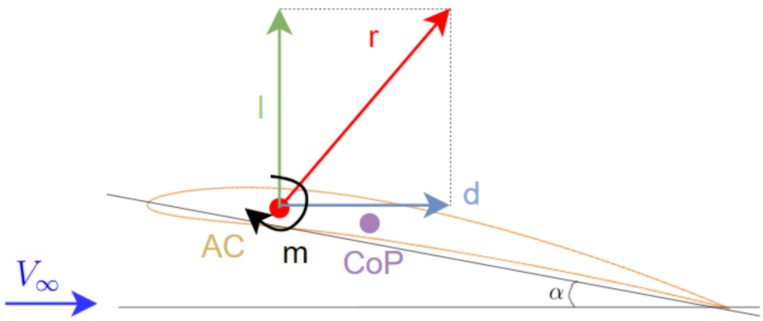

Figure 2.18: Airfoil free body diagram for 2D analysis

$$\begin{aligned} r &= \frac{1}{2}\rho_\infty V_\infty^2 c C_r \quad \text{or} \quad C_r = \frac{2r}{\rho_\infty V_\infty^2 c} \\ l &= \frac{1}{2}\rho_\infty V_\infty^2 c C_l \quad \text{or} \quad C_l = \frac{2l}{\rho_\infty V_\infty^2 c} \\ d &= \frac{1}{2}\rho_\infty V_\infty^2 c C_d \quad \text{or} \quad C_d = \frac{2d}{\rho_\infty V_\infty^2 c} \\ m &= \frac{1}{2}\rho_\infty V_\infty^2 c^2 C_m \quad \text{or} \quad C_m = \frac{2m}{\rho_\infty V_\infty^2 c^2} \end{aligned} \tag{2.21}$$

Where ρ_∞ is freestream density, V_∞ is freestream velocity or airspeed, S is reference area, c is chord, C_r is the dimensionless coefficient that relates the angle of attack to the resulting force, C_l is the dimensionless coefficient that relates the angle of attack to the lift force, C_d is the dimensionless coefficient that relates the angle of attack to the drag force, C_m is the dimensionless coefficient that relates the angle of attack to the pitching moment.

To enhance simplicity and clarity, the set of equations could be reformulated by introducing the concept of dynamic pressure. Dynamic pressure, a fundamental property in aerodynamics, quantifies the impact of air motion on the airfoil and is mathematically expressed as follows:

$$q_\infty = \frac{1}{2}\rho_\infty V_\infty^2$$

If it is within the interest of the reader to go deeper into the theoretical background of airfoils, it is recommended to look out for chapter 4 in [41], chapter 8 in [39] and chapter 5 in [43].

2.4.2.2 Aerodynamic coefficients in 3D bodies

In a manner analogous to the approach discussed in the previous section, the resultant forces acting on a three-dimensional (3D) body are defined, as illustrated in Figure 2.19. Furthermore, the resulting force can be decomposed into three components: the lift force, the section drag force, and the pitching moment. These components can be used to define the dimensionless aerodynamic coefficients, as shown in the set of equations in [39, Equation 2.22]. It is relevant to highlight that for 3D calculations the letter used to define the component is written in upper case, while for 2D calculations the letter used to address the component is written in lower case.

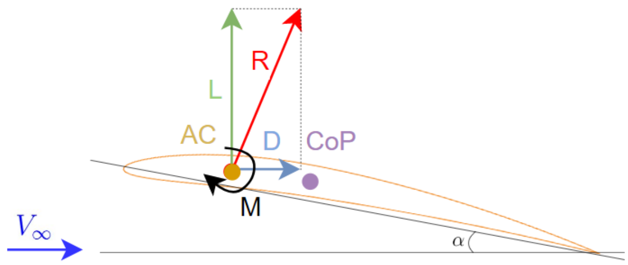

Figure 2.19: Body free body diagram for a 3D analysis

$$\begin{aligned}
R &= q_\infty S_{ref} C_R \quad \text{or} \quad C_R = \frac{R}{q_\infty S_{ref}} \\
L &= q_\infty S_{ref} C_L \quad \text{or} \quad C_L = \frac{L}{q_\infty S_{ref}} \\
D &= q_\infty S_{ref} C_D \quad \text{or} \quad C_D = \frac{D}{q_\infty S_{ref}} \\
M &= q_\infty S_{ref} c_{MGC} C_M \quad \text{or} \quad C_M = \frac{M}{q_\infty S_{ref} c_{MGC}}
\end{aligned} \tag{2.22}$$

Where q_∞ is the dynamic pressure, S_{ref} is the reference area, c_{MGC} is the mean geometric chord, C_L is the dimensionless coefficient for the lift force, C_D is the dimensionless coefficient for the drag force, C_M is the dimensionless coefficient for the pitching moment.

The modelling of the dimensionless coefficients for each property can be as extensive and comprehensive as required. Basic models are commonly defined as functions of geometry, Reynolds number, Mach number, angle of attack, and angle of yaw. On the other hand, advanced models typically include the different components and bodies that contribute to the property of interest [39].

2.4.3 Aerodynamic lift

The lift force is defined as the component of the resulting force perpendicular to the freestream [30], which for a 3D body can be extended to a plane perpendicular to the freestream. As mentioned in section 2.3.1, the lift force is highly dependent on the angle of attack and the geometry of the airfoil, and on the planform shape whose effects are briefly discussed in subsection 2.3.2.

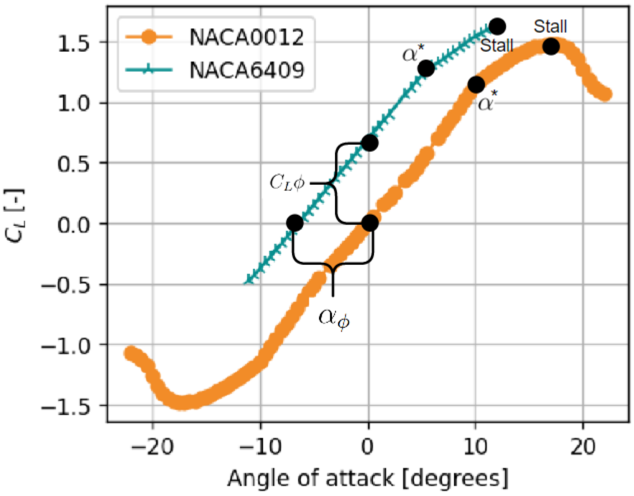

Figure 2.20: Airfoil lift coefficient for uncambered airfoil and cambered airfoil for Reynolds number approximately 2.2 x 10^6.

The relationship between the lift force and angle of attack is typically proportional, although it is subject to aerodynamic limitations that impose a limit on the amount of lift that can be generated [39]. The lift versus angle of attack curve can be divided into three sections. In the first section, which usually ranges from -7 to 9 degrees, the curve has a linear shape that can be extended based on the airfoil geometry [39]. In the second region, a non-linear behaviour appears between lift force and angle of attack, in this region the maximum lift is achieved and the value of angle of attack on such condition is achieved receives the name of stall angle of attack. The start of this region is typically referred to as α^*. This behaviour has a strong dependence on the Reynolds number [39, 41]. Beyond the stall angle of attack, the lift force rapidly decreases. This behaviour is evident in the lift curve for the 'NACA0012' series, as shown in Figure 2.20.

Furthermore, it is crucial to emphasize the considerable influence of airfoil camber on the generation of lift force. A cambered airfoil exhibits a translation effect in the lift force versus angle of attack (AoA) relationship, leading to enhanced lift force generation compared to a symmetrical airfoil at the same AoA. It is often expressed as $C_L\phi$ or α_ϕ according to the axis. This effect is attributed to the curved shape of the cambered airfoil, which results in favourable pressure distributions and improved aerodynamic performance [41].

Furthermore, it is important to highlight the significant role of the airfoil camber in lift force generation. A cambered airfoil generates a translation effect in the lift force vs. angle of attack curve, which can result in higher lift force generation at the same AoA when compared with a symmetrical airfoil [41].

2.4.4 Aerodynamic drag breakdown

In basic terms, drag force is defined as the component of the resulting force parallel to the freestream [30]. The accurate calculation of drag force is of paramount importance in aircraft design, as it affects the performance of the aircraft which leads to the need for changes and thereby, affects other areas and departments within an aircraft company. Additionally, drag modelling is one of the most complex tasks in aircraft design since it is difficult to predict accurately [39]. As a result, it is one of the main drivers or indicators of the feasibility of an aircraft project.

As discussed in section 2.4, the sources for the resulting force are pressure and skin-friction. Consequently, the overall drag force can be further decomposed into various components. In this document, the drag breakdown scheme depicted in Figure 2.21 is adopted. It is important to note that this scheme does not consider the drag effects resulting from shock generation in supersonic flow regimes, nor does it account for additional drag effects that may arise when multiple distinct bodies are interconnected.

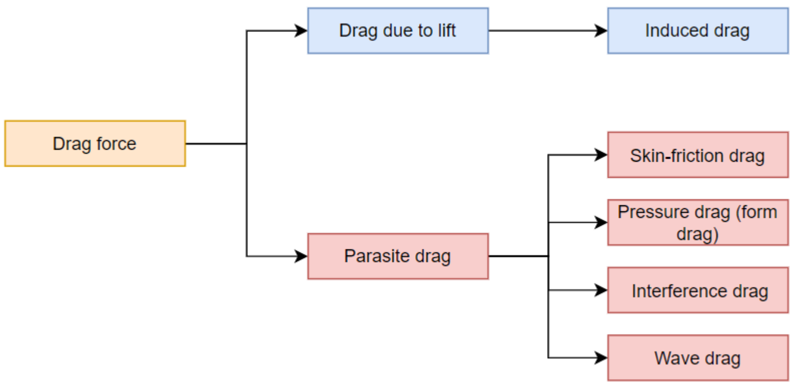

Figure 2.21: Drag classification scheme

Therefore, the total drag can be mathematically defined as in equation 2.23.

$$D_{total} = D_{due\,to\,lift} + D_{parasite} \tag{2.23}$$

Where:

$$D_{due\,to\,lift} = D_{induced} + D_{due\,to\,lift,wave}$$
$$D_{parasite} = D_{pressure} + D_{skin\,friction} + D_{interference} + D_{parasite,wave}$$

However, according to the scope of this work, the total drag forces could be defined as in equation 2.24, as the aircraft will operate at a range $M <= 0.32$.

$$D_{total} = D_{due\,to\,lift} + D_{pressure} + D_{skin\,friction} + D_{interference} \tag{2.24}$$

2.4.4.1 Drag due to lift

As it can be inferred from the name of the drag component, this class of drag is meant to gather all drag components associated with the generation of lift of any type of body. The most known and relevant drag component of this class is the "induced drag", which refers to the drag caused by the consequence of lift and the pressure difference on the tip of the Wing.

The induced drag is proportional to the square of the lift force, according to the elemental derivation for the induced drag coefficient from lifting line theory which is briefly discussed in section 2.2.1.2. The induced drag mathematical expression that relates to the aforementioned concepts is given in [39, Equation 2.25].

$$C_{D_i} = \frac{C_L^2}{\pi \cdot AR \cdot e} \tag{2.25}$$

Where e is Oswald efficiency factor, C_{D_i} is the induced drag coefficient, C_L is the lift coefficient, and AR is the aspect ratio.

Additionally, induced drag is inversely proportional as well to the wing span, with the latter being the main driver to decrease the former, as shown in [45]. Nonetheless, the reference area of the wing is an important constraint for several stages of aircraft design, and varying the value of the wing span will cause a considerable change in the former. However, this effect could be prevented if the chord in the spanwise direction is modified to account for this constraint. Therefore, an additional property is often used to account for the induced drag reduction, aspect ratio [39, 41]. The wing tip shape plays a relevant role in the induced drag as the vortex generation starts in that zone, implementing different types of defined geometries in the wing tip is a common and effective strategy to achieve a relevant decrease in the induced drag [45]. The dihedral angle also has a proportional correlation with the induced drag, as the lift generated by the lifting body will decrease as the dihedral angle increase, but the drag will remain the same [45]. Drag reduction is intertwined with the body parameters and properties, for the wing-body such elements are discussed in section 2.3.2.

2.4.4.2 Parasite drag

This drag class covers all the drag components that are not included in the 'drag due to lift' class. In this section, the concepts of skin-friction, pressure, interference and wave drag will be briefly discussed.

1. **Skin-friction drag:** This drag component arises from the effect of viscosity in the flow. It manifests as a tangential force exerted on the surface of a body when a fluid passes over it, as the molecular interactions within the fluid impede the relative motion between its molecules, resulting in shear stresses [45]. The magnitude of skin-friction drag is closely associated with the surface roughness of the body. Specifically, it is directly proportional to the roughness regardless of the flow regime. However, it is worth noting that surface

roughness can have advantageous effects in certain scenarios, as it can delay flow separation by promoting the transition of the boundary layer from laminar to turbulent, thereby reducing drag [46]. The skin-friction drag shows different behaviours according to the fluid flow regime, as well as the value of the Reynolds number. However, it is inversely proportional to the Reynolds number. The skin friction force and skin friction drag coefficient are given in [39, Equations 2.26 and 2.27].

$$D_{skin\,friction} = \frac{1}{2}\rho_\infty V_\infty^2 C_f S_{ref} \tag{2.26}$$

$$C_{Df} = \frac{2D_{skin\,friction}}{\rho_\infty V_\infty^2 S_{ref}} = C_f \left(\frac{S_{\text{wet}}}{S_{ref}}\right) \tag{2.27}$$

Where C_{D_f} is the skin friction drag coefficient, C_f is the skin friction coefficient, D_f is the skin friction drag force, ρ_∞ is the air density, V_∞ is the far-field airspeed, S_{wet} is the wetted area.

2. **Pressure drag (form drag):** the origin of this drag type is due to the pressure distribution normal to the body surface [45]. The shape of the body surface dictates the magnitude and the rate of change of the pressure gradient alongside the axis parallel to the fluid flow according to Bernoulli's principle. To illustrate the relationship between pressure and geometry, an airfoil can be considered with a flow at an angle of attack (AoA) of 0 degrees. In this scenario, the pressure gradient from the stagnation point to the maximum thickness region would exhibit a negative value. Conversely, beyond the maximum thickness point, the pressure gradient becomes positive, leading to a deceleration of the flow. This positive pressure gradient is commonly referred to as an adverse pressure gradient. A visual representation of this pressure distribution can be observed in Figure 2.22. In such a scenario, flow separation occurs as the momentum of the decelerated fluid in the boundary layer is too low in order to move against the adverse pressure gradient. The separation of the boundary layer gives rise to a shear layer at the detachment point, leading to the formation of a turbulent wake behind the maximum thickness region (or in close proximity to it). In this wake, the pressure is expected to be equivalent to the local pressure within the boundary layer at the point of separation. The difference between the pressure acting in the front and rear zone of the body would be highly related to the pressure drag. In the case of flows characterized by high Reynolds numbers, the transition of the boundary layer from a laminar to a turbulent regime is expected to occur prior to reaching the maximum thickness point in the geometric configuration. However, the exact location of this transition point is influenced by factors such as the pressure distribution along the body geometry and the angle of attack. Hence, the momentum and energy of the boundary layer will be higher due to the turbulent mixing which would delay the separation when compared to the laminar flow regime [46].

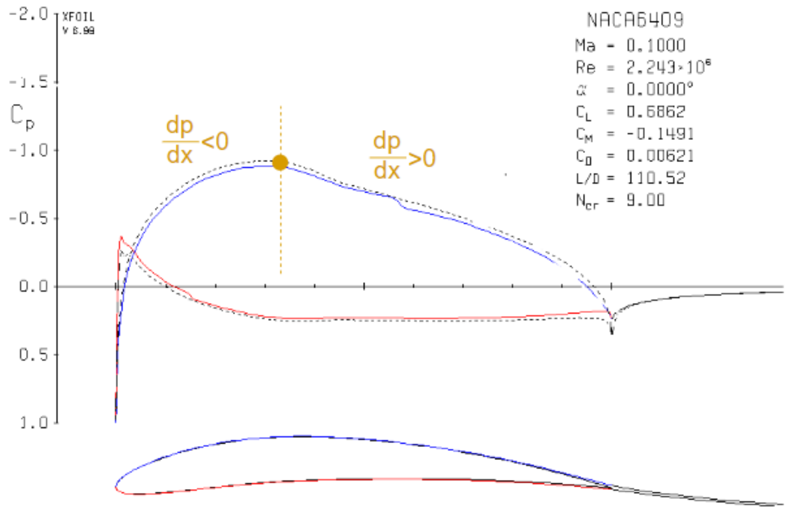

Figure 2.22: Pressure distribution in an airfoil. Source: XFOIL [25]

For lifting bodies as a wing, the angle of attack (detailed in section 2.3.2) would vary according to the mission profile of the aircraft. Therefore, the contribution of the pressure drag to the total drag will be increased when compared to a 0 angle of attack scenario [34], as the thickness of the boundary layer is proportional to the AoA.

3. **Interference drag:** arises when two or more bodies are in close proximity, connected, or even intersecting. The interaction between these bodies leads to a combined drag that exceeds the sum of the individual drag values for each body. This phenomenon can be mathematically represented by [45, Equation 2.28]. In cases where one body intersects another, the boundary layers of both bodies merge. The resulting interference drag depends on the thickness of the boundary layer of the larger body and the thickness-to-chord ratio (t/c) of the smaller body. Notably for this case, experimental data cited by [45] indicates that the interference drag can even become negative when the t/c ratio is below 8%. Interference drag is strongly influenced by the generation of lift, especially when one of the bodies involved acts as a lifting body. This correlation stems from the interaction between the pressure gradient and its effects on the upper and lower surfaces at the junction. Importantly, the interference drag exhibits a direct proportionality to the square of the lift coefficient [45]. When considering a body functioning as a strut, the effects of its orientation can be observed in both the spanwise axis (tilting the strut in the wing direction) and the longitudinal axis (tilting the strut in the direction of flow). Specifically, increasing the angle in the longitudinal axis has the effect of reducing interference drag. Conversely, increasing the angle in the spanwise axis leads to an increase in interference drag [45].
However, there is an exception for this case, two bodies that are near each other and one ahead in the flow direction. The drag versus the distance between them will have three different regions. In the first region, the distance between the bodies is inversely proportional to the drag, thus the combined drag will be

lower than the sum of the individual values. In the second region, the distance between the bodies is now proportional to the drag, hence the drag value will increase. In the third region, the distance between the bodies will be too large and then the total drag would be equal to the sum of the individual drag values. The layout of the regions will be dependent on the Reynolds number and the geometry of the bodies [45].

$$D_{interference} = D_{joint\,bodies} - \sum_{n=1}^{\#bodies} D_n \tag{2.28}$$

4. **Wave drag:** this drag type originates from the generation of shock waves in the aircraft bodies due to local flow velocities greater than the local speed of sound (M_{local}>1). Shocks generate an abrupt rise in pressure and other flow properties, this receives the name of compressibility effects by some authors. Thus, wave drag is a form of pressure drag for a particular flow regime. For transonic and supersonic wing design, a parameter named 'critical mach number' is used to refer to the aircraft airspeed on which the compressibility effects start to appear for a given airfoil [39].

2.4.5 Efficiency in lifting bodies

In the field of aircraft design, the notion of "efficiency" plays a crucial role in quantifying the relationship between lift and drag forces or coefficients, depending on the context. This concept serves as a means to compare and evaluate various aerodynamic geometries. Three key parameters that contribute to this evaluation will be discussed in the following sections: aerodynamic efficiency, drag polar, and Oswald factor.

- **Aerodynamic efficiency:** an indirect comparison between lift and drag. It is defined as the ratio of the former divided by the latter. Typically plotted versus the angle of attack. The aerodynamic coefficient (L/D) is important as it is an efficiency metric adopted to compare different aerodynamic geometries, such as airfoils, wings, lifting body, among others. In figure 2.23 can be observed the aerodynamic efficiency for two different airfoils.
- **Drag polar:** it can be considered as a direct comparison between lift and drag in a graphical form. It is typically plotted as C_l (2D) or C_L (3D) in the vertical axis, and C_d (2D) or C_D (3D) in the horizontal axis. In figure 2.24 can be observed the drag polar for two different airfoils.
- **Oswald efficiency:** is a factor that measures aircraft efficiency in producing lift. It relates to how the geometry behaves in terms of induced drag. Therefore, if the Oswald factor has a higher value, the induced drag is lower. This can be observed in [39, Equation 2.29].

$$e = \frac{C_L^2}{\pi \cdot AR \cdot C_{D_i}} \tag{2.29}$$

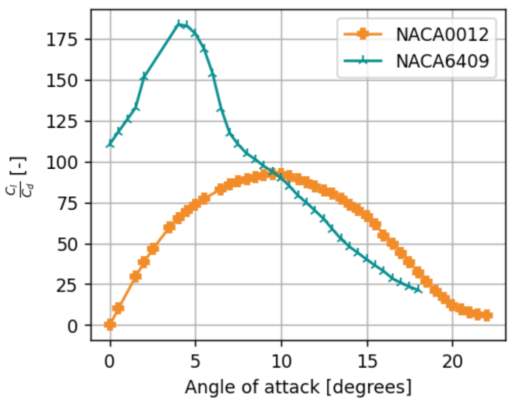

Figure 2.23: Aerodynamic efficiency for two different airfoils

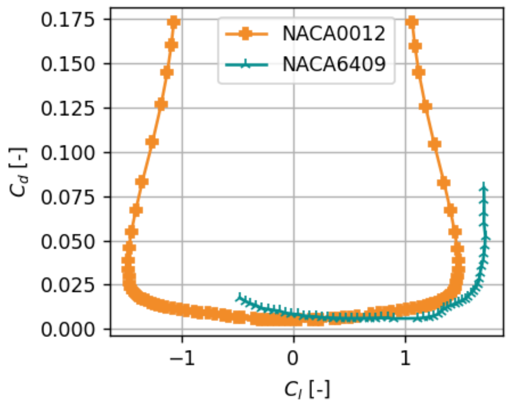

Figure 2.24: Drag polar for two different airfoils

2.4.5.1 Lift distribution and Wing types

The distribution of lift over the wing span plays a crucial role in the level of induced drag. The elliptical lift distribution is known to yield the minimum amount of induced drag, as it maintains a constant downwash across the span of the wing. This results in a lower level of induced drag compared to other wing planforms. The Oswald efficiency factor is a measure of the efficiency of a wing's planforms in terms of induced drag, and the elliptical wing has the highest Oswald efficiency factor without ant wing-tip devices. Higher Oswald efficiency factors could be obtained with wing tip devices. However, due to its high manufacturing cost, the tapered wing is commonly used as an approximation to the spanwise lift distribution of the elliptical wing [30].

2.5 Optimization

In this section, an outline for optimization will be discussed. It would be followed by a brief review of the optimization types in terms of objective functions and constraints. A special focus on the gradient-based, and stochastic optimization techniques is given as well.

Optimization, also known as mathematical programming, encompasses the theoretical background and methodologies used to reach the optimal solution according to a required goal and given constraints [47, 48, 49]. It involves a combination of analytical and numerical methods, including algorithms used to calculate or compute the solutions. Mathematical structure and properties are used to define and model the problem in order to solve it [50].

Optimization is classified based on various perspectives. The most common ones are; regarding the continuity of the domain (continuous or discrete), the order of the objective and constraint functions (linear and non-linear), and the differentiable nature of the objective and constraint functions (differentiable and non-differentiable), among others [48]. However, for the scope of this master's thesis, the classification will be based on how much randomness can be observed. Therefore, two types can be identified; deterministic and stochastic [49].

2.5.1 Modelling structure

The optimization problems are typically defined using the following structure according to [49]:

1. **Decision variables:** input variables for the optimization model. Usually defined as x.
2. **Objective function:** the objective function is a fundamental component of the optimization scheme, defining the relationship between the decision variables and the optimization goal, which is typically to minimize or maximize a certain value. It is denoted as $f(x)$, where x represents the decision variables. In certain cases, when a function cannot be directly formulated, an equation involving the decision variables is employed as a surrogate representation of the objective function.
3. **Constraints:** function or set of functions that must be satisfied in order for a solution to be considered feasible. Constraints are typically expressed as equalities or inequalities in terms of the decision variables of the problem. Constraints can be categorized as soft or hard, with the former allowing for solutions that do not fully satisfy the constraint while penalizing the objective function, and the latter enforcing the constraint strictly to label a solution as feasible.

A common way to express an optimization problem is given:

$$\begin{array}{ll} \textbf{minimize } (min) & f(x) \\ \textbf{with respect to } (w.r.t.) & x = [x_1, x_2, ..., x_n] \\ \textbf{subject to } (s.t.) & g_i(x) \leq 0,\ i = 1, \ldots, m. \\ & h_j(x) = 0, j = 1, \ldots, m. \end{array}$$

Where $f(x)$ is the objective function, x is the decision variables vector, $g_i(x)$ and $h_j(x)$ are functions used to define inequality and equality constraints respectively.

In the field of optimization theory, the notions of locality and globality play a crucial role in determining the best solutions for a given problem. These concepts revolve around how objective functions and decision variables behave within a specific domain or range. By examining the local and global properties of these functions and variables, insights can be gained into the nature of the problem and effective strategies can be devised to find the most favorable solutions. A brief introduction of the most relevant concepts is summarized as follows:

1. **Minimum:** point of the feasible set that has the lowest value of a given function.
2. **Maximum:** point of the feasible set that has the highest value of a given function.

3. **Local minimum/maximum:** point of the feasible set that has the lowest-/highest value for a subset of possible solutions of the given function.
4. **Global minimum/maximum:** point of the feasible set that has the lowest-/highest value for the whole set of possible solutions of the given function.

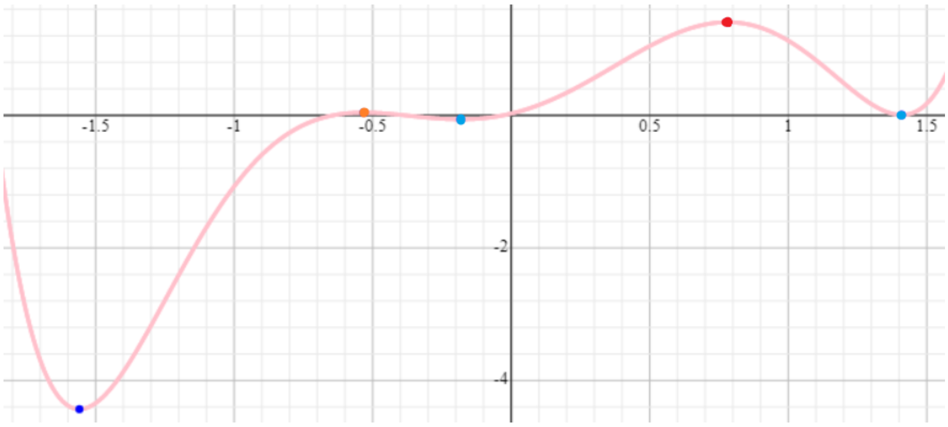

Figure 2.25: Local and global minima and maxima plotted in a function. Where; light blue dots represent local minima, blue dots represent global minimum, orange dots represent local maxima, and red dots represent global maximum

For an optimization problem, the search space is typically wide and it can have multiple solutions that might work to solve a given problem or situation. Typically, the optimization problems can be defined to minimize an objective function $f(x)$. If the requirement is to maximize it, the objective function is reflected over the input axis $(-f(x))$ as most of the algorithms used to solve the methods are designed to follow a minimization scheme [47]. Furthermore, the required solution must fulfill or satisfy certain conditions according to the problem meant to be solved.

2.5.2 Optimization classes

Most of the classic optimization schemes can be included in the deterministic category, as the formulation used to model and solve a given situation is meant to reach a unique solution for particular given sets of initial conditions, and constraints. The following schemes are included in this category; simplex method, descent methods, Newton's method, quasi-Newton methods, and sequential quadratic programming, among others [48, 50]. On the other hand, the stochastic methods rely in a good proportion on random numbers, which means that the obtained results could differ for particular given sets of initial conditions and constraints. The following schemes are included in this category; stochastic tunnelling, parallel tempering, stochastic hill climbing, swarm algorithms, evolutionary algorithms, and cascade object optimization, among others [49].

For this master thesis scope, the selected schemes to solve the optimization problem are; Globalized Sequential Quadratic Programming Algorithm for the deterministic class and Simple Genetic Algorithm for the stochastic class.

2.5.3 Globalized Sequential Quadratic Programming Algorithm

In this algorithm, the objective function and the constraint functions are defined as a system of equations. Newton's method is applied to this system, it consists of the exploration of the dimensions of the decision variable by means of evaluation of the objective function while changing the values of one of the decision variables. This exploration is defined by a set of inputs given as; step size for the exploration and a tolerance for the gradient of the objective function according to the implementation. Such evaluation allows to find a sufficient decrease of the objective function and allows to define a new state or values for the decision vector. The algorithm reaches a solution when the values calculated for the gradient are lower than the input tolerance [50].

If the reader is interested in further reading about this topic, information can be found in Chapter 13 of [48], and Chapter 20 of [50] which includes the detailed algorithm.

2.5.4 Simple Genetic Algorithm

In this algorithm, the main characteristics of evolution are adopted in order to achieve the optimum value for a defined objective function. Following evolution terminology, the decision vector receives the name of 'individual', each variable is encoded under a binary encoding-decoding scheme and receives the name of 'chromosome', a finite number of samples of individuals receives the name of 'population', a finite number of iterations receives the name of 'generations' and the result of an individual evaluated through a merit function is named 'fitness'. The algorithm consists of four steps. First, individuals are randomly generated based on the population size. The second step consists of an evaluation of each individual of the population for the current generation in order to determine the fitness of the entire group and the selection of the fittest individual. The third step is to form the next generation. The new generation includes the fittest individual of the previous generation, and the rest of the individuals are generated by a 'mating process'. This process consists of selecting two individuals and generating two offspring chromosomes with a given probability to inherit one of their parents' chromosomes or the complement of that probability to just copy the parent chromosomes without modification. A mutation factor is typically introduced in order to increase the randomness with a particularly low probability. The last step consists on repeat steps two and three until the maximum number of generations is achieved [49]. This is shown in detail in Figure 2.26 as a flowchart.

If the reader is interested in further reading about this topic, information can be found in Chapter 3 of [49] which includes the detailed algorithm and its main characteristics.

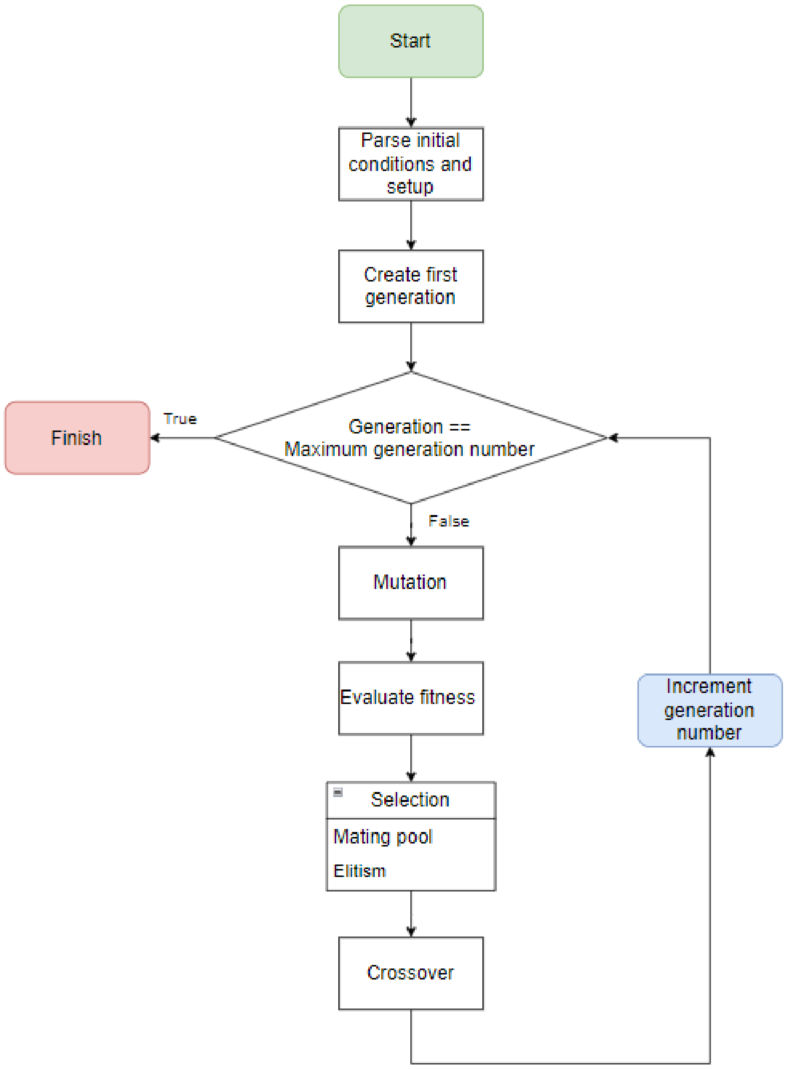

Figure 2.26: Simple Genetic Algorithm flowchart

2.6 Latin Hypercube Sampling (LHS)

The Latin Hypercube sampling is a technique that generates a sample space for a target space based on two premises; guarantee that the entire range of all the input variables (X_i) are included in the sample space, and keep the number of samples in the sample space (O) as low as possible [51]. Therefore, the computational cost for running a simulation will be considerably decreased while covering most sections of the target space (T). It is commonly used in the Monte Carlo Simulation technique in different fields [52].

The scheme consists of the following elements:

- **Number of input variables:** defined as I.
- **Input variables:** space of variables intended to explore, denoted as X. Each input variable has a value assigned, and can be accessed according to the

following form:

$$X_i. \quad i = 1, ..., I$$

- **Input variable range:** intended range for evaluation of each input variable defined as a two points element:

$$X_{range_j}. \ j = 0 \text{ for lower limit, } j = 1 \text{ for upper limit.}$$

- **Strata:** size of the interval, or desired number of samples, denoted as N.
- **Strata interval:** space of the strata interval denoted as Y. Each strata element has the same marginal probability assigned. And can be accessed according to the following form:

$$Y_n. \quad n = 1, ..., N$$

- **Cells:** matrix that holds the values for each input variable and each strata, denoted as S. The matrix has a size of $N \times I$.

$$S_{i,n}. \quad i = 1, ..., I \quad and \quad n = 1, ..., N$$

The cells matrix S is populated by splitting the interval range $X_{i,j}$ of each input variable X_i by the strata N and randomly sampling for each input variable for given strata n. The resulting cells matrix will have a defined number of $N \times K$ cells.

An example of the output structure of a LHS for a 2 input variable and 4 strata scenario. Totalling 8 cells, 4 random values for each of the two input variables. This can be observed in Figure 2.27, with the 4 random variables represented as an **x**.

x			
		x	
	x		
			x

Figure 2.27: LHS with low number of samples number for three input variables

This can be observed in Figure 2.28. The sample space is scattered alongside all the intervals of the three input variables, but the coverage is not that comprehensive.

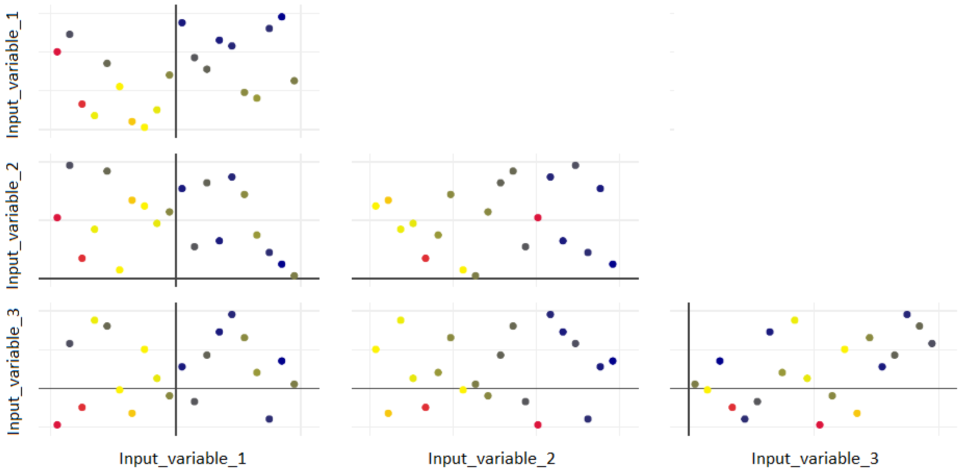

Figure 2.28: LHS with low strata number for three input variables.

The number of strata is of extreme importance as the higher number, the higher the coverage of the target space T by the sample space O. This can be observed when comparing both figures 2.28 and 2.29. An additional example is given to the reader in figure 2.29, while selecting a particular region in the plot of the input variable 2 as a column and the input variable 3 as a row. It can be seen in the other 5 plots shows that the LHS reaches the spectrum (includes the entire range of the input variable 1) that is not delimited by the intervals of the selected region of the input variables 2 and 3.

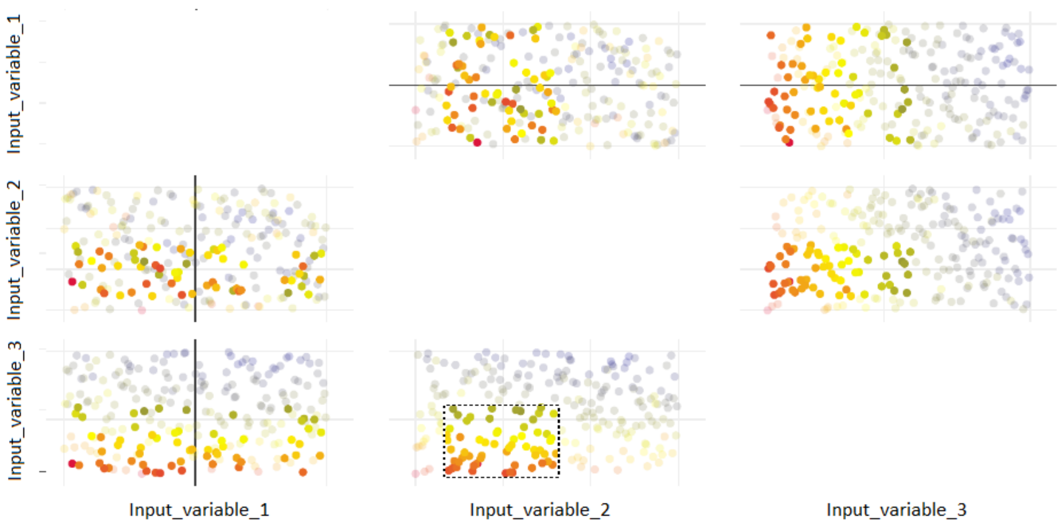

Figure 2.29: LHS with high strata number for three input variables

2.7 Bezier curve

Bezier curve is a parametric curve that can be used for many reasons. In this Thesis, a Bezier curve is used for curve fitting in the sectional twist. The general Bezier curve is defined in [53, Equation 2.30].

$$B(t) = \sum_{i=0}^{n} B_i^n(t) P_i \tag{2.30}$$

Where B(t) is the Bernstein polynomial, and $0 \leq t \leq 1$.

Bernstein polynomial is defined as in [53, Equation 2.31].

$$B_i^n(t) = \begin{pmatrix} n \\ i \end{pmatrix} (1-t)^{n-i} t^i \tag{2.31}$$

For the quadratic case, the Bezier curve can be simplified as 2.32.

$$P(t) = (1-t)^2 \cdot P_0 + 2t(1-t) \cdot P_1 + t^2 \cdot P_2 \tag{2.32}$$

Where P_0, P_1 and P_2 are the control points of the curve shown in Figure 2.30 and $P(t)$ is the new value of the variable where the location is defined with t.

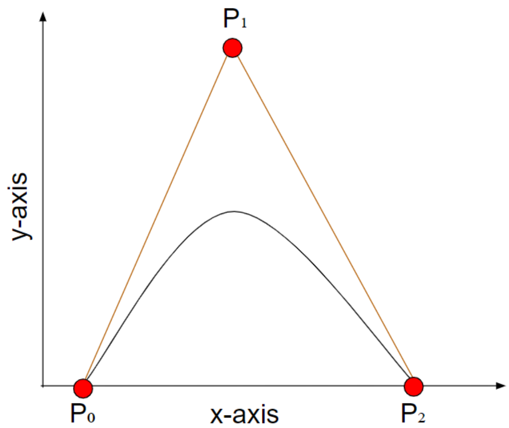

Figure 2.30: Example Bezier curve and control points.

The equation 2.32 is used as Bezier curve formula.

3

Methods

The methods chapter describes the setup of the script and the structure of how the optimization process is performed.

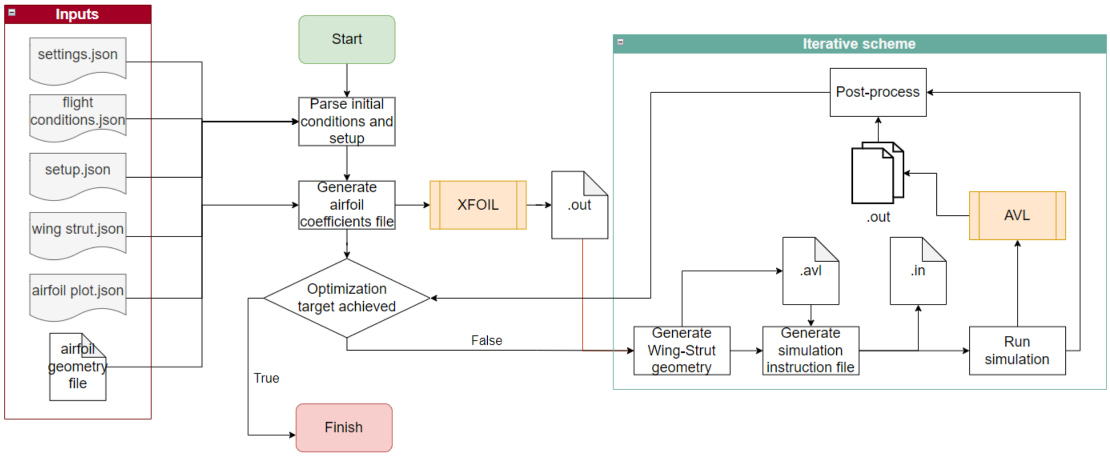

Regarding the shapes; the rectangles represent functions, the paper-like shapes represent files or documents, and the diamond shape represents a decision node. On the other hand for the colors, green and red colors represent the start and end of the simulation respectively, and the remnant represents JSON files as inputs.

3.1 Conceptual Design and Wing Design

In the conceptual design phase of an aircraft, some variables defined for the wing are dependent on the other variables of the aircraft, as explained in Section 2.3.2. Furthermore, in this stage, several iterations should be made in order to obtain a feasible concept to be developed in later design stages. Hence, during the conceptual design stage, it becomes pertinent to employ methodologies that strike a balance between computational efficiency and accuracy. One of the most critical variables for the wing design is the reference area, which would be one of the primary properties that defines the lift coefficient for the flight mission. The required wing area is generally defined by the constraint analyses in conceptual design [39, 41, 43]. Therefore, the wing area is kept constant through this thesis and assumed as 75.76 m^2. Furthermore, the required lift for the wing is determined based on the aircraft's weight. The lift coefficient for the cruise condition is defined as 0.8, considering a reference area of 75.76 m^2.

In strut braced wings, the strut plays a significant role in generating lift for the aircraft. To better understand the influence of reference area variations on the results, a comparative study was conducted, as discussed in Section 4.4. Throughout the study, a fixed reference area of 75.76 m^2 was utilized, while maintaining a lift coefficient of 0.8.

3.2 Airfoil selection

This thesis focuses on investigating the use of low-fidelity CFD (VLM method) and optimization methods. To facilitate this investigation, the NACA0012 airfoil was chosen as the basis for wing generation in this thesis study and will be assigned to the spanwise sections in the planform shown in Figure 3.2. The NACA0012 airfoil was selected for this investigation due to the abundance of available data and the public availability of its geometry. Moreover, NACA0012 is a commonly used and well-studied symmetrical airfoil, which simplifies the investigation of the methods and optimization processes due to its relatively uncomplicated behaviour.

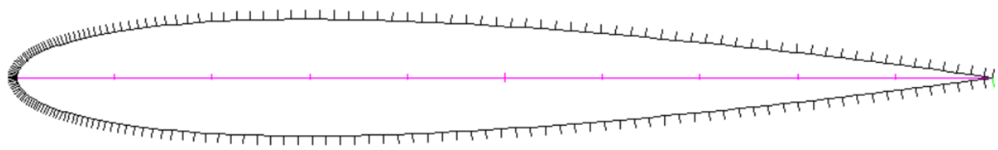

Figure 3.1: NACA0012 airfoil [54]. Source: XFOIL [25]

3.3 Low-fidelity CFD

3.3.1 OpenVSP

3.3.1.1 Geometry

The geometry generation process is facilitated within the OpenVSP framework, employing the "wing" module. The wing geometry is constructed using four sections, each employing the NACA0012 airfoil profile. By specifying the root chord, span, and tip chord for each section, the requisite wing geometry is generated. The planform of the wing is defined as a tapered configuration, featuring a span of 32.3 m, a root chord of 3.193 m, a taper ratio of 0.469, and a reference area of 75.77 m^2.

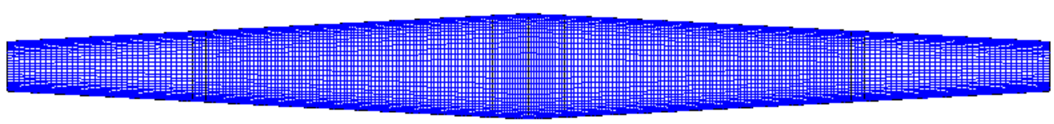

Figure 3.2: Wing planform used in OpenVSP simulations. Source: OpenVSP [35]

3.3.1.2 Mesh

The mesh is generated based on a mesh dependency study. The results of the mesh dependency study are presented in Figure 3.3. The tip section of the mesh is clustered.

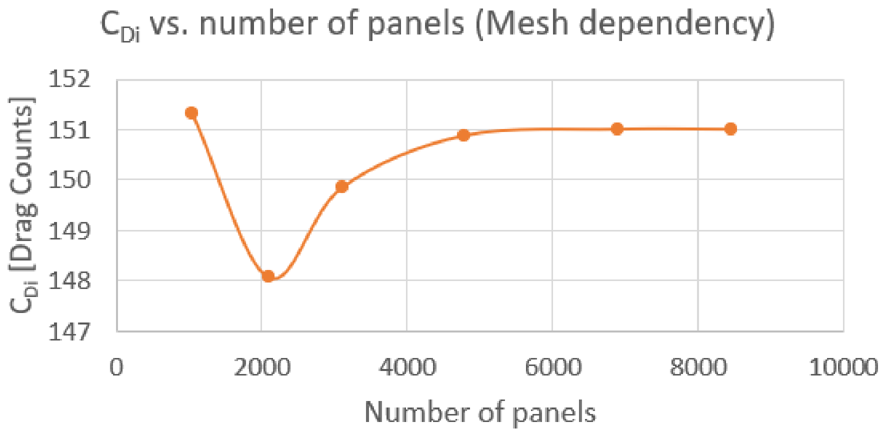

Figure 3.3: Mesh dependency study for OpenVSP

The results of the mesh dependency study for the trapezoidal wing in OpenVSP show that the tip-loaded mesh achieves convergence after 5,000 panels for induced drag. Therefore, a tip-loaded mesh consisting of 5,000 panels is utilized for the remaining simulations in OpenVSP.

3.3.1.3 Setup - VSPAERO

VSPAERO was utilized to obtain data using 3 wake iterations and 64 wake nodes, as indicated in Table 3.1. It was observed that increasing the number of wake iterations and nodes did not significantly alter the results, as they yielded similar outcomes.

Table 3.1: Mesh dependency table for trapezoidal wing

Panel #	**Number of itera-tions**	**Wake Nodes**	C_{D_i} [-]	C_{D_i} **[Drag Counts]**
10472.00	3.00	64.00	0.01560	156
10472.00	8.00	64.00	0.01560	156
10472.00	8.00	128.00	0.01560	156
10472.00	3.00	128.00	0.01560	156

The wake relaxation has no significant effect on results as seen in Table 3.1.

3.3.1.4 Output - VSPAERO

The aerodynamic coefficients, including the pressure coefficient differences between the pressure and suction sides, were extracted from the output file generated by

OpenVSP. This data was subsequently employed for comparative analysis with results obtained from AVL and StarCCM+ [55]. Furthermore, the lift and drag coefficients at different angles of attack were exported for further examination in the comparative study.

3.3.2 XFOIL

XFOIL was employed to acquire the drag polar including viscous considerations data for AVL simulations. The Reynolds number was set to 2,242,744, and the Mach number was chosen as 0.1, aligning with the anticipated cruise speed of the reference aircraft. The analysis was conducted using 200 panels and 100 iterations. The angle of attack range for the analysis spanned from -22 to 22 degrees, with a step size of 0.5 degrees. The selected airfoil for the analysis was NACA0012.

3.3.3 AVL

3.3.3.1 Geometry

In AVL, the geometry is generated using an input file that follows a specific format, as outlined in Figure 3.4. For the mesh dependency study, the induced drag is analyzed and measured in drag counts.

```
!Mach
 0
!IYsym   IZsym   Zsym
0   0   0
!Sref    Cref    Bref
75.765  2.500   27.53
!Xref    Yref    Zref
0.00    0.00    4.040
#------------------------------------------------
SURFACE
WING
!Nchordwise    Cspace    Nspanwise    Sspace
40    3    100    3
SECTION
!Xle    Yle    Zle    Chord    Ainc    Nspanwise    Sspace
-0.749 -16.150 4.040     1.498    0     0     1
AFILE
C:\Thesis\min_aero_strut\naca0012.txt
CDCL
-1.118 0.18641 -0.056 0.00518 1.1194 0.18668
```

Figure 3.4: File format of AVL geometry file

The input geometry of the model includes the defined Mach number, reference surface area, reference chord, and reference span for the entire geometry. Once the surface has been created, the mesh is assigned the "Nchordwise" and "Nspanwise" parameters if the mesh is given globally. If the "Nchordwise" and "Nspanwise" parameters are specified for the section, the mesh is generated according to the given numbers per section. The geometry is generated by defining sections, with each section being defined by its X-position, Y-position, Z-position, chord, and local geometric incidence angle with the profile of the section. Moreover, extension on AVL is used for defining viscous drag by inputting the Lift and Drag coefficients in the global maximum and global minimum points. The X-position, Y-position, Z-position, and chord for each section are determined by formulas/processes specified in section 3.5.1. In the optimizer script, the geometry file is regenerated with the decision variables generated by the optimizer.

Additionally, two different strategies are employed in the simulations and optimization. In the first strategy, the lift contribution from the fairing and joint is included. This means that the lift produced by the entire geometry, including the fairing and joint, is taken into account.

In the second strategy, the lift produced by the fairing and joint is excluded by using the "NOLOAD" option provided by AVL. This allows for the isolation of the lift contribution from the wing only, disregarding the effects of the fairing and joint in the analysis.

Once the wing geometry is created as a surface with sections, the struts, joints, and the fairing part are also generated in the AVL file. This is achieved by creating three surfaces: left strut, right strut, and fairing which contains the joints, as shown in Figure 3.5.

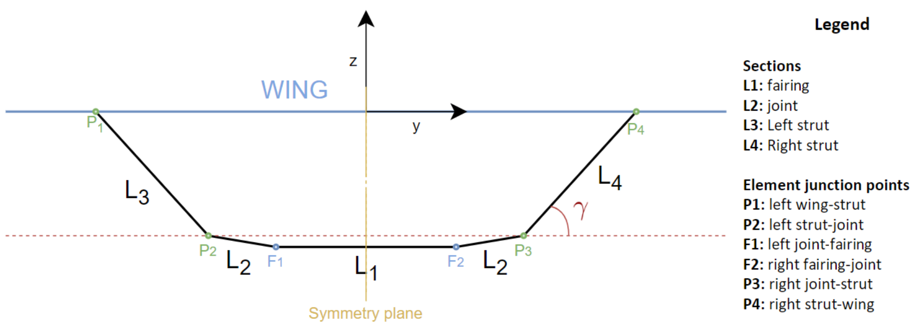

Figure 3.5: Front view of the SBW geometry

All the separate surfaces are also generated with sections as described in Section 3.3.3.1. NACA0012 profile is assigned to all surfaces. Moreover, the strut chord is kept constant along its span and equal to 0.8 m.

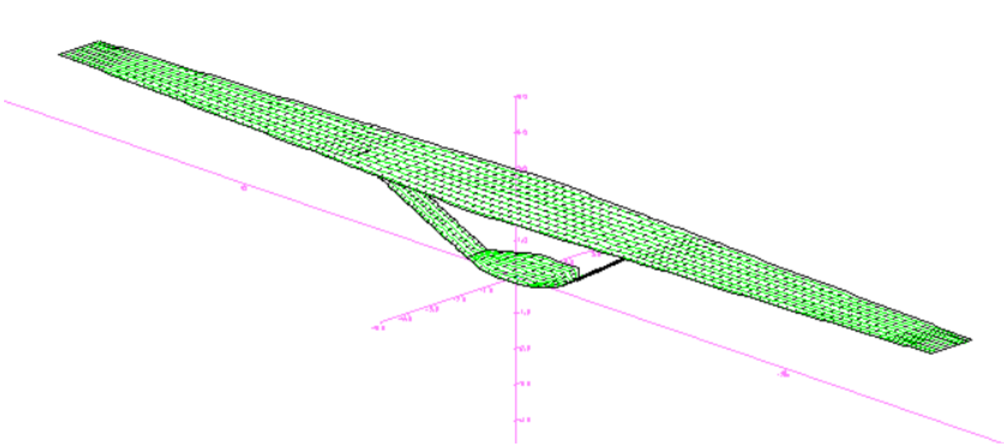

Figure 3.6: Isometric view of the SBW geometry

The joint and fairing part geometries are fixed through the simulations and dimensions are generated due to the reference aircraft [1].

3.3.3.2 Mesh generation

1. **Wing:** two different mesh generation strategies were employed in the study. In the first strategy, a global approach was used where the mesh was applied uniformly across the entire wing, both span-wise and chord-wise. In the second strategy, the mesh was assigned to specific sections of the wing, allowing for more refined meshing at the wingtip (clustered), which is crucial for capturing induced drag effects.

   A mesh dependency study was conducted to determine the appropriate number of mesh elements. The study focused on the convergence of drag counts and Oswald factor, as these variables are calculated within AVL. The results for the trapezoidal wing are presented in Figure 3.7. More detailed information about each mesh configuration can be found in Appendix A.1.

   A mesh dependency study was conducted for three different wing planforms: trapezoidal, elliptical, and rectangular. The trapezoidal wing had a span of 32.3 m, a root chord of 3.193 m, a taper ratio of 0.469, and a reference area of 75.77 m^2. The elliptical wing had a span of 32.3 m, a root chord of 2.457 m, and the same reference area. Similarly, the rectangular wing had a span of 32.3 m, a root chord of 2.346 m, and the same reference area. The aspect ratio (AR) for all three wing planforms was set to 13.77. The simulations were performed with a target lift coefficient of 0.8.

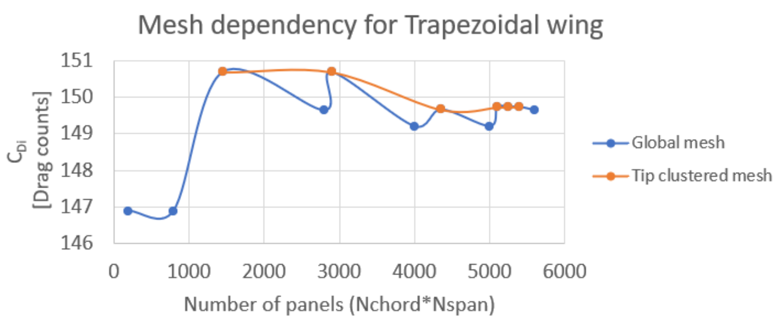

Figure 3.7: Mesh dependency study for AVL for trapezoidal wing based on C_{D_i}

   The mesh dependency study for the trapezoidal wing revealed important findings. It was observed that the clustered mesh configuration reached convergence for both the Oswald factor and induced drag after utilizing 4300 panels. However, when the mesh was not clustered, even with a higher number of panels, convergence was not achieved. Based on these results, the tip-loaded mesh configuration with 4300 panels was selected for subsequent AVL simulations for this wing.

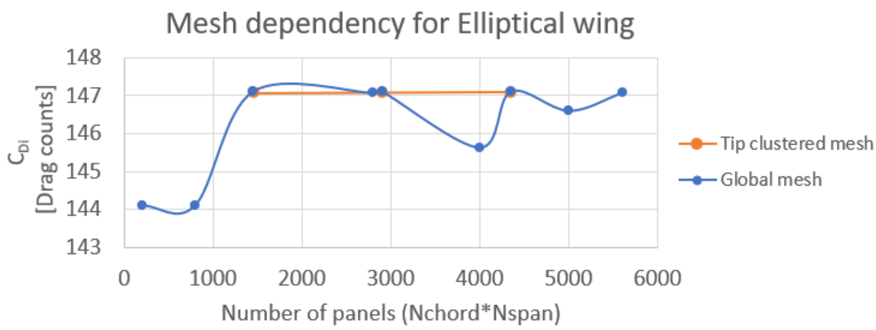

Figure 3.8: Mesh dependency study for AVL for elliptical wing based on C_{D_i}

In the results of mesh dependency for the elliptical wing, the tip-loaded mesh converges after 1400 panels for both Oswald factor and induced drag. On the other hand, if the mesh is not tip-loaded even if the panel number is higher, the convergence does not occur. For this reason, the tip-loaded mesh with 1400 panels is used for the rest of the AVL simulations for this wing.

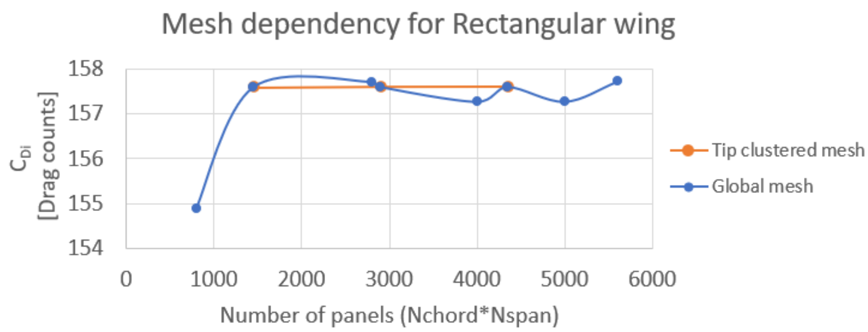

Figure 3.9: Mesh dependency study for AVL for rectangular wing based on C_{D_i}

In the results of mesh dependency for the rectangular wing, the tip-loaded mesh converges after 1200 panels for both Oswald factor and induced drag. On the other hand, if the mesh is not tip-loaded even if the panel number is higher, the convergence doesn't happen. For this reason, the tip-loaded mesh with 1200 panels is used for the rest of the AVL simulations for this wing.

2. **Wing and strut configuration:** strut mesh is also an important factor as the Lift is calculated on the strut also. For the mesh dependency study rectangular wing with a 32.3 m span, 2.346 m root chord and 75.77 m^2 reference area.

   The positioning of the strut in the mesh generation process is crucial, as it has been observed that placing the joint of the strut and wing in the middle of the panel leads to unreliable induced drag values. This discrepancy arises because the induced drag calculated from Trefftz plane analysis and surface integration do not align, as indicated in Table 3.2. This inconsistency aligns with the panel limitations of the Vortex Lattice Method (VLM), as explained in Section 2.2.1.3.

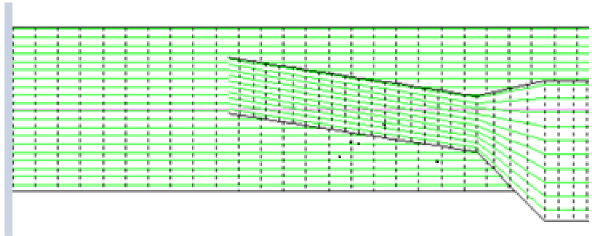

Figure 3.10: Mesh of "Rectangle wing with strut" case

Table 3.2: Mesh generation strategy of wing strut combination

Geometry	C_L	C_{D_i} [Drag counts]	$C_{D_{ff}}$ [Drag counts]	ΔC_{D_i} - $C_{D_{ff}}$[%]
Rectangle wing with strut	0.8	155.748	307.689	49.381
Rectangle wing with strut-remeshed	0.8	156.062	156.568	0.323

Where $C_{D_{ff}}$ is the induced drag calculated with Trefftz plane analysis and C_{D_i} is the induced drag calculated on the surface.

In Table 3.2, a rectangle wing is used to generate this mesh study. In the "Rectangle wing with strut" case, the strut is placed in the middle of the panels as seen in Figure 3.10. On the other hand in the "Rectangle wing with strut-re-meshed" case, the mesh is generated to have a mesh where the corner of the mesh is in the joint of wing and strut as seen in Figure 3.11.

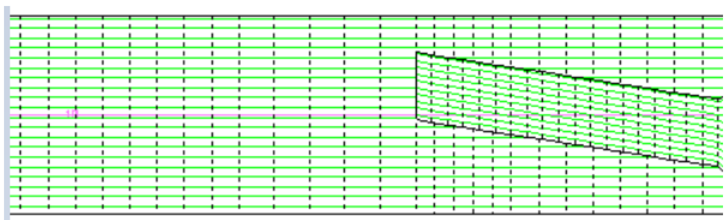

Figure 3.11: Mesh of "Rectangle wing with strut-re-meshed" case

A mesh dependency study was conducted with different numbers of panels using the globally assigned mesh for the strut. Induced drag, which is generated by the strut, was used as the objective of the study. The results of the mesh study are presented in Figure 3.12. The dihedral angle in the mesh dependency study for the strut is selected as 30 degrees. The mesh was generated by taking into account the mesh and position dependency explained above.

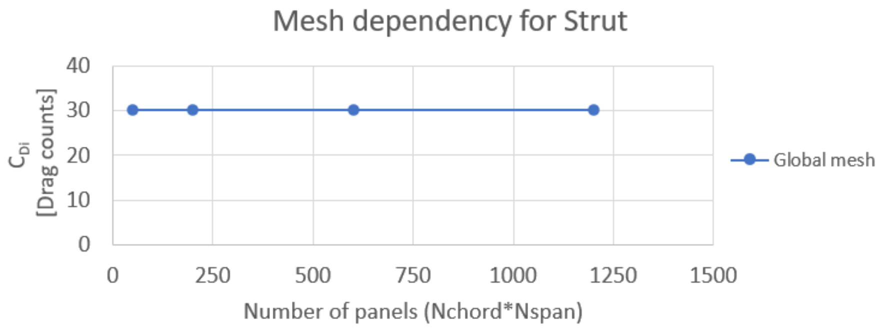

Figure 3.12: Mesh dependency for strut

The results of the mesh dependency study for the strut indicate that the induced drag, calculated using the surface of the strut, converges with a local strut mesh of 100 and does not change with further mesh refinement down to the smallest mesh that AVL accepts. Therefore, a mesh size of 100 is selected for the strut. Further details of the meshes used are provided in Appendix A.1.

3.3.3.3 Output

After the results of the simulation are obtained, it is possible to review the results in different setups, as well as with different degrees of detail. For this work, the total forces (FT), strip forces (FS), and surface forces (FN) files are taken as output. An overview of the FT, FN and FS files is given in Figures 3.13, 3.14, and 3.15.

The information contained in all the files is briefly summarized as follows:

- **FT:** gives the number of evaluated surfaces, the number of strips (spanwise divisions) and vortices (cells or lattices). It gives as well all the aerodynamic coefficients (lift, total drag, induced drag, viscous drag, moment) from the surface and the aerodynamic coefficients (lift, drag, and Oswald factor) from the Trefftz plane, the angle of attack, and the input values for reference area, the span and the mean aerodynamic chord.

```
Alpha =  -1.78635     pb/2V =  -0.00000     p'b/2V =  -0.00000
Beta  =   0.00000     qc/2V =   0.00000
Mach  =     0.000     rb/2V =  -0.00000     r'b/2V =  -0.00000

CXtot =  -0.13066     Cltot =  -0.00030     Cl'tot =  -0.00030
CYtot =   0.00000     Cmtot =   3.77434
CZtot =  -0.79631     Cntot =   0.00006     Cn'tot =   0.00005

CLtot =   0.80000
CDtot =   0.10577
CDvis =   0.09029     CDind = 0.0154835
CLff  =   0.79711     CDff  = 0.0163050    | Trefftz
CYff  =   0.00000         e =    0.9006    | Plane
```

Figure 3.13: FT-Output

- **FN:** outputs the aerodynamic coefficients (lift, total drag, induced drag, viscous drag, moment) based on the geometrical inputs given in the .avl file, geometry-related properties (reference area, mean aerodynamic chord), and the input values for reference area, the span and the mean aerodynamic chord for each surface evaluated by the program.

```
---------------------------------------------------------------
Surface Forces (referred to Sref,Cref,Bref about Xref,Yref,Zref)
Standard axis orientation,  X fwd, Z down

  Sref =   75.75       Cref =    2.4570   Bref =   32.3000
  Xref =     11.0860   Yref =    0.0000   Zref =    4.0520

n      Area     CL      CD      Cm      CY      Cn      Cl     CDi     CDv
1    75.776  0.7113  0.0920  3.3731 -0.0000  0.0001 -0.0003  0.0101  0.0819   WING
2    26.639  0.0887  0.0137  0.4013  0.0000 -0.0000  0.0000  0.0054  0.0083   Strut

Surface Forces (referred to Ssurf, Cave about root LE on hinge axis)

 n     Ssurf      Cave       cl        cd       cdv      cm_LE
 1    75.776     2.346    0.7111    0.0920    0.0819    0.0000  WING
 2    26.639     0.968    0.2522    0.0390    0.0237    0.0000  Strut
```

Figure 3.14: FN-Output

- **FS:** gives the summarized values for the aerodynamic coefficients and geometry-related properties in a similar way as the FN file does for each evaluated surface. Additionally, it gives the specific values for each strip (spanwise group of vortices) in terms of spanwise position. The values given include (but not limited to) the spanwise position of the strip, chord, area, lift coefficient, drag coefficient, viscous drag coefficient, and moment coefficient at quarter chord.

```
---------------------------------------------------------------
Surface and Strip Forces by surface

 Forces referred to Sref, Cref, Bref about Xref, Yref, Zref
Standard axis orientation,  X fwd, Z down

 Surface # 1     WING
   # Chordwise = 20   # Spanwise =129     First strip =  1
   Surface area =   75.775795       Ave. chord =    2.346000
   CLsurf  =   0.71131     Clsurf  =  -0.00031
   CYsurf  =  -0.00000     Cmsurf  =   3.37305
   CDsurf  =   0.09205     Cnsurf  =   0.00006
   CDisurf =   0.01010     CDvsurf =   0.08195

 Forces referred to Ssurf, Cave about hinge axis thru LE
   CLsurf  =   0.71107     CDsurf  =   0.09202
   Deflect =

Strip Forces referred to Strip Area, Chord
  j      Yle     Chord     Area     c cl      ai     cl_norm  cl       cd       cdv     cm_c/4    cm_LE  C.P.x/c
   1 -16.1096   2.3460   0.1894   0.3171   0.1078   0.1356   0.1356   0.0177   0.0078   0.0090  -0.0248    0.184
   2 -16.0289   2.3460   0.1894   0.4711   0.1056   0.2013   0.2013   0.0244   0.0111   0.0122  -0.0379    0.189
   3 -15.9481   2.3460   0.1894   0.5831   0.1034   0.2492   0.2492   0.0295   0.0142   0.0140  -0.0481    0.194
   4 -15.8674   2.3460   0.1894   0.6738   0.1014   0.2879   0.2879   0.0340   0.0173   0.0149  -0.0567    0.198
   5 -15.7866   2.3460   0.1894   0.7509   0.0994   0.3208   0.3208   0.0380   0.0203   0.0155  -0.0644    0.202
   6 -15.7059   2.3460   0.1894   0.8182   0.0975   0.3495   0.3495   0.0417   0.0231   0.0157  -0.0713    0.205
   7 -15.6251   2.3460   0.1894   0.8781   0.0956   0.3751   0.3751   0.0451   0.0258   0.0157  -0.0777    0.208
   8 -15.5444   2.3460   0.1894   0.9322   0.0937   0.3981   0.3981   0.0482   0.0285   0.0155  -0.0836    0.211
   9 -15.4636   2.3460   0.1894   0.9813   0.0919   0.4191   0.4191   0.0511   0.0310   0.0153  -0.0890    0.213
```

Figure 3.15: FS-Output

3.4 High-fidelity CFD

3.4.1 StarCCM+ (Euler equation) - 2D

NACA0012 is imported to STARCCM+ as a point file and the airfoil profile is created with a spline function. The fluid domain is created with a 5m height, 10m long rectangle. The mesh is generated due to the Mesh dependency study results given in Figure 3.16 with polyhedral mesh.

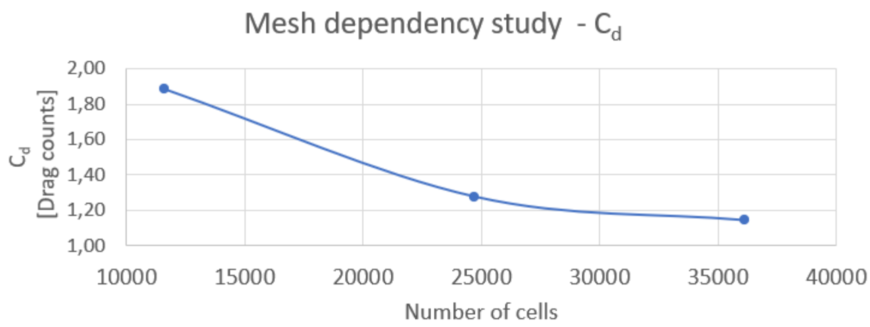

Figure 3.16: 2D mesh dependency study

The mesh convergence study determined that a cell number of 24723 was appropriate for the simulations. The simulations were performed using the Euler governing equations, assuming incompressible flow in a 2D domain. The simulations were steady-state, and the segregated flow setting was used, which solves the governing equations sequentially. The pressure distribution over the airfoil was extracted from the simulations for comparison with the results obtained from XFOIL.

3.4.2 StarCCM+ (Euler equation) - 3D

3.4.2.1 Geometry generation and Boundary conditions

A simple CAD of half of the trapezoidal wing with 32.3 m span (half-span is 16.15 m), 3.193 m root chord, taper ratio of 0.469 and reference area as 75.77 m^2 (37.885 m^2 for half-wing) is generated as the wing. Moreover, a rectangular prism with dimensions 33.193m in Length, 10.2 m in height and 25 m depth and the fluid domain is generated by subtracting half wing from the rectangular prism. The fluid domain, along with half of the wing, is depicted in Figure 3.17. The boundary conditions for the simulation include velocity inlet, pressure outlet, symmetry plane, and wall, as illustrated in Figure 3.17 and Figure 3.18.

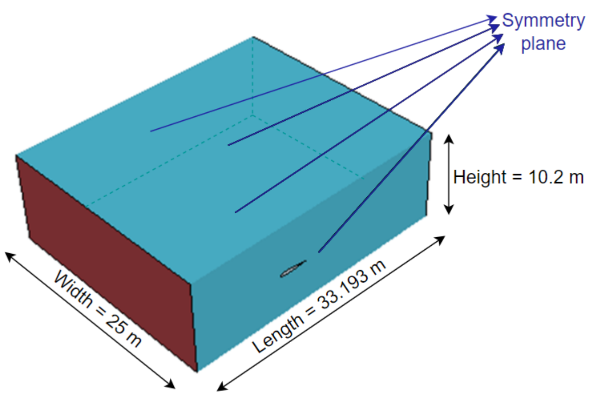

Figure 3.17: Fluid domain with basic setup and properties. Source: StarCCM+ [55]

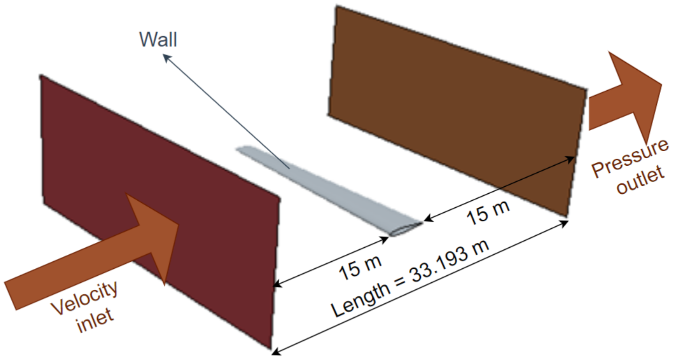

Figure 3.18: Additional relevant setup and properties in the fluid domain. Source: StarCCM+ [55]

3.4.2.2 Mesh generation

A mesh convergence study was conducted for the trapezoidal wing using the Euler equations, which do not account for viscous effects. Therefore, the obtained value for drag represents the induced drag. Moreover, mesh convergence study was conducted with polyhedral mesh with using a block with dimensions 19 m in Length, 4 m in height and 3 m in width to refine mesh around the Wing. The results of the mesh dependency study for the trapezoidal wing can be observed in Figure 3.19.

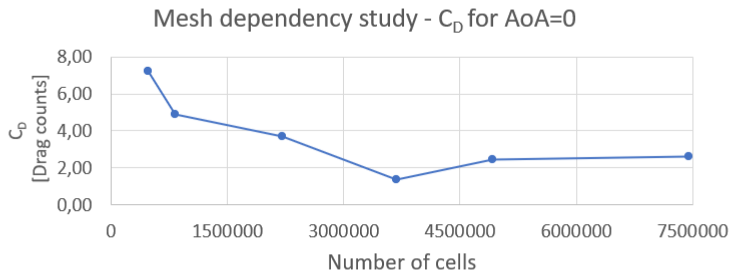

Figure 3.19: Mesh dependency study for StarCCM+ for trapezoidal wing

In the results of the mesh dependency analysis, it was observed that the simulation reaches convergence and provides a stable solution after 5 million cells. Therefore, a mesh with 5 million cells is chosen for the comparative study. The mesh distribution for this configuration is depicted in Figure 3.20.

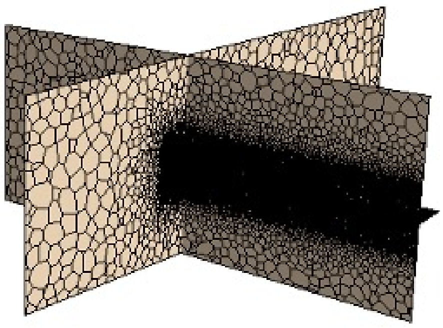

Figure 3.20: Mesh on sections 12.5 m away from wing root and 1.2 m away from the leading edge of the wing

3.4.2.3 Setup and Post process

The simulations were conducted using the Euler governing equations, which assume incompressible flow, in a 3D domain. The simulations were carried out in a steady-state manner, and the segregated flow setting was employed to sequentially solve the governing equations.
In StarCCM+, the Lift and Drag coefficients were calculated using the relative direction of the flow, along with the area, velocity, and density of the fluid. The Lift and Drag coefficients, as well as the pressure distribution, were evaluated for the wing section, specifically the region covering half of the half wing (equivalent to one-fourth of the entire wing span).

3.5 Optimization and analysis framework

Python [28] was selected to couple all the modules required to structure the optimization scheme. The integrated modules could be briefly summarized as; XFOIL [25] software based on panel method coupled with a boundary layer transition model, AVL [26] software based on an extended implementation of VLM for 3D, SciPy library minimize optimization method [27] with the SLSQP algorithm set as the solver, Simple Genetic Algorithm implementation as a stochastic optimization, pyDOE library [56] LHS basic implementation, Python built-in libraries, and as well own-defined functions and features developed for the wing-strut configuration.

The development environment chosen for this project adopts an Object Oriented Programming (OOP) structure, primarily due to its inherent flexibility in facilitating the integration of diverse functions and modules characterized by a certain level of complexity. This model allows to focus on the stored information rather than the logic, which helps to wrap large and complex systems in compact structures that allow as well to integrate new features. Each module will be defined as a class. In a class, the relevant information is stored in variables named attributes, and features or subroutines that would use the stored information to compute additional parameters or properties are defined as methods. Each class will be defined in an independent file, and are classified as core and auxiliary. The auxiliary classes are used to perform intermediate tasks, and the core classes are used to perform advanced tasks. Additionally, helper functions used to ease the parsing, plotting and different basic tasks were defined in the file 'generic functions' and a file called 'run optimizer' is used to run all the methods of the given classes according to the needs of the user. All the input-related parameters, properties, names, and settings are stored in JSON files in order to ease the parsing of the properties as dictionaries in Python, and as well to ease the implementation of new features.

The auxiliary classes are briefly described as follows:

1. **Airfoil:** this class covers all the execution related to XFOIL. It computes and/or plots the pressure distribution and/or drag polar according to the requirements of the user, the simulation can be set as inviscid or viscous. The Input/Output scheme for the airfoil class is shown in Figure 3.21. A color code

is used to define the relationship between the inputs and the outputs. Blue is assigned for data that is used by both outputs, green is for the features related to pressure distribution, and red is for the features related to drag polar.

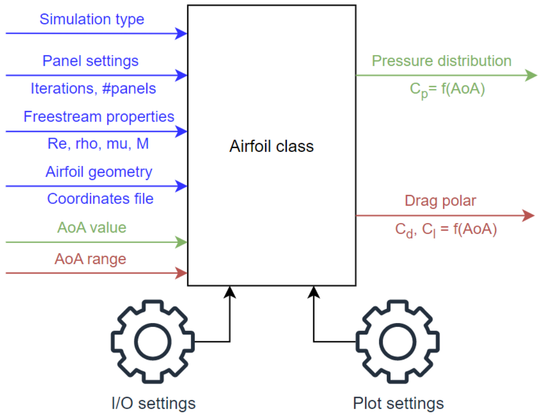

Figure 3.21: I/O scheme for airfoil class

2. **Comparator:** this class objective is to compare different wing-strut designs, usually generated by the optimizer class. The comparison is made in terms of the lift distribution, drag distribution and geometry of the planform and the front view of the design. The Input/Output scheme for the comparator class is shown in Figure 3.22. Again, a color code is used to define the relationship between the inputs and the outputs as it changes for each class. Blue is used for data that is used by all outputs, purple is used for the features related to simulations run in AVL, green is for the features related to lift distribution, red is for the features related to drag distribution, and yellow is for the features related to geometry.

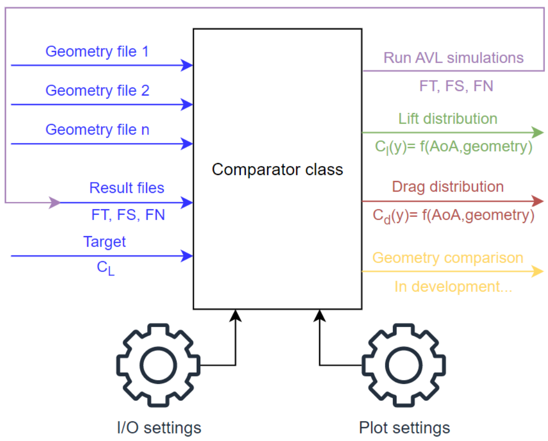

Figure 3.22: I/O scheme for comparator class

3. **DOE:** this class entails all the methods and features related to the design of experiments for the optimizer. Due to the complexity of the search and target spaces, the LHS technique was set up as an initial approach to explore feasible options for the SLSQP and the SGA optimization initial decision variables array with a model that has a relatively coarse mesh. The Input/Output

scheme for the DOE class is shown in Figure 3.23. Again, a color code is used to define the relationship between the inputs and the outputs as it changes for each class. Blue is used for data used to initialize the class, green is used for the test case method generation, purple is used for the features related to simulations run in AVL, and red is for the features related to the simulation result array.

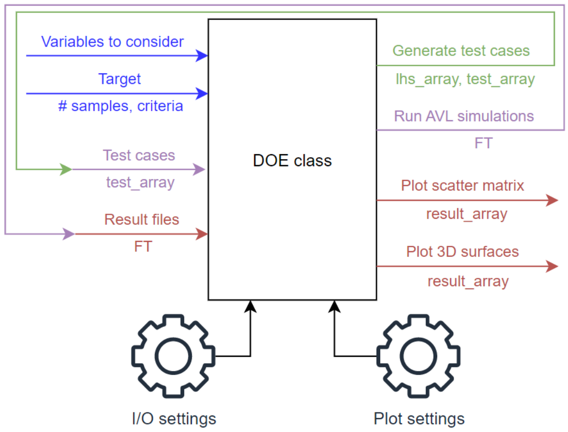

Figure 3.23: I/O scheme for DOE class

4. **SGA:** in this class all the features designed for the Simple Genetic Algorithm are defined. The class has several methods that follow the theoretical background detailed in Section 2.5.4. The Input/Output scheme for the SGA class is shown in Figure 3.24. Again, a color code is used to define the relationship between the inputs and the outputs as it changes for each class. Blue is used for data used to initialize the class, red is for the features related to the optimization result arrays.

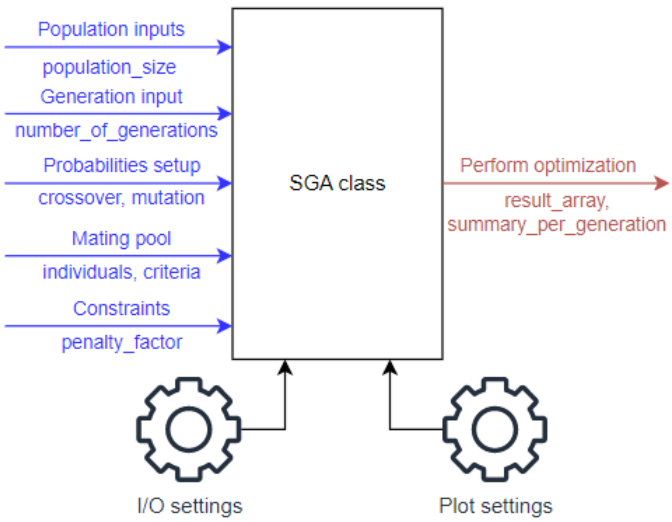

Figure 3.24: I/O scheme for SGA class

A more detailed explanation of the SGA class functionality will be given in the following subsections for the wing-strut and Optimizer classes as they are intertwined.

And as well due to the relevance, size and complexity.

3.5.1 Wing-strut class

The wing-strut class is the core class of the project, as it contains all the methods and attributes/properties for the wing-strut design, mainly related to the geometry of the wing and strut. The geometry definition is done individually for each component. For the wing, a single surface is generated based on the planform types mentioned in section 2.3.2. On the other hand, the strut geometry is generated as three different surfaces; the left strut, the right strut, and the fairing and both strut-fairing joints as a single entity. The previous arrangement was defined in terms of simplicity, and as well as it is quite convenient to enable or disable the contribution of lift generated by the fairing and strut-fairing joints group in the simulation when required. Hence, the wing-strut class will generate four different surfaces. It is relevant to mention that the wing-strut class was developed taking into account that it would play a main role in the optimization scheme, as it will be executed in terms of the decision vector that will be constantly changed in such scheme. Due to the size and extent of these methods, it is deemed necessary to explain in detail the functionality and assumptions of the methods developed in this class.

- **generate_wing_strut_geometry:** return arrays with the x, y, z coordinates, chord and local geometrical incidence values for the wing and the strut. For the wing planform, the geometry is defined in terms of 4 variables; span, chord of the root, taper ratio, and the type of the wing. The type of the wing can be selected as elliptical or tapered, a straight wing can be obtained setting the taper ratio as 1. For the strut, the definition of the geometry is quite complex when compared to the wing. It is defined in terms of 10 variables; strut dihedral angle, strut width, strut height, strut bottom offset, strut top offset, fairing width, fairing length, fairing offset, joint length, and joint height. Finally, for the local geometrical incidences two possibilities are given; define the local geometrical incidence as an array input according to the number of sections of the wing and/or strut, or by the means of a simple three-point Bezier curve defining the values for local geometrical incidence for both wing and strut.
- **generate_avl_file:** return a geometry file (.avl) to the defined path and folder. In this method, the arrays with the x, y, z coordinates, chord and local geometrical incidence values for the wing and the strut are calculated with the generate _wing _strut _geometry method, plus the fixed geometry values for the fairing and the joints, the airfoil coordinate files, and the aerodynamic coefficients for the given conditions are used to generate a file with the required structure by AVL to perform simulations.
- **run_avl_case:** This method executes AVL to carry out a defined simulation. An instruction file (.in) is generated according to the setup in the JSON files, it carries the setup for the simulation and as well defines the output files (.out) to be generated by AVL. Consequently, the instruction and the geometry files are used together to run the desired simulation in AVL.

- **visualize_avl_file:** uses AVL to plot the generated geometry file. Basic script is used mainly to debug and evaluate the results for a set of given inputs. It interrupts the actual code.
- **generate_bezier_list:** generates the local geometrical incidence array using a three-point Bezier curve based on De Casteljau's algorithm for the wing and/or strut. The start (P_0) and end (P_2) points are based on the input array's tip and root values for the wing, the wing-strut joint point, and the strut-fairing joint point for the strut. The middle point (P_1) is generated based on a scalar value given in the decision variable array. The coordinates for a point in the Bezier curve generated in terms of the parametric t value ($0 \leq t \leq 1$) is calculated using Equation 2.32. The value for t is calculated using the positional index based on the number of sections of the wing or strut as shown in Equation 3.1.

$$
\begin{aligned}
t &= \frac{section}{\frac{wing\ number\ sections}{2} + 1} \\
t &= \frac{section}{\frac{strut\ number\ sections}{2} + 1}
\end{aligned}
\tag{3.1}
$$

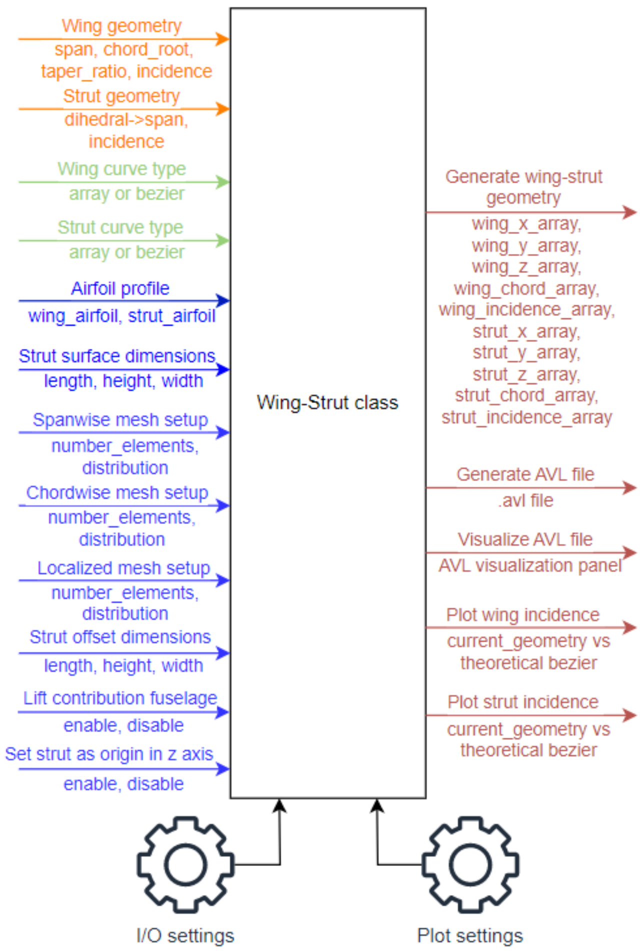

Figure 3.25: I/O scheme for wing-strut class

The Input/Output scheme for the wing-strut class is shown in Figure 3.25. As indicated in the previous classes, a color code is used to define the relationship between the inputs and the outputs as it changes for each class. Blue is used for data used to initialize the class, orange is used for data that is meant to be changed in the optimization scheme, green is used for data structured as settings for the optimization scheme, red is for the features related to the optimization result arrays, output files and plotting schemes.

3.5.2 Optimizer class

The optimizer class is defined to wrap up all the classes presented in the previous sections. The main function of the optimizer class is to run and execute one of the two optimization schemes available; Newton method-based SLSQP and SGA under the selected setup in the JSON files. The secondary functions are; store all the relevant data for the simulation, inherit values to the auxiliary classes, store and plot the simulation results according to the I/O settings, and generate new decision arrays for each iteration of the optimization scheme. The Input/Output scheme for the optimizer class is shown in Figure 3.26. Again, a color code is used to define the relationship between the inputs and the outputs. Blue is used for data used to initialize the class, red is for the features related to the optimization result arrays, orange is for the data that is meant to be changed on each iteration, and green is used to outline the basic features included in the class to perform the optimization.

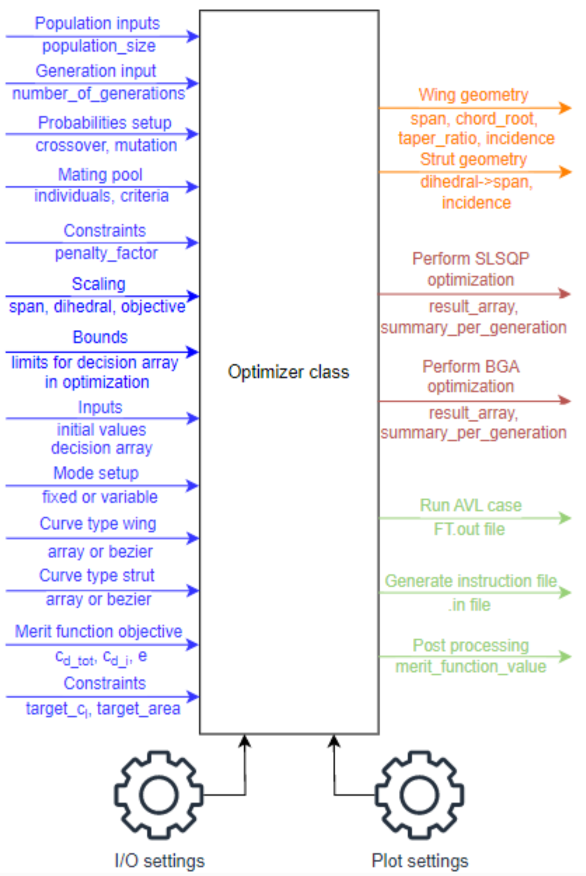

Figure 3.26: I/O scheme for optimizer class

As mentioned in previous sections, the optimizer would use two optimization schemes. Both options are briefly explained as follows:

3.5.2.1 SLSQP

For the SLSQP optimization scheme, there are 3 classes and 6 input files involved. The process can be summarized in 3 steps; Initialization, execution, and evaluation. In the initialization step, the input files are parsed and the information is stored as attributes in the optimizer class. The execution step consists on trigger the 'minimize' function from SciPy library with the 'run_avl' function responsible to compute the objective function. The evaluation step is included in the 'minimize' function, and it is executed several times per iteration as part of the exploration scheme made by the algorithm to define the gradient and Hessian in the search space for the actual state.

A detailed flowchart of the SLSQP optimization scheme can be observed in Figure 3.27. The legend in the flowchart is based on two concepts; shapes that address functionality, and colors that indicate groups and interest points. Regarding the shapes, the circles represent objects, the rectangles represent classes, the rectangles with rounded edges represent functions, the paper-like shapes represent files or documents, and the diamond shape represents a decision node. On the other hand for the colors, green and red colors represent the start and end of the simulation respectively, light blue represents the optimizer class, light yellow represents the airfoil class, light orange represents the wing-strut class, and the remnant represents JSON files as inputs.

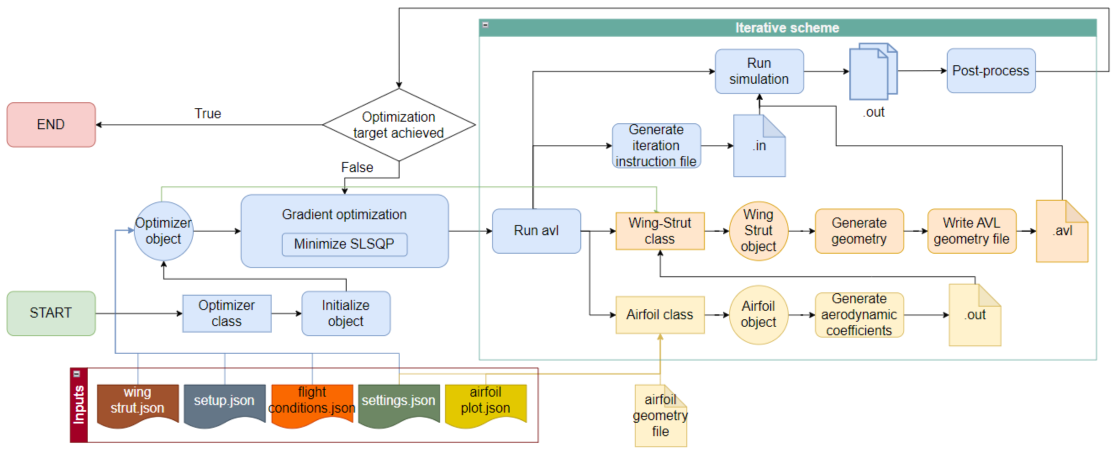

Figure 3.27: Detailed flowchart for SLSQP optimization scheme

3.5.2.2 SGA

For the SGA optimization scheme, there are 4 classes and 6 input files involved. The process can be summarized in 3 steps as well; Initialization, execution, iteration, and evaluation. In the initialization step, the input files are parsed and the information is stored as attributes in the optimizer class. The execution step consists on trigger the 'SGA optimization' function from SGA class with the 'run_avl' function/method which computes the objective function value, this leads to a SGA object creation that inherits all the attributes of the optimizer object. The iteration and evaluation steps are followed as explained in Section 2.5.4.

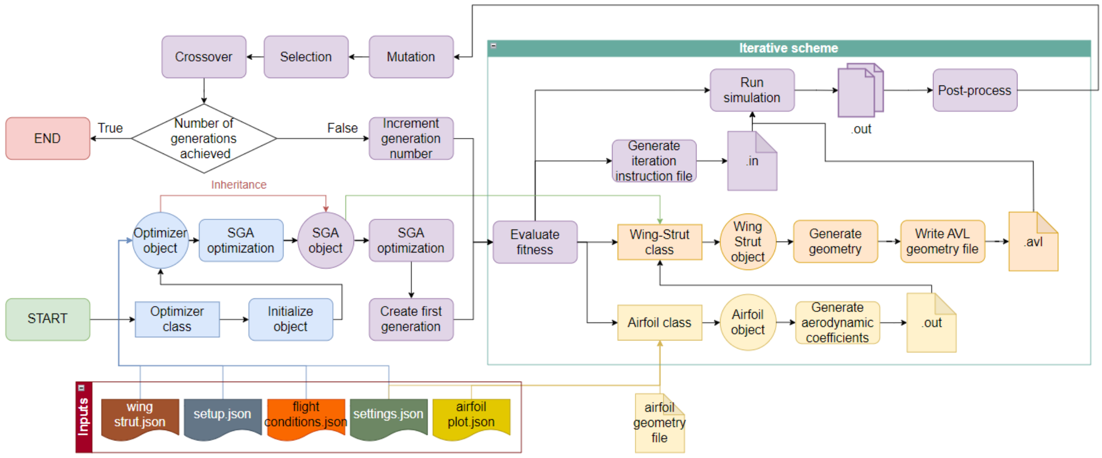

Figure 3.28: Simplified flowchart for SGA optimization scheme

A detailed flowchart of the SGA optimization scheme can be observed in Figure 3.28. The legend in the flowchart is based on two concepts as well; shapes that address functionality, and colors that indicate groups and interest points. Regarding the shapes, the circles represent objects, the rectangles represent classes, the rectangles with rounded edges represent functions, the paper-like shapes represent files or documents, and the diamond shape represents a decision node. On the other hand for the colors, green and red colors represent the start and end of the simulation respectively, light blue represents the optimizer class, light yellow represents the airfoil class, light orange represents the wing-strut class, light purple represents the SGA class, and the remnant represents JSON files as inputs.

3.5.3 Objective function

The objective function is defined as the result of the AVL simulations, which uses the wing-strut class and an instruction file to carry out the required simulation. The instruction file contains a line to produce an output file using the FT layout. Subsequently, Total drag, Induced drag, and Oswald factor are parsed from AVL output file and adopted as the objective/merit function for the SLSQP and SGA algorithms. Total drag, Induced drag, and Oswald factor are parsed from the output file and adopted as objective or merit function for the SLSQP and SGA optimizations schemes.

3.5.4 Bounds

The bounds are defined in the setup JSON file as a set of lists for each variable defined in the iterative scheme. The bounds are the limiting values for a run of the optimization scheme and are defined as a couple of points; the first one is defined as the lower range, and the second one as the higher range. This is intertwined with the 'mode' functionality. The 'mode' just defines if a particular property will be regarded as a design variable or a parameter for a run of the optimization scheme. If the "fixed" configuration in the 'mode' functionality is selected for a property, it will preserve the same value given as an input through the entire simulation scheme.

Table 3.3: Values used to limit the search space for both optimization algorithms

Variable / Parameter	Lower limit	Upper limit
Wing tip and root local geometric incidence [Degrees]	-5	5
Strut local geometric incidence [Degrees]	-5	5
Span b [m]	26	35
Chord root c_{root} [m]	1.8	3.5
Taper Ratio λ [-]	0.1	1.0
Strut dihedral angle [Degrees]	10.4	50

Table 3.4: Additional values used to limit the search space for both optimization algorithms for 'bezier' mode

Variable / Parameter	Lower limit	Upper limit
Wing control point for Bezier curve in spanwise axis [-]	0	1
Wing control point for Bezier curve in incidence axis [-]	0	1
Strut control point for Bezier curve in spanwise axis [-]	0	1
Strut control point for Bezier curve in incidence axis [-]	0	1

Table 3.3 presents the bounds for the initial 'array' mode, which will be applied to all simulations unless explicitly stated otherwise. Furthermore, Table 3.4 provides the bounds for the 'bezier' mode.

3.5.5 Constraints

This section defines two groups of constraints. The first group of constraints fixes the reference area as an equality constraint, while the second group of constraints defines the local geometric incidence variation through the strut when the 'array' mode is selected.

3.5.5.1 Area constraint

When generating the geometry, only the Root chord, Span, and Taper ratio are used, as explained in Section 2.3. The area of the trapezoidal wing can be calculated in terms of these three parameters, using the definitions of the aspect ratio given in equation 2.9 and equation 2.12. The resulting equality is given in equation 3.2.

$$2S_{\text{ref}} - bc_{\text{root}}(1+\lambda) = 0 \tag{3.2}$$

Where c_{root} is the root chord b is span, λ is the taper ratio and S_{ref} is the reference area.

1. **SLSQP:** the lambda function, as described in Equation 3.2, utilizes the values of span (b), taper ratio (λ), and root chord (c_{root}) from the most recent input array to calculate the reference area. In this case, the reference area is maintained at a constant value of 75.77 m^2.

   To incorporate the inequality constraints, two strategies are implemented:

   - **First Strategy:** The equation is formulated as an inequality constraint using the NonlinearConstraint class [57]. The inequality limits are set to -0.5 and 0.5, allowing for a deviation of ±0.5 from the target reference area.
   - **Second Strategy:** The equation is defined as a function, as shown in Equations 3.3 and 3.4, to enforce the inequality constraint. This strategy ensures that the calculated reference area remains within the desired range.

   Both strategies aim to maintain the reference area within the specified limits, thereby satisfying the inequality constraint.

$$\left(2S_{\text{ref}} - bc_{\text{root}}\,(1+\lambda)\right) + 0.5 = 0 \tag{3.3}$$

$$0.5 - \left(2S_{\text{ref}} - bc_{\text{root}}\,(1+\lambda)\right) = 0 \tag{3.4}$$

   Therefore, the inequality is defined in the SLSQP as equation 3.5 for both strategies.

$$0.5 > 2S_{\text{ref}} - bc_{\text{root}}\,(1+\lambda) > -0.5 \tag{3.5}$$

   Where S_{ref} is reference area, λ is taper ratio, b is span and C_{root} is root chord.

   Both constraint strategies yielded the same result, indicating that they effectively enforce the desired constraints on the optimization process. In particular, the inequality constraint approach using the NonlinearConstraint class [57] is primarily employed to enforce the area constraint.

   During the optimization process, the chord root was intentionally held constant to avoid over-constraining the design, considering that the taper ratio is dependent on the chord root. Furthermore, the aspect ratio and taper ratio are two crucial parameters that profoundly influence the drag characteristics of the wing design.

2. **SGA:** equation 3.2 is assigned to SGA as a penalty in the merit function. It is redefined as Equation 3.6 used to define penalty equations in terms of the objective property. Such Equations are defined as 3.7, 3.8, and 3.9.

$$IG = 2S_{\mathrm{ref}} - bc_{\mathrm{root}}\,(1+\lambda) \tag{3.6}$$

- Total drag.
$$P = 305 IG^{\frac{1}{3}} \tag{3.7}$$
- Induced drag.
$$P = 305 IG^{\frac{1}{3}} \tag{3.8}$$
- Oswald factor.
$$P = \frac{1}{305 IG^{\frac{1}{3}}} \tag{3.9}$$

3.5.5.2 Twist constraint between sections

The twist between two sections can be assigned using the local geometrical incidence in each section, which is defined in the AVL file when generating the geometry. This enables the investigation of the twist distribution across the strut and wing. Bezier curve is used as a constraint equation type when assigning the twist constraint.

The Bezier curve formula, as described in Equation 2.32, is utilized for local geometrical incidence distribution along the span of strut and wing. The curve is constructed by assigning values to the local geometrical incidence per section.

In the implementation, the position of the control point P_1, as illustrated in Figure 2.30, is determined by the optimizer without any restrictions, except for the defined bounds. The control points P_0 and P_2 represent the local geometric incidences of the final and initial sections of the strut or wing, respectively. It should be noted that in Figure 2.30, the x-axis represents the span-wise position, while the y-axis represents the local geometric incidence of the section.

Furthermore, if Equation 2.32 is written separately for the x-axis and y-axis, the set of equations described in Equation 3.10 is obtained.

$$\begin{aligned} x &= (1-t)^2 \cdot P_{0_x} + 2t(1-t) \cdot P_{1_x} + t^2 \cdot P_{2_x} \\ y &= (1-t)^2 \cdot P_{0_y} + 2t(1-t) \cdot P_{1_y} + t^2 \cdot P_{2_y} \end{aligned} \tag{3.10}$$

The implementation of the Bezier curve is given below for one optimization step:

1. P_0 and P_2 control points are determined and normalized from the optimization array.
2. The suggested P_1 control point is determined and normalized from the optimization array.
3. The x and y positions are calculated using equations in 3.10 with defined t values and saved into an array.
4. De-normalization of the x and y arrays.
5. Linear interpolation of the array due to the spanwise position of each section.
6. The calculated local geometric incidences are assigned to the corresponding section on AVL.

The bounds for the control point P_1 are set to 0 as the lowest value and 1 as the highest value for both the x and y axes, considering that these axes are normalized. Additionally, the bounds for the control points P_0 and P_2 are defined as -4 and 10, respectively, which align with the bounds set for the other local geometric incidence values.

3.6 Weight estimation methodology

In the weight estimation methodology, there are two ways to estimate the weight of the wing-strut configuration. The first one is using a semi-empirical formula and the second way is using the Bending moment and simplifying strut‘s structure as mentioned in the previous study [58].

3.6.1 Semi-empirical formula

The semi-empiricall formula for weight estimation for wing and strut combination as given [39, Equation 3.11].

$$W_W = 0.002933 \cdot n_z^{0.611} S_W^{1.018} AR_W^{2.473} \quad (\text{ strut-braced }) \tag{3.11}$$

Where n_z is the ultimate load factor, S_W is the wing surface area, and AR_W is the aspect ratio as given in [39].

It is important to note that the semi-empirical formula was developed based on limited databases. Furthermore, the aspect ratio, span, and taper ratio of the wings used to derive these formulas may differ from those of the wings under consideration, which can affect the reliability of the results.

3.6.2 Bending moment and simplified strut methodology

The weight estimation methodology mentioned in this section is based on a previous study [58], and utilizes a semi-empirical weight estimation formula for cantilever wings as presented [39, Equation 3.12]. The assumptions and calculation process for weight estimation are explained in the subsequent section.

$$\begin{aligned} W_W =& 0.036 \cdot S_W^{0.758} W_{FW}^{0.0035} \left(\frac{AR_W}{\cos^2 \Lambda_{c/4}} \right)^{0.6} \\ & \cdot q^{0.006} \lambda_W^{0.04} \left(\frac{100 \cdot t/c}{\cos \Lambda_{c/4}} \right)^{-0.3} (n_z W_0)^{0.49} \end{aligned} \tag{3.12}$$

Where W_W is the weight of the wing, S_W is the surface area, AR_W is the aspect ratio of the wing, W_{FW} is the weight of the fuel, $\Lambda_{c/4}$ is the sweep angle at 25% of MAC, q is dynamic pressure λ_W taper ratio of the wing, t/c is the thickness to chord ratio, n_z is ultimate loading factor, W_0 is the design gross weight. Note that all the units are defined in the imperial measurement system.

The weight distribution is assumed to be triangular across the span, as depicted in Figure 3.29. Moreover, the lift distribution is considered to be continuous up to the symmetry point. The configuration assumes the presence of two motors, similar to the ES-30 aircraft [1].

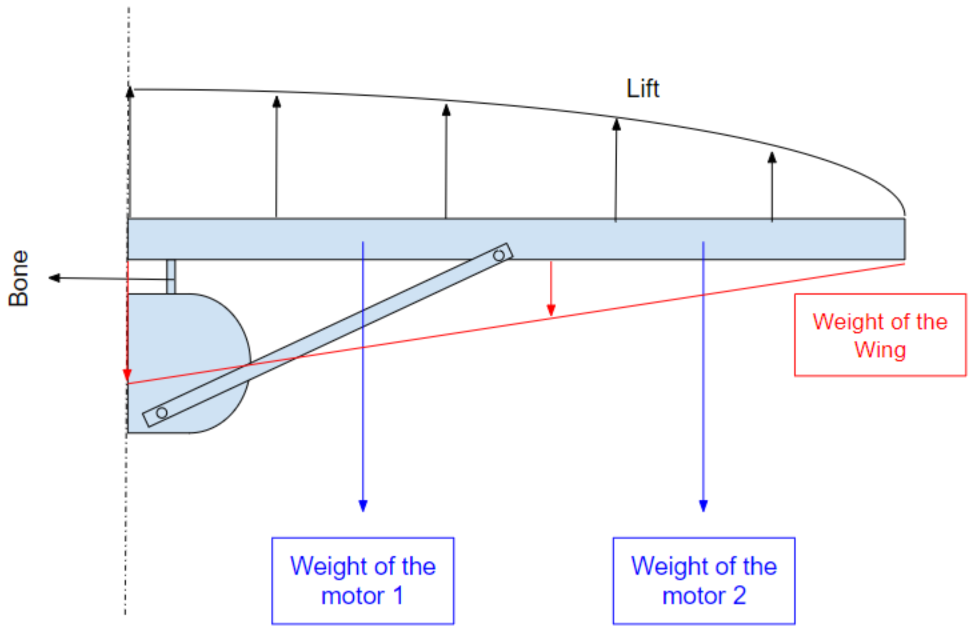

Figure 3.29: Forces on the wing and distributions

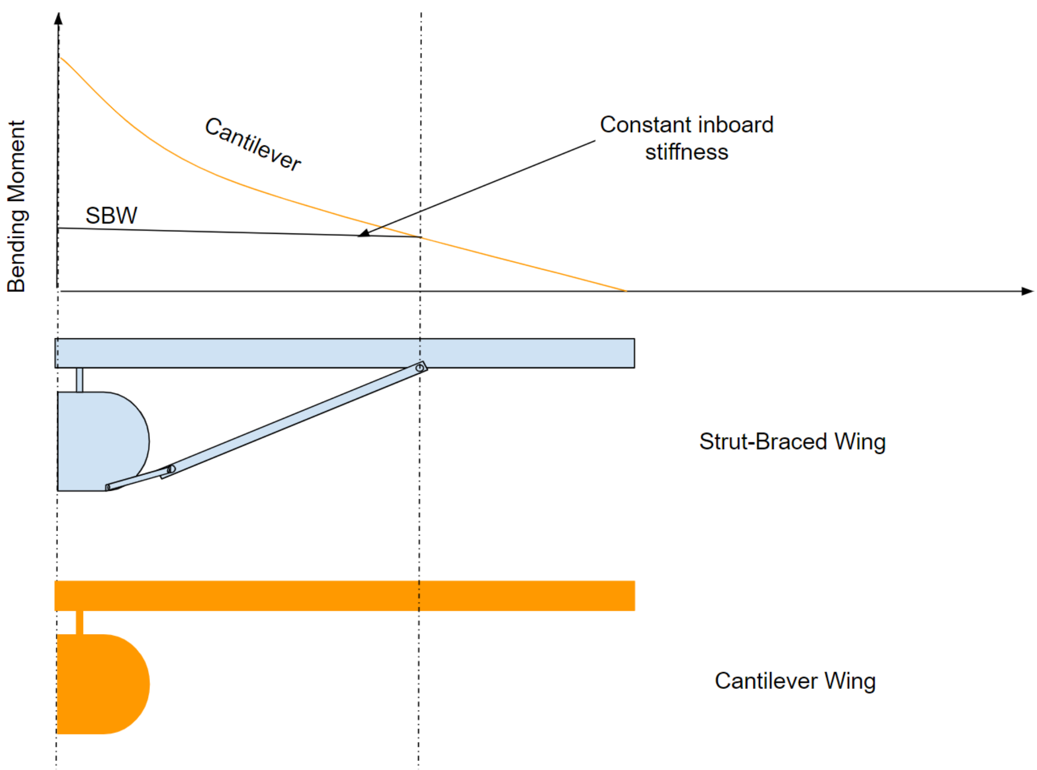

Figure 3.30: Constant inboard loading assumption

In this weight estimation methodology, the internal loads of the wing, including vertical shear and bending moment, are initially computed by taking into account the lift, weight of the wing, and weight of the motors, as illustrated in Figure 3.29. Subsequently, the bending moment along the wing is determined both with and without the presence of the strut. To ensure a conservative estimate for the wing-strut configuration, a constant inboard loading assumption is made beyond the strut, as depicted in Figure 3.30. The area between the two curves represents the percentage decrease in wing weight.
The strut is assumed as a simple beam given in Figure 3.31 and the dimensions of the strut are defined due to the Buckling criteria as seen in equation 3.13. The weight is calculated simply with equation 3.14.

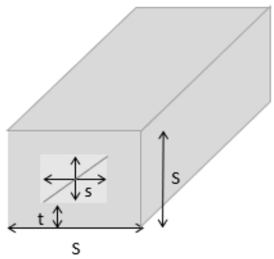

Figure 3.31: Strut beam shape

$$\mathrm{P_{cr}} = \frac{\pi^2 EI}{(\,\mathrm{K}L)^2} \tag{3.13}$$

Where P_{cr} is the critical load for buckling, E is Young‘s modulus, I is inertia, L is the length and K is the effective length factor.

$$W_{\text{strut}} = \rho \cdot VF \tag{3.14}$$

Where ρ is density and V is the Volume of the strut and F is a factor for secondary structures (brackets, fittings, leading edge, trailing edges, and manufacturing tolerances).

3.6.2.1 Load factor

Load factor gives the stress measure to which the aircraft is subjected due to the condition of flight and manoeuvring. The bending moment is calculated due to the +G condition at level flight. For this reason, a loading factor should be applied for the critical condition where Buckling is effective as the designing criteria is selected as Buckling in the weight estimation methodology for strut. A generic load factor graph is given in Figure 3.32. The load factor for this study is defined as -1 as the -G condition is critical for buckling criteria.

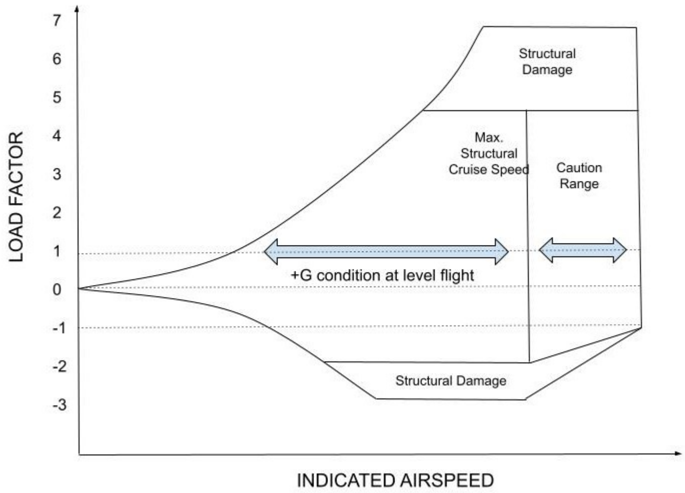

Figure 3.32: Generic Load factor graph

3.6.3 General Assumptions of weight calculation

General assumptions:

1. Ultimate load factor is used for -G condition which is 1.5 times of load factor.
2. There is a linear behaviour in the Bending moment between Bone and strut as shown in Figure 3.33.
3. There is a linear behaviour in the Bending moment between the wing tip and strut as shown in Figure 3.33.
4. Effective length factor (K) is assumed 1 for Buckling criteria.
5. The safety factor for strut force is 1.5.
6. Factor for secondary structures (brackets, fittings, leading edge, trailing edges, and manufacturing tolerances) is 1.4.

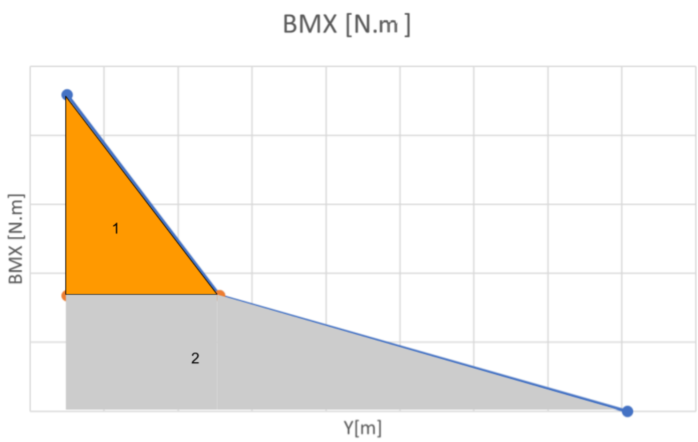

Figure 3.33: Assumed Spanwise BMX distribution

3.6.4 Bending Moment

For the weight estimation, the wing is divided into regions based on their x-axis (BMX) bending moments. Critical points along the spanwise locations, where the wing and strut are joined and where the bone is located, are used to select the regions. Such locations can be observed in Figure 3.34. The bending moment contribution generated by the lift is calculated using AVL output (FN.out), which provides the local lift coefficient of every strip (panel). The output file of AVL gives the local lift coefficient, spanwise location of each strip's midpoint, and area of each strip. The dynamic pressure is calculated as 696 N/m^2. Therefore, by using the Area, local lift coefficient and dynamic pressure, the lift force that is generated on every strip is calculated. The bending moment contribution from each strip's lift is found by multiplying the lift force exerted on the strip by the distance between the strut and the strip's midpoint for region 1. This calculation is repeated for region 2 using the distance between the bone and the strip's midpoint. The bending moment contribution from the overall lift is computed by summing all the bending moment contributions from each strip's lift at the BMX sections.

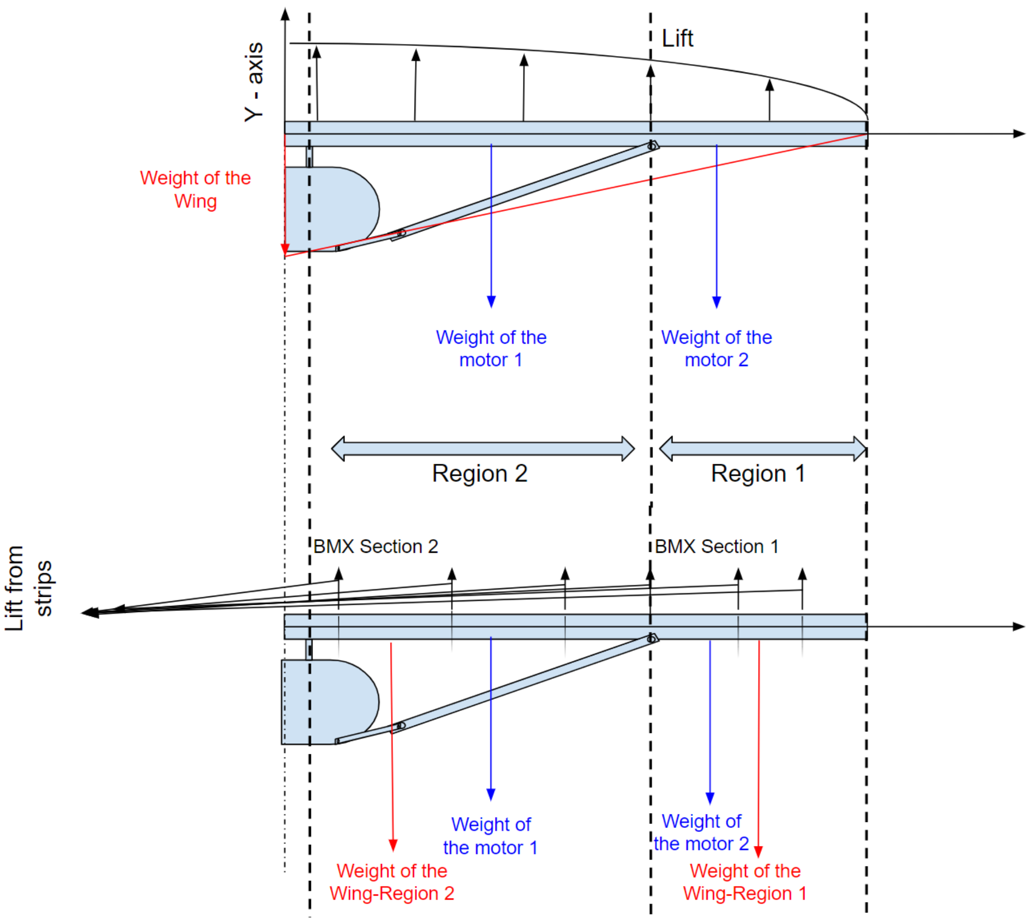

Figure 3.34: Regions and point forces for Bending Moment calculation

The total wing weight is calculated directly using Equation 3.12 proposed by Raymer. The ultimate load factor is assumed to be 1.5, as the bending moment calculation is done for the +G condition first. The surface area (S_{ref}) is 75.77 m^2, and the aspect ratio (AR) is found through the optimization process.

The bending moment contribution from the weight of the wing is calculated per region. For region 1, the total weight of the region is assumed to have a triangular weight distribution throughout the wing, as shown in Figure 3.34. The center of gravity is calculated based on the triangle geometry and converted to a point force from the center of gravity. The bending moment is calculated using the weight and the distance between the center of gravity and the joint of the strut and wing. The calculation for region 2 is repeated with the center of gravity of the trapezoid, weight of region 2, and the distance between the center of gravity of region 2 and the bone.

The bending moment contribution from the motors is calculated with some assumptions. The first assumption is that the concept has four motors, two per each side of the wing-strut. Furthermore, as the motor weights and spanwise locations are unknown, assumptions listed in Table 3.5 are made. The bending moment contribution from the motors is calculated with the weight and the distance between the spanwise location where the strut is positioned and the location of the motor for region 1. The calculation for region 2 is repeated with the distance between the bone and the motor. It should be noted that the location of two motors changes as the region changes with the position of the strut.

Table 3.5: Assumptions for motor

Element	**Value**	**Unit**
W_{motor_1}	1420	N
y_{motor_1}	3	m
W_{motor_2}	1420	N
y_{motor_2}	7.5	m

Where W_{motor_1} is the weight of motor 1, W_{motor_2} is the weight of motor 2, y_{motor_1} is the spanwise location of the motor 1 and y_{motor_2} is the spanwise location of the motor 2 with respect to the root of the wing.

To summarize, the bending moment in section 1 is determined considering contributions from lift, wing weight, and motor weight. In section 2, the bending moment includes contributions from lift, wing weight, motor weight, inboard bending moment from region 1, and inboard shear force from region 1. By calculating the bending moment at the bone location and the joint at the wing-strut location, the percentage change in wing weight can be determined by evaluating the area between the curves for region 1 and the combined area for regions 1 and 2.

3.6.5 Force on the strut

The critical strut force is determined by calculating the bending moment at the bone in -G condition which is obtained with using the ultimate load factor. To find the force that is effective at the strut location, the bending moment at the bone is divided by the distance between the bone and the strut. This division results in the force on the y-axis, as illustrated in Figure 3.35. To determine the force acting on the strut, the sine of the force on the y-axis is multiplied by the dihedral angle of the strut. The critical force is then calculated by applying a safety factor which is defined as 1.5 to the force acting on the strut.

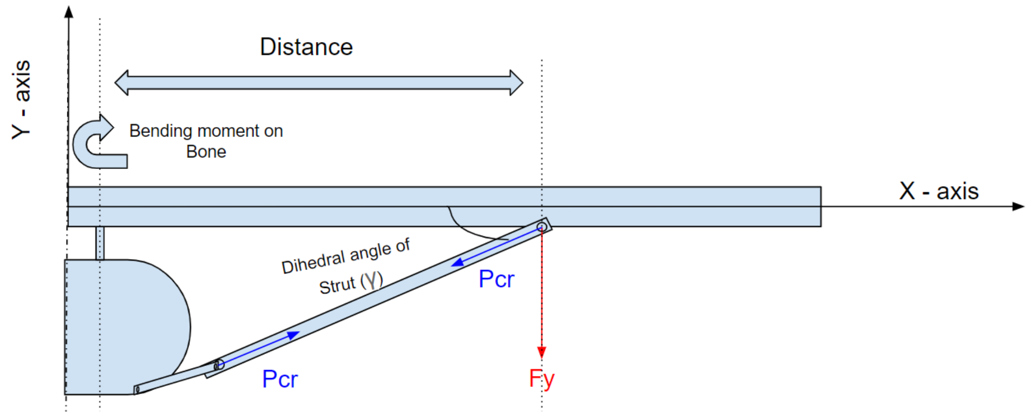

Figure 3.35: Force acting on strut

3.6.6 Total Weight of the SBW

Inertia is calculated using equation 3.13 and the geometric inertia with equation 3.15. The thickness is changed until both inertia are the same. The volume is calculated using the calculated thickness, the 240 mm height, and the length of the strut which is found from the optimizer. The material of the strut is assumed to be Al 7075 which has a density of 2850 kg/m3. The weight is calculated by multiplying the volume and density. The total weight of the SBW is found by summing the weight of the wing, which has a percentage decrease applied, and the weight of the strut.

$$I = \frac{S^4 - (S - (2 * t))^4}{12} \tag{3.15}$$

$$t = \frac{S - (S^4 - 12I)^{1/4}}{2} \tag{3.16}$$

Where S is the height of the beam and t is the thickness of the beam as given in Figure 3.31. The height (S) is assumed 240 mm and the length is used as the strut length from optimization.

4

Results and Discussion

This chapter serves as a comprehensive platform for the presentation and in-depth discussion of the results obtained in this thesis. It encompasses a thorough analysis and interpretation of the findings, enabling a deeper understanding of the research objectives and outcomes. The chapter's structure and organization are illustrated in the accompanying flowchart, depicted in Figure 4.1.

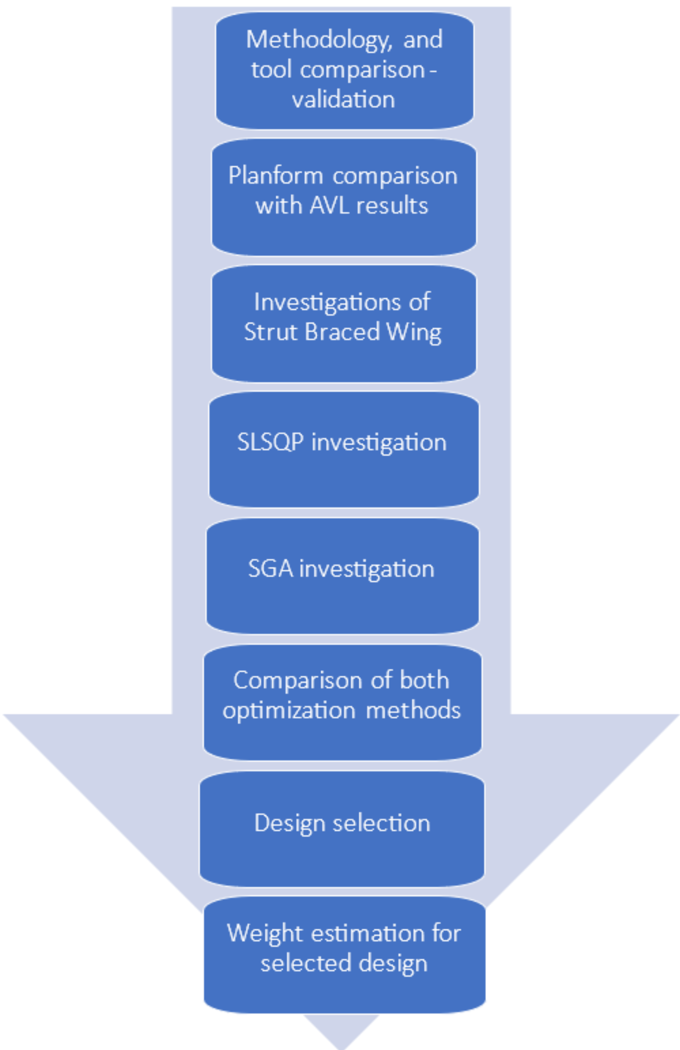

Figure 4.1: Result section flowchart

4.1 XFOIL Validation

Lift and Drag coefficients for different AoA are obtained with XFOIL software as seen in Figures 4.2, 4.3, and 4.4. The simulation was set to be carried out for a flow with Reynolds number $2 \cdot 10^6$ at 0.15 Mach, in order to compare with available experimental values taken from previous Wind Tunnel tests performed by [59].

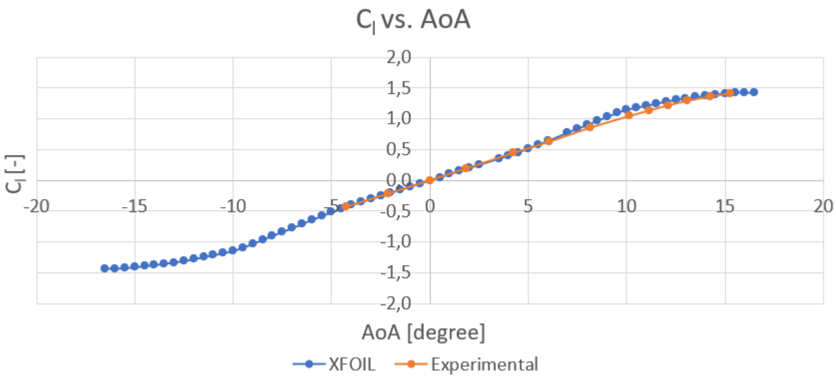

Figure 4.2: C_l vs. AoA comparison between XFOIL and wind tunnel data for NACA0012 @ $Re = 2 \cdot 10^6$, $M = 0.15$

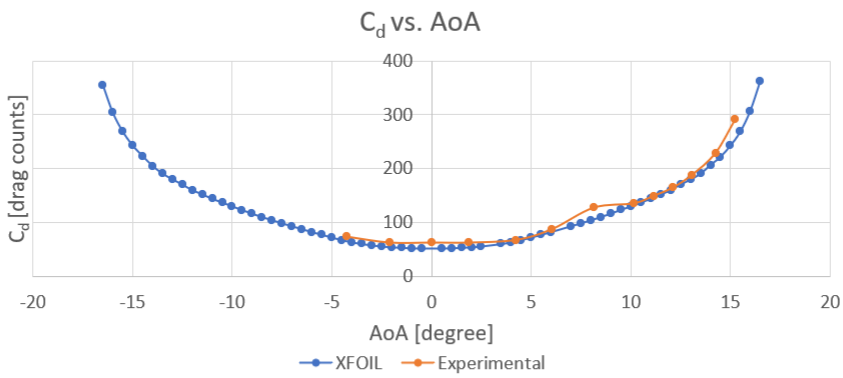

Figure 4.3: C_d vs. AoA comparison between XFOIL and wind tunnel data for NACA0012 @ $Re = 2 \cdot 10^6$, $M = 0.15$

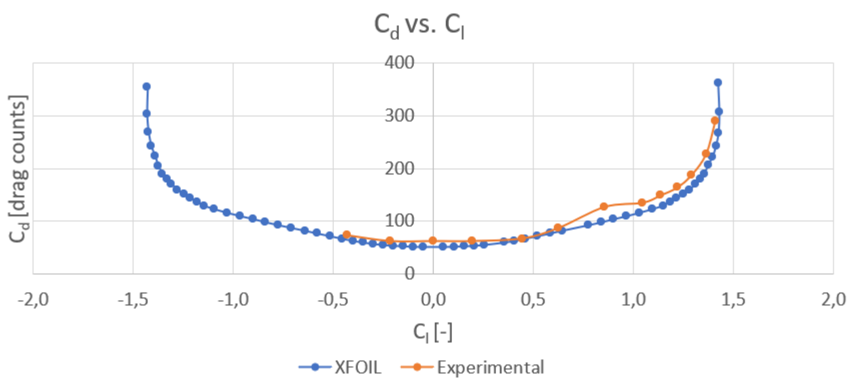

Figure 4.4: C_d vs. C_l comparison between XFOIL and wind tunnel data for NACA0012 @ $Re = 2 \cdot 10^6$, $M = 0.15$

The experimental value has a limited range in terms of AoA, as just accounts for a limited portion of the negative AoA. The highest difference between XFOIL and experimental results is 12 % for C_d and 1 % for C_l. The difference in Drag could be caused because of installation effects on Wind Tunnel results.

Moreover, pressure distribution over the airfoil is calculated for XFOIL, StarCCM+, and compared with experimental values taken from previous Wind Tunnel study [60]. The fluid properties for such study were a Reynolds number of 3x10^6 and an AoA of 0. However, StarCCM+ and XFOIL results are for a Reynolds number $2.24 \cdot 10^6$ which is the flight condition for reference aircraft. The results are given in Figure 4.5.

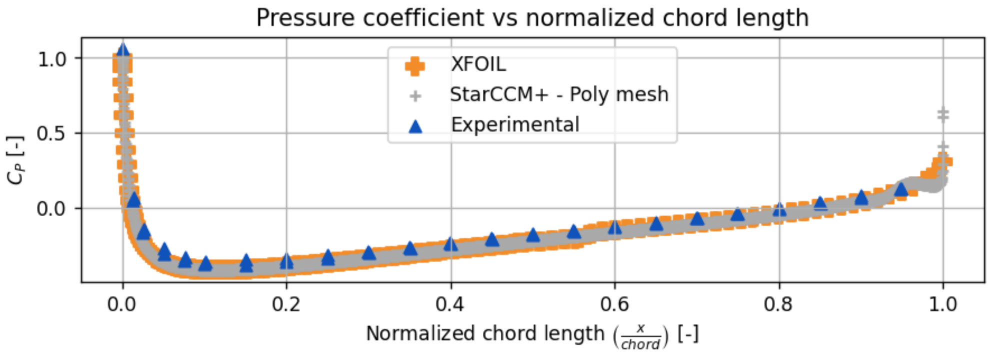

Figure 4.5: NACA0012 Pressure distribution over airfoil from evaluated sources

In the results, the experimental and XFOIL results are relatively close, with a maximum difference of approximately 10%. However, there is a significant difference of approximately 50% between the results given by StarCCM+ and XFOIL results near the trailing edge. XFOIL produces closer values to experimental results compared to StarCCM+ on the leading and trailing edges, but the pressure coefficient values between the leading edge and trailing edge are nearly the same for the three sets. In summary, the average error between experimental results and XFOIL is 5% for C_d, 0.5% for C_l, and 8% for C_P, which is lower than 10%. Although StarCCM+ results are similar to XFOIL results, they have a higher dependency on mesh and are considerably more computationally expensive.

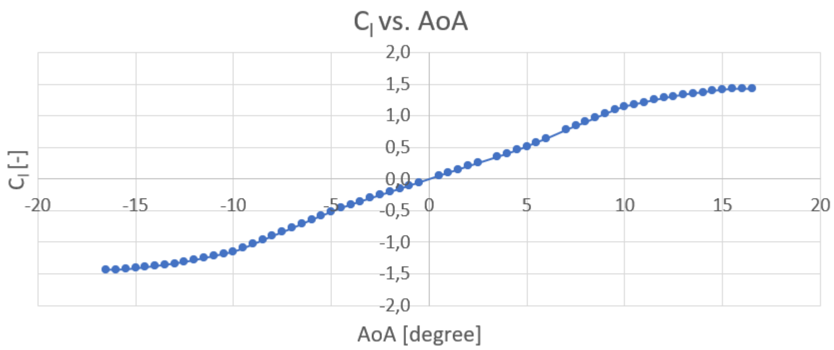

Figure 4.6: C_l vs. AoA comparison generated with XFOIL NACA0012 @ $Re = 2.24 \cdot 10^6$, $M = 0.1$

The reference aircraft's cruise Mach number will be 0.1 and the Reynolds number is calculated as $2.24 \cdot 10^6$. The C_l and C_d values used for the simulations are given in Figures 4.6, 4.7, and 4.8.

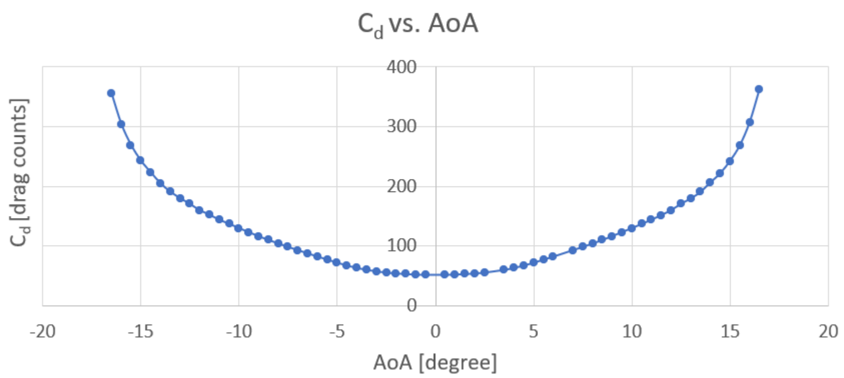

Figure 4.7: C_d vs. AoA comparison generated with XFOIL NACA0012 @ $Re = 2.24 \cdot 10^6$, $M = 0.1$

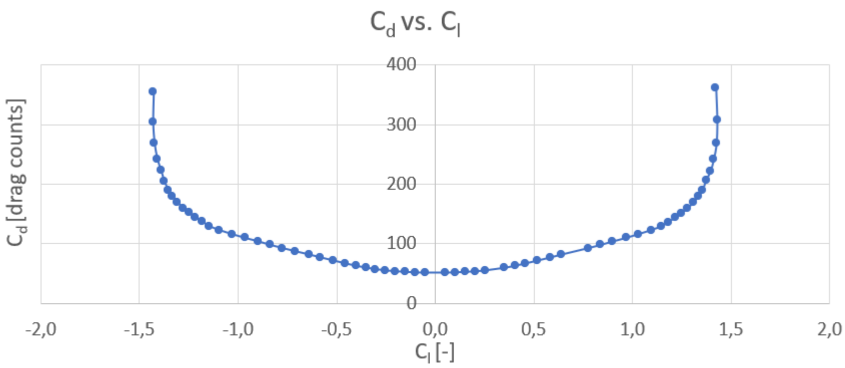

Figure 4.8: C_d vs. C_l comparison generated with XFOIL NACA0012 @ $Re = 2.24 \cdot 10^6$, $M = 0.1$

4.2 Tools and methods comparison

In this section, a comparison study for all the considered options is presented. The objective was to select the most appropriate tool for the optimization process in the conceptual design stage in terms of accuracy, time complexity and setup complexity. In the study, 3 different tools and 4 different methods are considered. The tool-methods setups are given in the form tool (method); StarCCM+ (Euler equation), OpenVSP (Panel method), OpenVSP (VLM) and AVL (Extended-VLM). The cases are run for Angles of Attack between -16 to 16 for each method and aerodynamic coefficients are exported from each tool. The simulations were done using the same tapered wing planform properties; a span of 32.3 m, a root chord of 3.193 m, a taper ratio of 0.469, and a reference area of 75.77 m^2. The results can be observed in Figures 4.9, and 4.10.

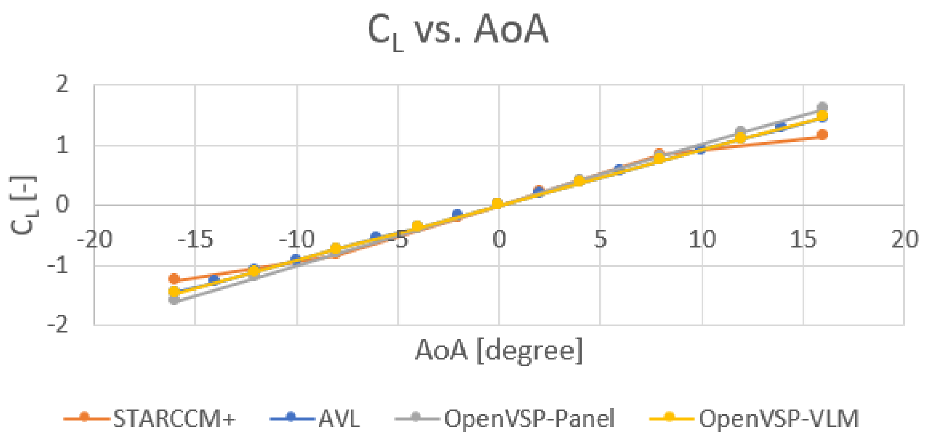

Figure 4.9: C_L vs. AoA graph for different tools

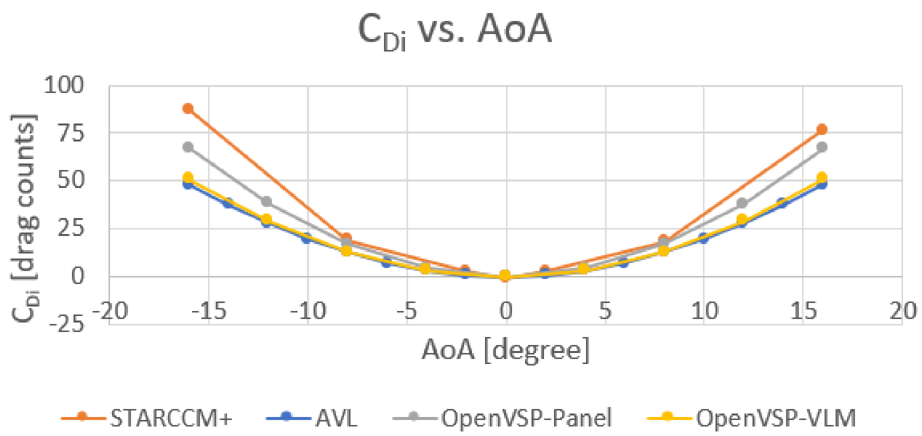

Figure 4.10: C_{D_i} vs AoA graph for different tools

The difference between tools slightly increases as the AoA value increases, it becomes considerably higher after the AoA value of 8 degrees. OpenVSP using the VLM method and AVL have the lowest difference in C_L and C_{D_i} in drag counts, those results are expected as both tools use the same methodology. Furthermore, it clarifies that VLM method for both tools gives stable solutions. In StarCCM+, non-physical separation can be observed in Figures 4.11 and 4.12 in the results for higher AoAs. Moreover, a difference is also observed between VLM and Panel methods, this could also be caused by differences in the formulation of each method.

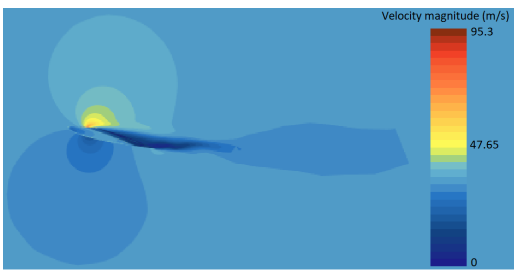

Figure 4.11: StarCCM+ velocity scalar for 16 AoA. Source: Star-CCM+ [55]

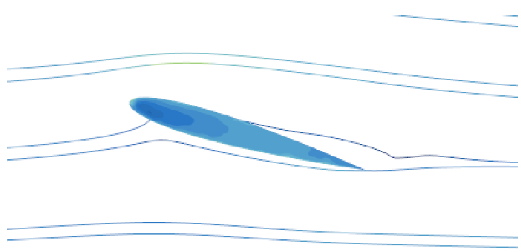

Figure 4.12: Streamlines over the airfoil for 16 AoA. Source: Star-CCM+ [55]

In summary, StarCCM+ requires significant computational power and exhibits numerical separation at high angles of attack, while the Panel method demands less computational resources and provides similar results. Therefore, the Vortex Lattice Method (VLM) emerges as the optimal choice for conceptual design, striking a balance between accuracy and computational cost. Additionally, AVL's interface offers better interaction with Python, enhancing the usability of the software for optimization.

4.3 Wing planform comparison

Different wing planforms were considered in this work, a comparison between them was done and is presented in this section. For the comparison, the same aspect ratio, reference area, taper ratio and span were set up. The target value for C_L was set up as 0.8. The comparison was made based on the drag coefficient at the far field ($C_{D_{ff}}$) calculated from the Trefftz plot. The results are summarized in Table 4.1.

In Table 4.1, the best wing planform in terms of induced drag can be identified as the elliptical. This result agrees with a previous study that suggests the uniform lift distribution shown by the elliptical wing planform gives the minimum induced drag [61]. The tapered elliptical and trapezoidal wing planforms achieved similar values for drag as the lift distribution for both is alike as seen in Figure 4.13. Moreover, analyzing both Table 4.1 and Figure 4.13 is possible to observe the relation between lift distribution and induced drag. The induced drag for a given wing planform will be lower as its lift distribution is closer to the one for the elliptical wing planform.

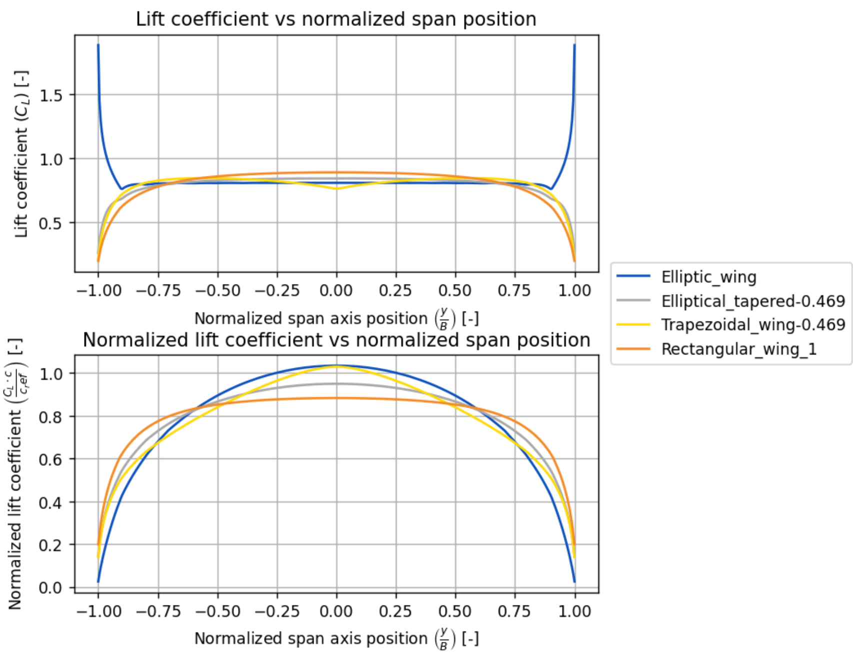

Figure 4.13: Lift distribution comparison for different Wing Planforms

Table 4.1: Comparison table for different Wing planforms

Geometry	**AR** [-]	$\mathbf{S_{ref}}$ [$\mathbf{m^2}$]	λ [-]	**B** [m]	$\mathbf{C_L}$ [-]	$\mathbf{C_{D_{ff}}}$ [drag counts]
Trapezoidal Wing	13.77	75.77	0.469	32.3	0.8	149.904
Tapered Elliptical	13.77	75.77	0.469	32.3	0.8	150.966
Fully Elliptic	13.77	75.77	0	32.3	0.8	147.104
Rectangle	13.77	75.77	1	32.3	0.8	157.686

4.4 Relation between Reference Area and Drag for SBW

In this section, a study intended to explain the relationship between the reference area and total drag is presented for a strut braced wing. A tapered wing planform type with a span of 32.3 m, chord root of 3.193 m, a taper ratio of 0.469, and a reference area of 75.77 m^2 was used. The proportions of the strut were fixed as well, with the only difference being the variation in the dihedral angle, which leads to a variation of the strut length.

Six simulations in total were conducted for the two scenarios, with three different strut angles for each scenario. The designs for strut-braced wings (SBW) with the three selected values for strut dihedral angles are illustrated in Figure 4.13. The reference area used for this study was fixed as the value of the wing planform for the first scenario. For the second scenario the area of the struts will be added to the wing planform area excluding the contribution from the fairing, the lift coefficient was adjusted to maintain a constant lift force. The results of the comparison study are presented in Tables 4.2 and 4.3.

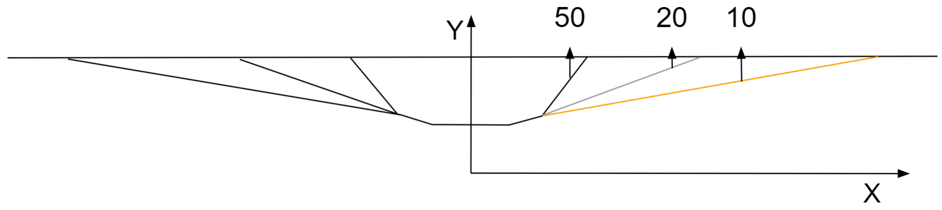

Figure 4.14: SBW design for different strut dihedral angles

Table 4.2: Change in total drag when the reference area is defined as the area of the wing

Lift x $\mathbf{q_\infty}$	**Strut Dihedral angle** [degree]	$\mathbf{S_{ref}}$ [$\mathbf{m^2}$]	$\mathbf{C_L}$ [$-$]	**Wing** $\mathbf{C_L}$ [$-$]	**Strut** $\mathbf{C_L}$ [$-$]	**Contri-bution of strut to** $\mathbf{C_L}$ [%]	$\mathbf{C_{D_{tot}}}$ [drag counts]	$\mathbf{\Delta C_{D_{tot}}}$ (Baseline 50 degrees) [%]
60.62	10	75.78	0.80	0.69	0.11	13.83	989.00	-13.36
60.62	20	75.78	0.80	0.75	0.05	5.78	1079.00	-5.47
60.62	50	75.78	0.80	0.79	0.01	1.03	1141.50	-

Where q_∞ is dynamic pressure and $C_{D_{tot}}$ is total drag expressed as drag counts.

From the first scenario, it can be observed that total drag ($C_{D_{tot}}$) is proportional to the strut dihedral angle, or inversely proportional to the strut area. The variation of the total drag in the range [-14,-5] % for a strut dihedral range [10,50] degrees. Further elaboration on this matter will be provided in the current section.

Table 4.3: Change in total drag when the reference area is defined as the sum of the areas of the strut and wing

Lift x $\mathbf{q_\infty}$	**Strut Dihedral angle [degree]**	**$\mathbf{S_{ref}}$ [$\mathbf{m^2}$]**	**$\mathbf{C_L}$** [−]	**Wing $\mathbf{C_L}$** [−]	**Strut $\mathbf{C_L}$** [−]	**Contri-bution of strut to $\mathbf{C_L}$** [%]	**$\mathbf{C_{D_{tot}}}$ [drag counts]**	**$\mathbf{\Delta C_{D_{tot}}}$** (Baseline 50 degrees) [%]
60.62	10	100.22	0.60	0.52	0.08	13.72	736.20	-27.53
60.62	20	90.94	0.67	0.63	0.04	5.79	907.50	-10.66
60.62	50	85.64	0.71	0.70	0.01	1.05	1015.80	-

Where q_∞ is dynamic pressure and $C_{D_{tot}}$ is total drag expressed as drag counts.

It can be observed from the second scenario, that the correlation between total drag, strut dihedral angle and strut area is still proportional and inversely proportional respectively, as expected. The change when strut contribution is included in the reference area, with the appropriate lift coefficient (C_L) recalculation is within the range (-28,-10) % for a strut dihedral range (10,50) degrees.

Comparing the results from both scenarios from the perspective of lift contribution, it can be concluded that for both scenarios more than 85 % of the lift is generated from the wing. Furthermore, regardless of the scenario, the contribution of lift from each surface was calculated correctly by AVL. Moreover, the difference between the total drag for the same dihedral angle for both scenarios is proportional to the ratio of the areas of the scenario. This can be seen in Table 4.4.

Table 4.4: Variation in total drag comparison between reference area based on the wing vs when the reference area is based on wing and strut

Strut Dihedral angle [degree]	**$\mathbf{C_{D_{tot}}}$ Constant Area [drag counts]**	**$\mathbf{C_{D_{tot}}}$ Varying Area [drag counts]**	**$\mathbf{\Delta C_{D_{tot}}}$** [%]
10	989.00	736.20	25.56
20	1079.00	907.5	15.89
50	1141.50	1015.8	6.85

In summary, the absolute change in total drag can have a significant effect on the results due to the contribution of the strut to lift. The variation in total drag between simulations with different reference areas and different strut dihedral angles is around 5-10%. To increase the simplicity, and reduce the computational cost and code complexity, it is advisable to use the same reference area and lift coefficient in simulations while optimizing the strut-braced wing design. Therefore, a reference area of 75.77 m^2 and a lift coefficient of 0.8 was used for all simulations.

4.5 Oswald efficiency investigation

In this section, the results of the Oswald efficiency study for a strut braced wing are presented. A tapered wing planform with a span of 32.3 m, chord root of 3.193 m, a taper ratio of 0.469, and a reference area of 75.77 m^2 with strut is analyzed through simulations conducted at different lift coefficients (C_L) values. Similarly as mentioned in previous sections, the fairing contribution is not counted in this study. Moreover, the Oswald efficiencies for different strut dihedral angles are compared. The Oswald efficiency is obtained from two sources; the first one is by the means of the equation of the slope for a linear function from the graph C_{D_i} vs. C_L^2 for each surface from the FN files named 'e-Graph', the second source is the overall Oswald efficiency for all the surfaces from the FT files, named 'e-AVL'. The results are presented in Figures 4.15 and 4.16, and Table 4.5.

Table 4.5: Oswald efficiency values for surface and surface group for both sources

Surface	**Angular coefficient** $\mathbf{C_D/C_L^2}$ [−]	**AR** [−]	**e (Graph)** [−]	**e (AVL)** [−]	$\mathbf{\Delta e}$ [%]
Wing	0.025	13.77	0.925	-	-
Strut	0.4027	13.77	0.057	-	-
Wing + Strut ($C_{D_{ff}}$)	0.0247	13.77	0.936	0.942	0.65

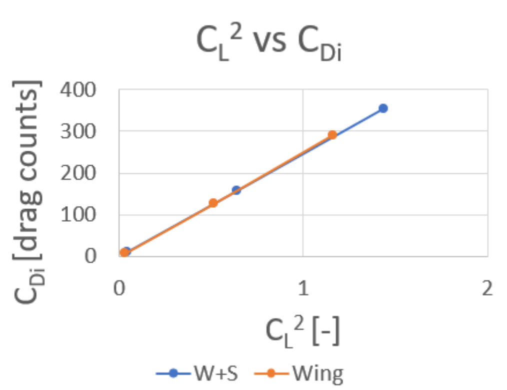

Figure 4.15: Oswald efficiency values for wing and wing+strut surfaces from FN file

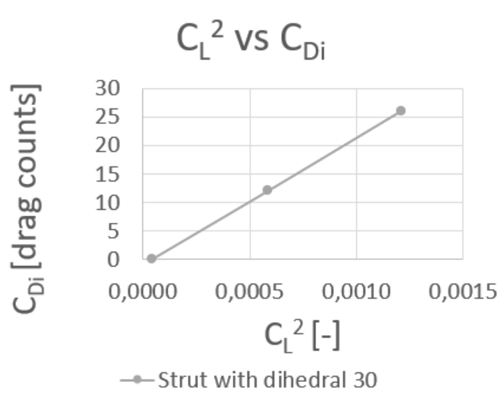

Figure 4.16: Oswald efficiency values for strut surface from FN file with different scale

As indicated in Table 4.5, a disparity can be observed in the Oswald efficiencies obtained from the two sources, with a marginal variation of approximately 0.65%.

It is relevant to note that the Oswald efficiency is only computed for the surface group by AVL, therefore the values for each surface are not available for comparison. A further discussion about Oswald efficiency calculation with different methodologies is given in Appendix A.4. Moreover, it can be observed that the Oswald efficiency of the strut is considerably lower when compared with the wing. This can be seen in Figures 4.15 and 4.16, it is important to note that the vertical axis located on the left is used to plot the values for the strut, while the axis of the right is used to plot the values for the wing and the wing+strut. Hence, generating lift from the wing is considerably more efficient than from the strut.

Looking up to the strut dihedral angle effect in Oswald efficiency, several values of this property were evaluated. Three values in total were considered; 10, 30, and 50 degrees. The results are shown in Figure 4.17. As observed, the Oswald efficiency increases as the strut dihedral angle decreases. This is expected, as the dihedral angle increases the span and the area of the strut increases while the chord of the strut is constant.

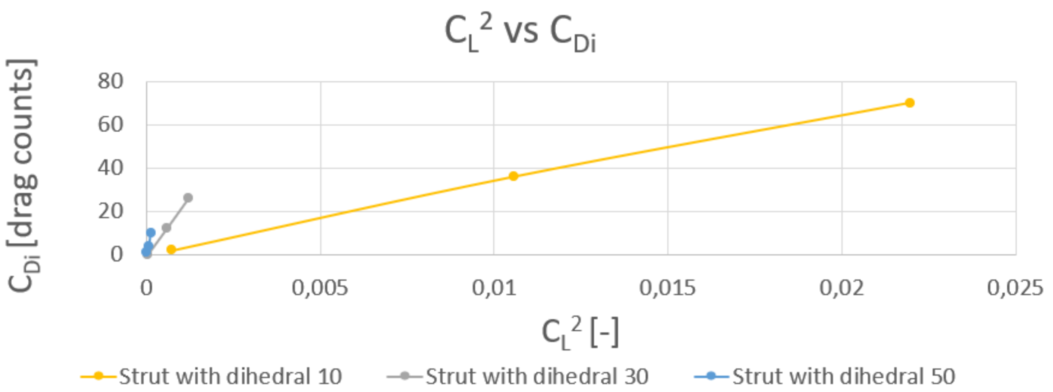

Figure 4.17: Oswald efficiency of different strut dihedral angles

4.6 Strut dihedral influence in aerodynamic coefficients investigation

Different strut dihedral angles were studied to investigate their effect on the behaviour of the wing and strut. Figure 4.18 shows the variation in strut dihedral angle considered for this evaluation. The aerodynamic coefficients were computed for different dihedral angles of the strut with a tapered wing having a span of 32.3 m, a root chord of 3.193 m, a taper ratio of 0.469, and a reference area of 75.77 m^2. The target C_L for the simulations was set to 0.0, and 0.8. Moreover, as part of the evaluation strategy, the lift contribution for the fairing was disregarded for the total forces. The twist angles for the strut and wing were set as 0 and kept constant throughout the evaluation. The resulting aerodynamic coefficients from the simulations are presented in Figures 4.19 for $C_L = 0.0$, and 4.20 for $C_L = 0.8$.

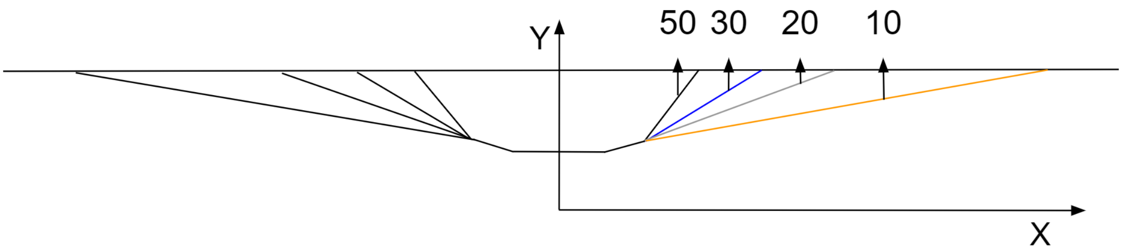

Figure 4.18: Dihedral change in the strut

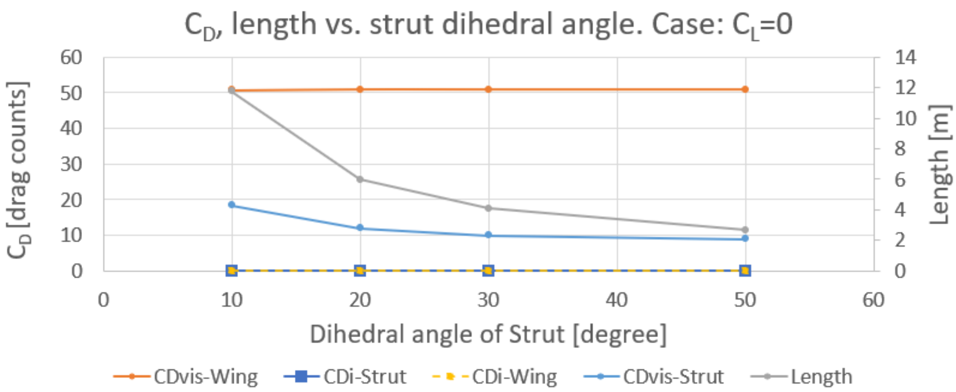

Figure 4.19: C_D and strut length vs strut dihedral angle for the case $C_L = 0$. where C_D represents the drag coefficients and the values are plotted with reference to the left vertical axis, and 'Length' is the length of the one strut and the values for this series are plotted with respect to the right vertical axis.

For the case $C_L = 0$, both strut and wing generate zero C_L. Hence, the induced drag for both surfaces is zero, as expected. As can be seen in Figure 4.19, the viscous drag decreases as the length decreases as expected, because the skin friction drag is proportional to the wetted area, which decreases when the dihedral angle increases.

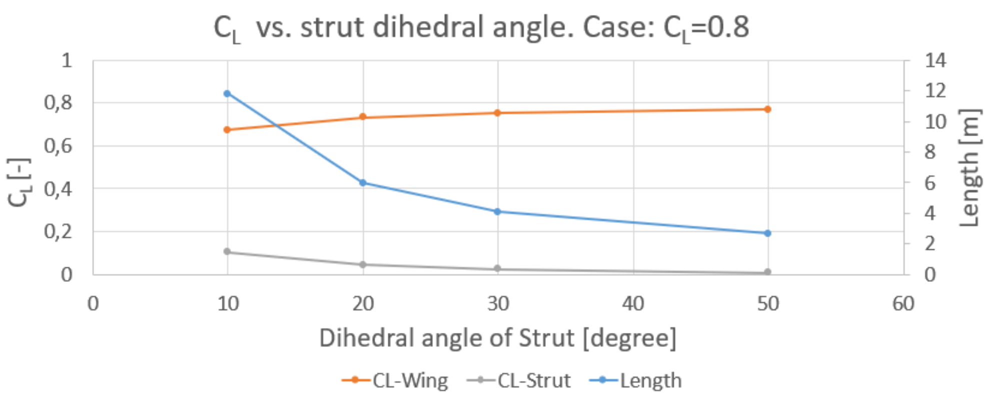

Figure 4.20: C_L and strut length vs strut dihedral angle for the case $C_L = 0.8$ where C_L represents the lift coefficients for each surface and the values are plotted with reference to the left vertical axis, and 'Length' is the length of the one strut and the values for this series are plotted with respect to the right vertical axis.

In Figure 4.20, it is observed that the wing contribution to C_L decreases as the dihedral angle of the strut decreases. This means that the strut generates more lift when the dihedral angle of the strut decreases, this change in the contribution of lift affects the Drag coefficient of both surfaces. When the dihedral angle of the strut decreases, the expected behaviour is an increase in the total drag for both surfaces. The previous is due to the increase in the length of the strut, which increases the skin friction drag.

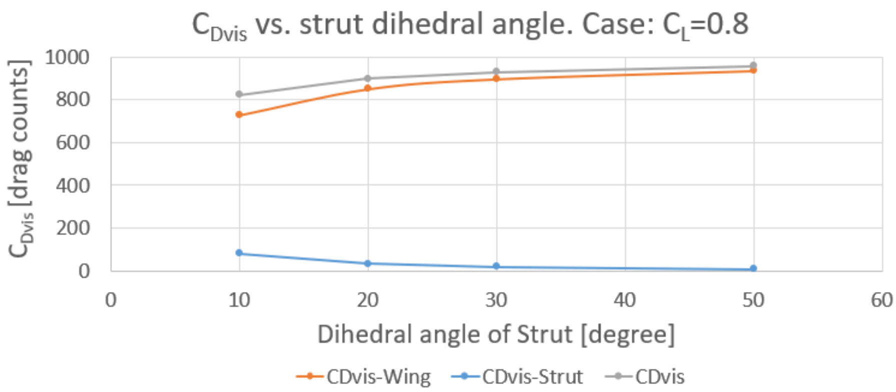

Figure 4.21: $C_{D_{vis}}$ and strut length vs strut dihedral angle for the case $C_L = 0.8$

However, the wing generates less lift with decreasing dihedral angle of the strut, as the lift contribution of the strut increases. Hence, the viscous drag of the wing decreases when the dihedral angle of the strut is decreasing due to lower AoA required to achieve the target C_L as seen in Figure 4.21. For the strut, viscous drag increases as the lift contribution from the strut increases with decreasing dihedral angle. For both surfaces, the total viscous drag is lower as the viscous drag drop of the wing is bigger than the increase in viscous drag of the strut. This effect could be analysed with the profile Lift Drag curve as seen in Figure 4.22.

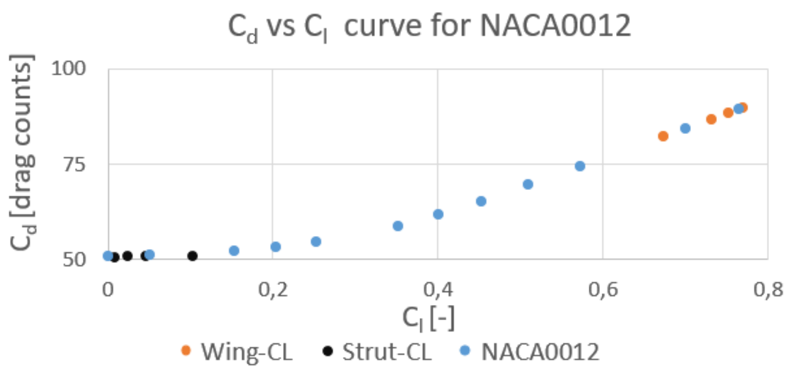

Figure 4.22: Wing and strut C_L and C_D in the NACA0012 profile C_d vs. C_l graph for four different values of strut dihedral angle

where 'strut-C_L' series is the lift coefficient of the strut for different dihedral angles with its corresponding profile drag coefficient in NACA0012, and 'wing-C_L' series is the lift coefficient of the wing with its corresponding profile drag coefficient in NACA0012.

In Figure 4.22, the main objective is to illustrate the regions where the wing and the strut lift and drag coefficients are located for each strut dihedral angle considering the NACA0012 profile. The wing contribution to the lift is higher than the strut, therefore it is located in the region where the C_l is higher for the NACA0012 profile. For the wing C_L, the local lift along the wing spanwise is located in a region where the C_d/C_l ratio has an approximate value of 0.0075. Conversely, the strut C_L yields lower C_l values, in this low C_l region, the C_d changes are almost negligible when compared to the changes in C_l, with a c_d/c_l ratio with an approximate value of 0.00025. This means, that the c_d/c_l ratio in the wing C_L region is approximately 30 times higher than the strut C_L region. As a result, the impact of wing C_L has a more significant effect on the total drag compared to the change in the strut drag.

The primary effect from the wing arises from the contribution of pressure drag, with the skin friction drag remaining constant due to the unchanged geometry. In contrast, both the skin friction drag and viscous drag play a significant role in the strut as the geometry undergoes changes.

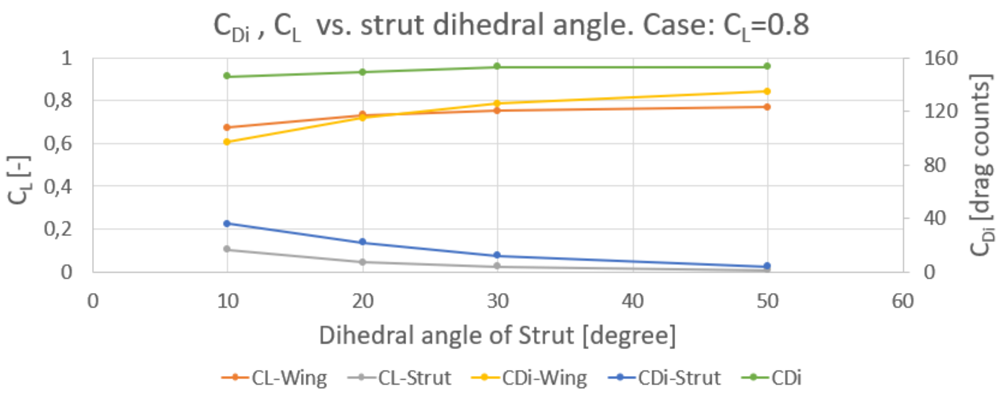

Figure 4.23: C_{D_i}, C_L vs strut dihedral angle for the case $C_L = 0.8$

The induced drag is influenced by variations in the strut dihedral angle, as these changes affect the lift contributions. This relationship can be observed in Figure 4.23. The change in the lift coefficient (C_L) exhibits a similar pattern to the variation in the induced drag coefficient (C_{D_i}) for the wing. However, in the case of the strut, the curve deviates slightly due to the improvement in Oswald efficiency resulting from a decrease in dihedral angle, as discussed in Section 4.5. Furthermore, the total induced drag decreases as the strut dihedral angle decreases, as the Oswald efficiency is impacted by changes in this parameter. This effect can be seen in Table 4.6. The Lift distributions of the 10-degree strut dihedral angle and 50-degree strut dihedral angle are given in Appendix A.3.

Table 4.6: Induced and viscous drag breakdown for each surface and joint surfaces

Surface	$C_{D_{vis}}$ (Dihedral 10) [drag counts]	$C_{D_{vis}}$ (Dihedral 50) [drag counts]	C_{D_i} (Dihedral 10) [drag counts]	C_{D_i} (Dihedral 50) [drag counts]	$\Delta C_{D_{vis}}$ [drag counts]	ΔC_{D_i} [drag counts]	Total change [drag counts]
Wing	727	936	97	135	-209	-38	-247
Strut	80	8	36	4	72	32	104
Total	-	-	-	-	-137	-6	-143

4.7 Strut dihedral and local geometrical incidence influence in aerodynamic coefficients investigation

Six test cases were conducted using AVL to assess the impact of local geometrical incidence on both the wing and the strut. These test cases consisted of three scenarios with a strut dihedral angle of 10.4 degrees and three scenarios with a strut dihedral angle of 50 degrees. Each strut dihedral angle was combined with three different local geometrical incidence combinations: (0,0) for the wing and strut, (10,0) for the wing and strut, and (0,10) for the wing and strut. The local geometrical incidence values for both the wing and the strut remained constant across the surfaces. The investigation was based on a tapered wing with the following planform properties: a span of 32.3 m, a root chord of 3.193 m, a taper ratio of 0.469, and a reference area of 75.77 m^2. The target lift coefficient (C_L) for the simulations was set to 0.8. Furthermore, as part of the evaluation strategy, the lift contribution of the fairing was excluded from the total forces analysis.

Table 4.7: Local geometrical incidence of wing, local geometrical incidence of strut and dihedral of strut

Test number	Wing local geometrical incidence [degree]	Strut local geometrical incidence [degree]	Strut dihedral [degree]	$\Delta C_{D_{tot}}$ [drag counts]	$\Delta C_{D_{ff}}$ [drag counts]
1	0	0	10.4	993.8	151.7
2	10	0	10.4	1474.4	147.1
3	0	10	10.4	1434.2	169.8
4	0	0	50	1141.0	152.1
5	10	0	50	1181.8	143.2
6	0	10	50	1171.5	163.2

Table 4.7 demonstrates that the relationship between the dihedral angle of the strut and total drag is not solely dependent on the angle itself. It is also influenced by the local geometrical incidence, which affects the lift generated by the wing and strut. A

comparison between Test numbers 5 and 6 reveals that when the local geometrical incidence of the wing is high, the total drag increases by 1.02% due to the increased lift generated by the wing and the smaller size of the strut, resulting in higher pressure and viscous drag, as discussed in Section 4.6. Furthermore, comparing the change between Tests 3 and 6 with the change between Tests 2 and 5, it can be observed that the total drag change is 18.34% between tests 3 and 6. However, the difference between Test 2 and 5 is 19.74%, indicating the significant contribution of the wing's lift to the overall change in total drag.

In the scenarios where the wing generates lower lift; incidence set as 0, or strut dihedral 10.4 degrees the drag is considerably lower than the other conditions. This behaviour is due to C_L vs. C_D graphs behaviour/shape. For a more detailed analysis, a Design of Experiments is shown as seen in Section 4.7.1.

4.7.1 Design of Experiments (DOE) - incidence

A study was carried out for the local geometrical incidence of the wing, the local geometrical incidence of the strut, and the strut dihedral in terms of induced drag, viscous drag and total drag. The Latin Hypercube Sampling (LHS) method was employed as part of a rigorous Design of Experiments (DOE) methodology. This study used the same setup, conditions, and considerations mentioned in Section 4.7. The set-up for the LHS array was; 230 samples, centred values in the Stratas, the range for the wing local geometrical incidence [-5,15] in degrees, the range for the strut local geometrical incidence [-5,15] in degrees, the range for the strut dihedral [10.4,50] in degrees. The results of the studies are given in Figures 4.24, 4.25, and 4.26.

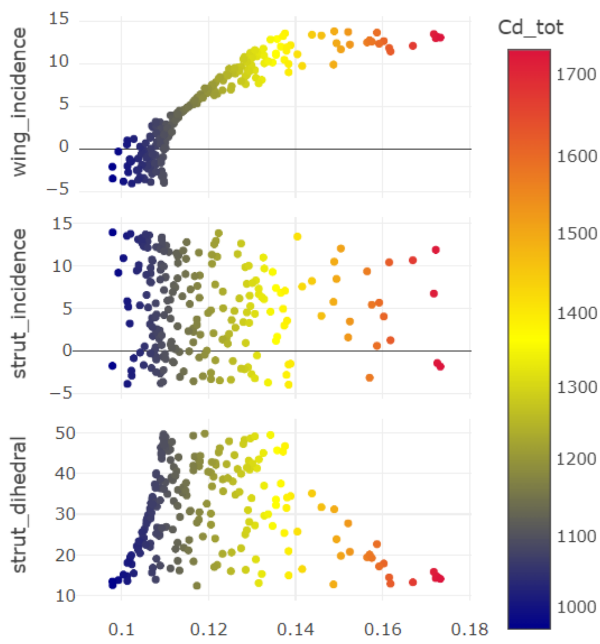

Figure 4.24: DOE for Total Drag. Values are expressed as drag counts and degrees

Figure 4.24 illustrates that the minimum total drag is achieved within the dihedral angle range of 10 to 20 degrees for the strut, accompanied by a wing local geometrical incidence ranging from 0 to -5 degrees. Notably, the incidence of the strut does not present itself as a decisive parameter in this study, as the minimum total drag can be attained regardless of the specific value within the examined range.

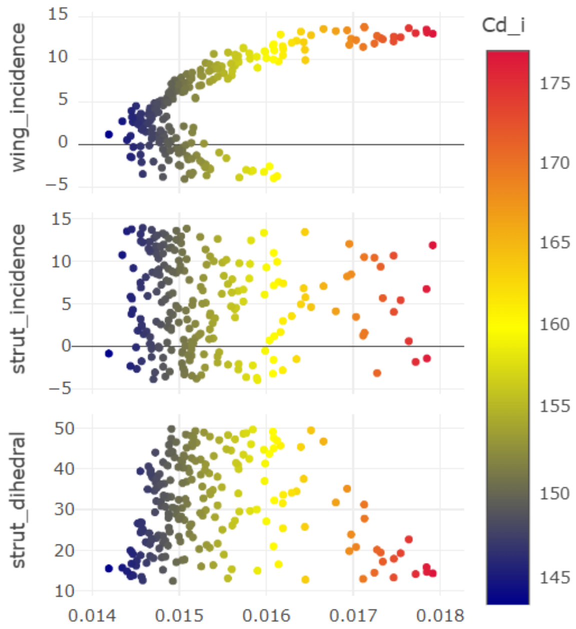

Figure 4.25: DOE for Induced Drag. Values are expressed as drag counts and degrees

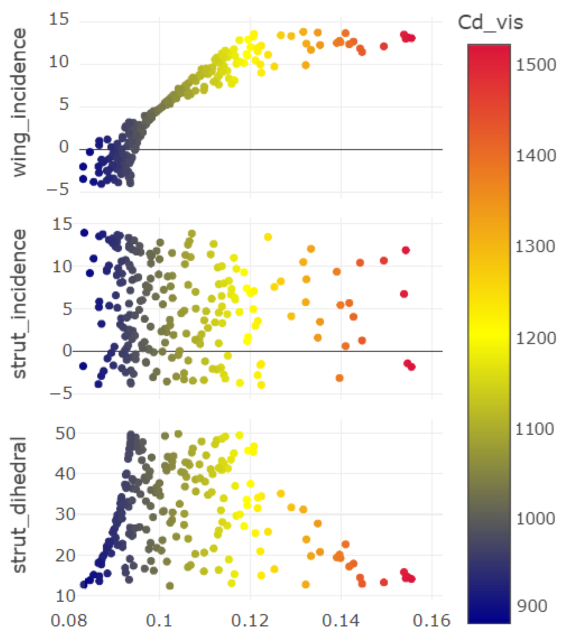

Figure 4.26: DOE for Viscous Drag. Values are expressed as drag counts and degrees

In Figure 4.25, it can be observed that minimum induced drag is obtained when the dihedral angle for the strut is between 10 and 20 degrees and wing local geometrical incidence is between 2 and 5. On the other hand, strut local geometrical incidence is not a conclusive parameter in this study as minimum total induced drag could be obtained in any strut local geometrical incidence within the considered range.

As depicted in Figure 4.26, the outcomes of the viscous drag investigation exhibit a similar pattern to the total drag results presented in Figure 4.24. This correlation can be attributed to the relatively greater influence of the viscous drag component compared to the substantially lower contribution of induced drag.

4.8 Design of Experiments (DOE) - Bezier curve

In a similar way as shown in section 4.7.1, a study based on the Latin Hypercube Sampling (LHS) method was employed as part of a rigorous Design of Experiments (DOE) methodology. The Design of Experiments (DOE) study included two experiments. The first experiment focused on varying the Bezier curve control points for the strut while measuring the total drag in drag counts, the wing local geometrical incidence was kept constant and equal to 0 degrees for all the wing sections. The set-up for the LHS array for this experiment was; 230 samples, centered values in the Stratas, the range for the strut local geometrical incidence [-5,5] in degrees, the range for the strut Bezier parametric coordinate for 'y' axis [0,1], and the strut Bezier parametric coordinate for 'incidence' axis [0,1]. The second experiment involved adjusting the Bezier curve control points for the wing, with the local geometrical incidence of the root fixed at 0 degrees, and measuring the total drag in drag counts, the strut local geometrical incidence was kept constant for all the strut sections, with a value of 0 degrees. The set-up for the LHS array for this experiment was; 230 samples, centered values in the Stratas, the range for the wing tip local geometrical incidence [-5,5] in degrees, the range for the wing Bezier parametric coordinate for 'y' axis [0,1], and the wing Bezier parametric coordinate for 'incidence' axis [0,1].

The visualisation of the span-wise distribution of local geometrical incidence with some example control points is given in Figure 4.27.

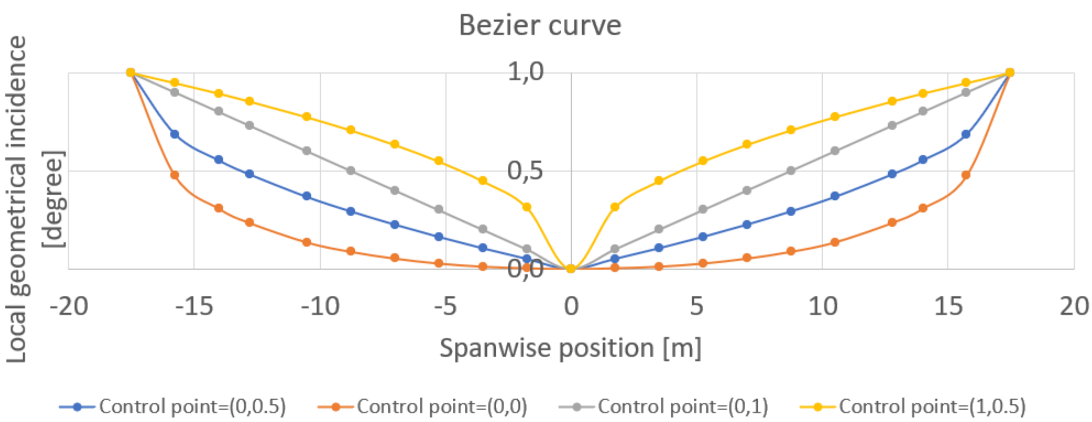

Figure 4.27: Bezier curve for different control points

These investigations were conducted using a tapered wing with specific dimensions, including a span of 32.3 m, a root chord of 3.193 m, a taper ratio of 0.469, and a reference area of 75.77 m^2. The target lift coefficient (C_L) for the simulations was set to 0.8. Furthermore, as part of the evaluation strategy, the lift contribution of the fairing was excluded from the total forces analysis. The results of the DOE study are presented in Figures 4.28 and 4.29. These figures provide valuable insights into the relationship between the Bezier curve control points and the total drag of the wing and strut configurations under investigation.

Figure 4.28 showcases the outcomes of the Design of Experiments (DOE) conducted to investigate the impact of variations in the parameters 'strut_bezier _coordinate_inc', 'strut_bezier _coordinate_y', and 'strut_incidence' on the total drag and local geometrical incidence. The objective was to identify parameter combinations that yield optimal performance for the strut design. The results reveal interesting trends in the total drag and local geometrical incidence at the section where the strut and fairing join. While there is no conclusive evidence for the total drag with variations in 'strut_bezier _coordinate_inc' and 'strut_bezier _coordinate_y', a more noticeable relationship is observed with the local geometrical incidence ('strut_incidence').

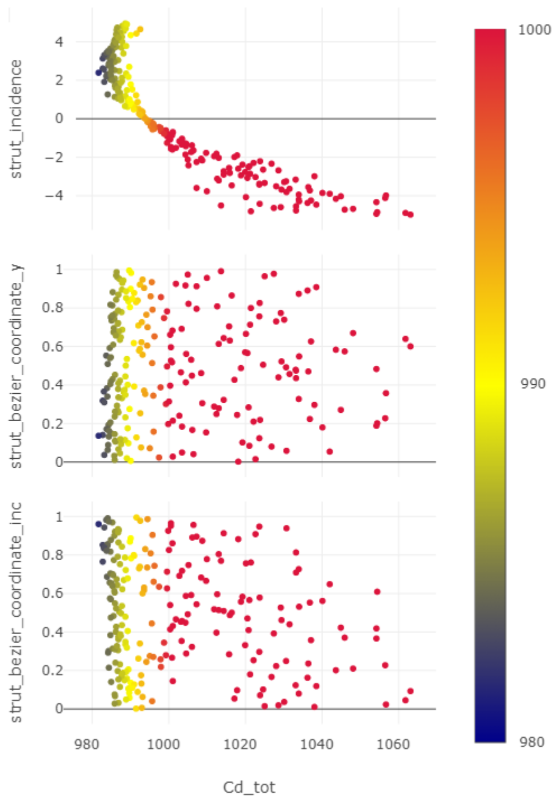

Figure 4.28: DOE for control points of Bezier curve for the strut. Values are expressed as drag counts

Notably, the total drag is minimized when specific parameter ranges are satisfied. The normalized position of 'strut_bezier _coordinate_inc' should be close to 1.

Similarly, the normalized position of 'strut_bezier _coordinate_y' should fall within the range of 0 to 0.5. Furthermore, the local geometrical incidence at the section where the strut and fairing join ('strut_incidence') should range between 1 and 3 degrees. By adhering to these parameter ranges, the strut design achieves the lowest total drag, signifying an optimized configuration. These findings offer valuable insights for enhancing the aerodynamic performance of the strut and guide the design process towards more efficient and effective solutions.

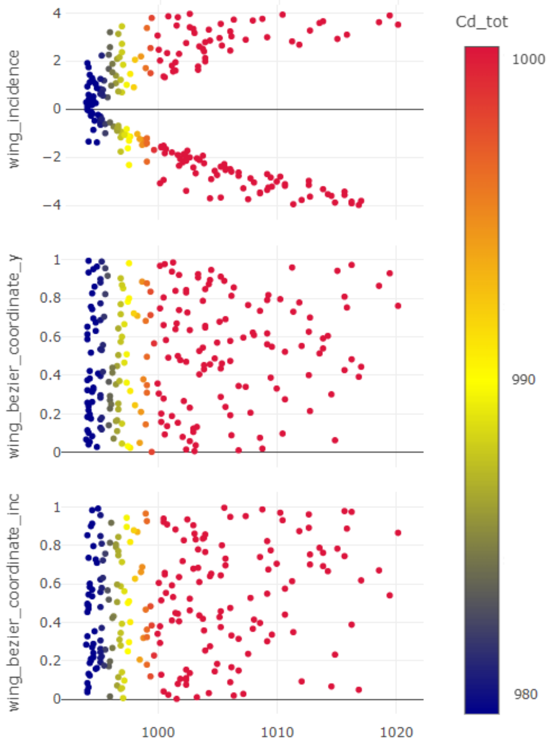

Figure 4.29: DOE for control points of Bezier curve for the wing. Values are expressed as drag counts, degrees for the incidence and unit-less for the coordinates

Figure 4.29 presents the outcomes obtained from the design of experiments (DOE) carried out to investigate the impact of variations in the parameters 'wing _incidence_tip', 'wing_bezier _coordinate_y', and 'wing_bezier _coordinate_inc' on the total drag of the wing. The results indicate that these parameters do not exhibit a clear and consistent behaviour in terms of minimizing the total drag, as different combinations can yield the same level of drag. However, certain parameter ranges demonstrate a higher probability of achieving lower total drag values. To minimize the total drag, it has been observed that the parameter 'wing_bezier _coordinate_y' should be set between 0 and 0.6. Similarly, the parameter 'wing_bezier _coordinate_inc' should be positioned near 0. Additionally, a negative local geometrical incidence ranging between -2 and -2 degrees at the wingtip ('wing _incidence_tip') has shown potential for reducing the total drag, but this effect is only valid when the root local geometrical incidence of the wing is fixed at 0 degrees. Therefore, it can be inferred that a twist value in the range of -1 to -3 degrees may be optimal for drag reduction. While these parameter ranges suggest a tendency towards achieving lower total drag values, further analysis and optimization efforts are required to fine-tune the design and identify the most optimal parameter combinations.

4.9 Optimization Investigation for SLSQP

4.9.1 Optimizer settings investigation

Initially, an evaluation was conducted to assess the impact of the parameters 'ftol' and step size 'eps' on the termination of the optimization process. This analysis aimed to understand the influence of these variables on the convergence criteria. The objective is to evaluate their effects on total drag and the resulting normalized Bezier curve control points. The optimization is conducted with several combinations of stopping criteria and step size settings. Table 4.8 provides details of the restrictions and initial points used in the optimization process. The corresponding results are presented in Table 4.9. The results include the total drag values and the resulting normalized Bezier curve control points for each case.

The purpose of this analysis is to understand how the choice of stopping criteria and step size influences the optimization outcomes, particularly in terms of total drag and the shape of the Bezier curve. By comparing the results across different settings, insights can be gained into the sensitivity of the optimization process to these parameters.

Table 4.8: Initial conditions and restrictions

Variables	**Fixed/Free-Type** (if applicable)	**Initial point**
Wing local geometrical incidence [degree]	Free-Bezier	Tip = -1, Root = 1
Strut local geometrical incidence [degree]	Free-Bezier	-1
Span [m]	Free	32.3
Root chord [m]	Fixed	3.193
Taper Ratio	Free	0.469
Strut dihedral angle [degree]	Free	20
Wing control point for Bezier curve in spanwise axis [-]	Free	0.5
Wing control point for Bezier curve in local geometrical incidence axis [-]	Free	0.5
Strut control point for Bezier curve in spanwise axis [-]	Free	0.5
Strut control point for Bezier curve in local geometrical incidence axis [-]	Free	0.5

Table 4.9: Total drag and normalized Bezier curve control point for different Optimization settings

Case	Value (ftol, eps)	Optimized $C_{D_{tot}}$ [drag counts]	Bezier P_1 ((Wing-y, Wing-incidence), (Strut-y, Strut-incidence))
1	1e-5, -0.2	962.6	((0.99, 0.99), (0.00, 0.99))
2	1e-5, 0.2	962.6	((0.99, 0.89), (0.00, 0.99))
3	1e-10, -0.2	962.6	((0.99, 0.99), (0.00, 0.99))
4	0.1, -0.2	962.6	((0.99, 0.99), (0.00, 0.99))

The obtained results indicate that variations in the stopping criteria ($ftol$) and step size (eps) have negligible impact on the total drag and normalized Bezier curve control points. Regardless of these alterations, the resulting wing design consistently exhibits a span of 35 m, a root chord of 3.193 m, a taper ratio of 0.36, and a strut dihedral angle of 10.4 degrees in all optimization cases. These findings suggest that the optimization process is robust and demonstrates limited sensitivity to modifications in these parameters.

4.9.2 Unit and Initial point effect

4.9.2.1 Strut dihedral angle

This study aims to investigate the influence of the objective function magnitude on the optimization process. The analysis is conducted by imposing certain restrictions, as outlined in Table 4.11. Throughout the investigation, a consistent local geometrical incidence is maintained for each section of both the wing and strut, while exploring different initial conditions. The objective function, which is defined as the total drag, is approached in two distinct ways: first, by considering the absolute value, and secondly, by employing drag counts ($C_{D_{tot}} \cdot 10^4$). This enables a comparison of the effects of these different units on the optimization results. Moreover, the impact of the strut's dihedral angle is examined by considering various initial points, as depicted in Figure 4.12. The optimization process is conducted with specific settings, which are detailed in Table 4.10.

Table 4.10: Optimizer setting for Unit effect on strut dihedral angle

Variable	Value
ftol [-]	1e-5
eps [-]	-0.2

Table 4.11: Restriction table for Unit effect on strut dihedral angle investigation

Variables	**Fixed/Free-Type** (if applicable)
Wing local geometrical incidence [degree]	Fixed-Array
Strut local geometrical incidence [degree]	Fixed-Array
Span [m]	Free
Chord root [m]	Free
Taper Ratio [-]	Fixed
Strut dihedral angle [degree]	Free

Table 4.12: Objective function unit effect table

Trial	**Objective**	**Input** $[\mathbf{A_{inc}},\mathbf{B},\mathbf{c_{root}},\lambda,\gamma]$	**Optimised** $[\mathbf{A_{inc}},\mathbf{B},\mathbf{c_{root}},\lambda,\gamma]$	**Optimized Objective**
1	$C_{D_{tot}}$	0, 32.3, 3.193, 0.469, 25	0, 35, 3.193, 0.356, 49.57	0.111
2	$C_{D_{tot}}$	10 ,32.3, 3.193, 0.469, 25	10, 35, 3.193, 0.356, 10.4	0.099
3	$C_{D_{tot}}$	5, 32.3, 3.193, 0.469, 25	5, 35, 3.193, 0.356, 24.6	0.108
4	$C_{D_{tot}} \cdot 10^4$	0, 32.3, 3.193, 0.469, 25	0, 35, 3.193, 0.356, 10.4	973.8
5	$C_{D_{tot}} \cdot 10^4$	10, 32.3, 3.193, 0.469, 25	10, 35, 3.193, 0.356, 10.4	988.0
6	$C_{D_{tot}} \cdot 10^4$	5, 32.3, 3.193, 0.469, 25	5, 35, 3.193, 0.356, 10.4	979.9

Where 'A_{inc}' is the local geometrical incidence of both wing and strut for all sections, 'B' is span, c_{root} is chord root, 'λ' is the taper ratio, 'γ' is the dihedral of the strut.

In Table 4.12, it is evident that the magnitude of the objective function results directly impacts the outcome of the optimization process. As discussed in Section 4.7.1, the anticipated behaviour of the optimizer is to converge towards a dihedral angle of approximately 10 degrees.

When the objective is defined as the total drag, the optimizer may not reach a local minimum due to the small variations in total drag, as illustrated in Trial 1 or Trial 3. In such cases, the optimizer struggles to find a significantly improved solution. In contrast, when the objective function is defined in terms of drag counts, the optimizer exhibits stability and tends to converge towards a dihedral angle close to 10 degrees, which has an improved probability to be a local minimum. This suggests that the drag counts formulation provides a more favourable condition for the optimization process, resulting in a more consistent and desirable outcome.

Additionally, the effect of the initial point on the optimization results can be observed in Table 4.12. It is evident that the choice of initial point for parameters such as local geometrical incidence of the strut and wing, span, and taper ratio can lead to variations in the total drag, with a difference of 14 drag counts. This highlights the importance of carefully selecting the initial point to ensure optimal results in the optimization process.

4.9.2.2 Bezier curve

In this section, the analysis focuses on the effect of the objective function unit and initial conditions on the Bezier curve control points. Table 4.13 provides information about the restrictions and initial points considered in the study. The investigation explores the total drag, both in terms of drag count and the normalized locations of the control points. By examining these factors, the study aims to understand how different objective function units and initial conditions influence the optimization process and the resulting Bezier curve control points.

Table 4.13: Restrictions and initial points

Variables	**Fixed/Free-Type** (if applicable)	**Design 1**	**Design 2**
Wing local geometrical incidence [Degrees]	Free-Bezier	Tip=-1, Root=1	Tip=-1, Root=2
Strut local geometrical incidence [Degrees]	Free-Bezier	-1	-1
Span [m]	Free	32.3	32.3
Chord root [m]	Free	3.193	3.193
Taper Ratio [-]	Fixed	0.469	0.469
Strut dihedral angle [Degrees]	Free	20	20
Wing control point for Bezier curve in spanwise axis [-]	Free	0.5	0.45
Wing control point for Bezier curve in local geometrical incidence axis [-]	Free	0.5	0.25
Strut control point for Bezier curve in spanwise axis [-]	Free	0.5	0.8
Strut control point for Bezier curve in local geometrical incidence axis [-]	Free	0.5	0.1

The comparative analysis of the local spanwise distribution between the surface groups is meticulously illustrated in Figures 4.30 and 4.31, dedicated to the wing and strut, respectively. These figures provide a visual representation of the distinct characteristics and variations in the spanwise distribution across the surfaces under investigation.

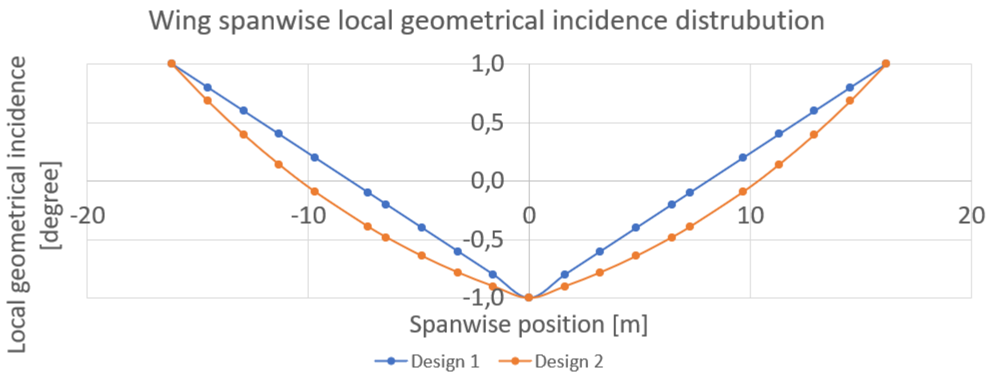

Figure 4.30: Spanwise local geometrical distribution of the wing for initial points of both designs

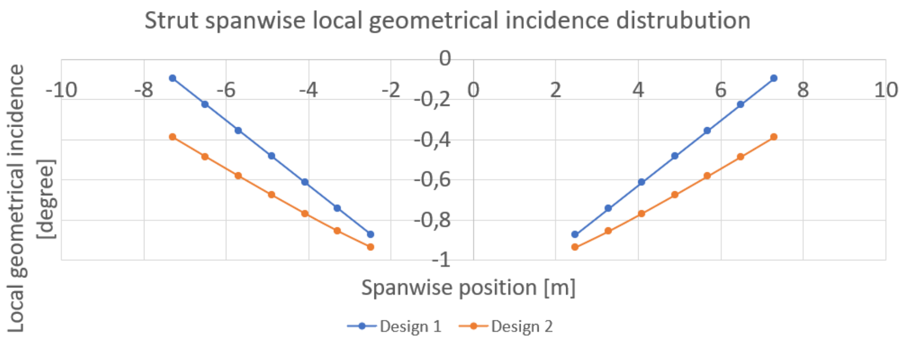

Figure 4.31: Spanwise local geometrical distribution of the strut for initial points of both designs

The results of the optimization process are given below in Table 4.14.

Table 4.14: Results of the optimization

Case #	**Objective**	**Twist**	**Optimized Objective [Drag counts]**	**Bezier P_1 ((Wing-y, Wing-incidence), (Strut-y, Strut-incidence))**
Design 1	$C_{D_{tot}} \cdot 10^4$	Positive	962.6	((0.99, 0.99), (0.00, 0.99))
Design 1	$C_{D_{tot}}$	Negative	976.1	((0.51, 0.48), (0.47, 0.53))
Design 2	$C_{D_{tot}} \cdot 10^4$	Negative	958.4	((0.98, 0.02), (0.01, 0.99))

In Table 4.14, it is evident that the optimization objective unit and initial point have a strong correlation with the Bezier curve points and the twist values. The choice of the optimization objective unit and the initial point significantly influence the resulting configuration of the Bezier curve and the associated twist distribution. Therefore, the selection of the optimization objective unit and the appropriate initial point play a crucial role in determining the final configuration of the Bezier curve and the resulting twist distribution.

4.9.3 Fairing load

This investigation focuses on analyzing the effect of Fairing forces on the optimization process. The fairing group is explained in detail in Subsection 3.3.3.1. The initial conditions and restrictions for this investigation are outlined in Table 4.16. The initial conditions include the local geometrical incidence of the wing and strut, which are defined based on the Bezier curve constraint. The objective function chosen for this analysis is the total drag, measured in drag counts. The optimizer settings used for this investigation are provided in Table 4.15. By examining these factors, the study aims to understand how the inclusion of the Fairing load affects the optimization process and its impact on the overall aircraft performance.

Table 4.15: Optimizer settings

Variable	**Value**
ftol	1e-5
eps	-0.2

Table 4.16: Fairing load investigation initial conditions and restrictions

Variables	**Fixed/Free-Type** (if applicable)	**Initial point**
Wing local geometrical incidence [degree]	Free-Bezier	Tip = -1, Root = 1
Strut local geometrical incidence [degree]	Free-Bezier	-1
Span [m]	Free	32.3
Chord root [m]	Fixed	3.193
Taper Ratio [-]	Free	0.469
Strut dihedral angle [degree]	Free	20
Wing control point for Bezier curve in spanwise axis [-]	Free	0.2
Wing control point for Bezier curve in local geometrical incidence axis [-]	Free	0.2
Strut control point for Bezier curve in spanwise axis [-]	Free	0.2
Strut control point for Bezier curve in local geometrical incidence axis [-]	Free	0.2

This optimization examines the local geometrical incidence distribution and lift distribution across the span of the wing and strut. Figures 4.33, 4.34, 4.35, 4.36, and 4.32 illustrate the optimized results in terms of these distributions. Additionally, Table 4.17 presents the results of the aerodynamic coefficients obtained from the optimization. These findings provide insights into the aerodynamic performance of the aircraft, particularly regarding the variation in local geometrical incidence and lift distribution along the span. By comparing the results under different conditions and configurations, a comprehensive understanding of the aerodynamic behaviour can be gained.

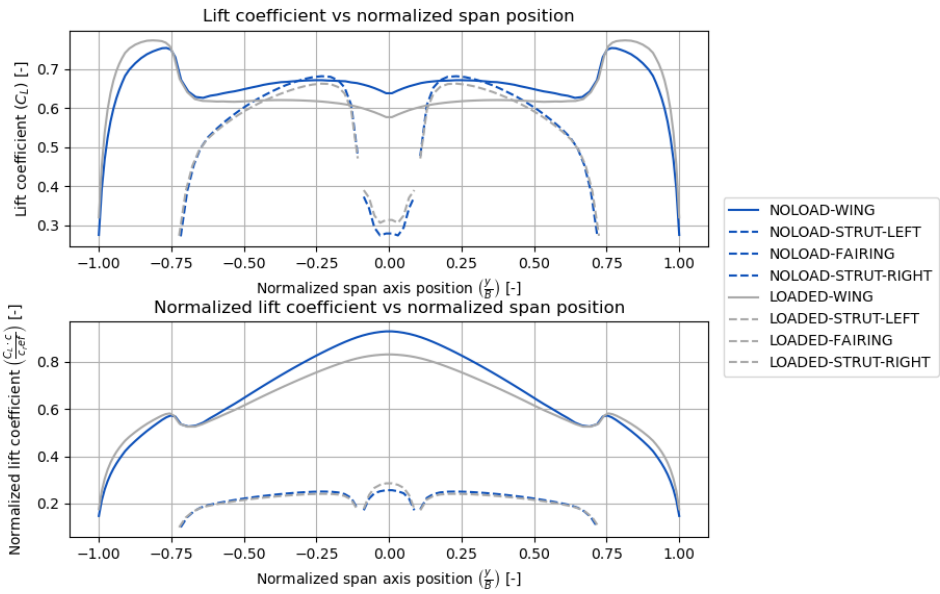

Figure 4.32: Spanwise lift distribution for loaded and unloaded cases

Where 'NOLOAD' is the case where fairing loads are calculated but not considered for meeting the C_L target of 0.8, and 'LOAD' is the case where fairing forces are counted in the total force.

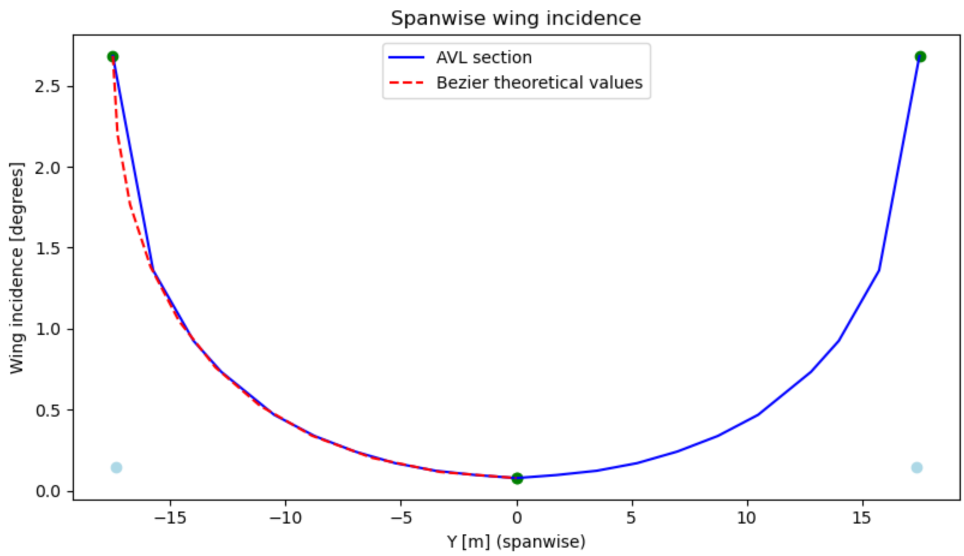

Figure 4.33: Local geometrical incidence distribution through span for wing when the fairing is counted in total drag

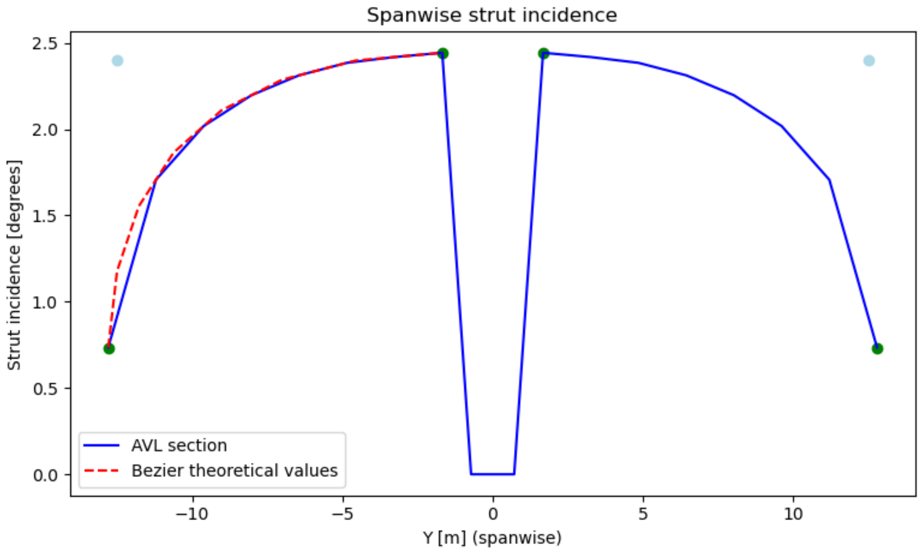

Figure 4.34: Local geometrical incidence distribution through span for strut when the fairing is counted in total drag

In Figure 4.32, it can be observed that when Fairing loads are included in the total loads, the wing tends to generate more lift near the tip due to the optimizer's attempt to achieve an elliptical lift distribution as the fairing contributes to lift near the wing root. Conversely, when Fairing loads are not considered, the wing generates more lift near the root since the fairing has no effect in that region. This effect is clearly evident in the local geometrical incidence distribution along the wing span for the two cases. When fairing forces are included, the wing exhibits a positive twist. In contrast, when fairing forces are not considered, the twist is negative. It is worth noting that the local geometrical incidence distribution of the strut remains the same in both cases.

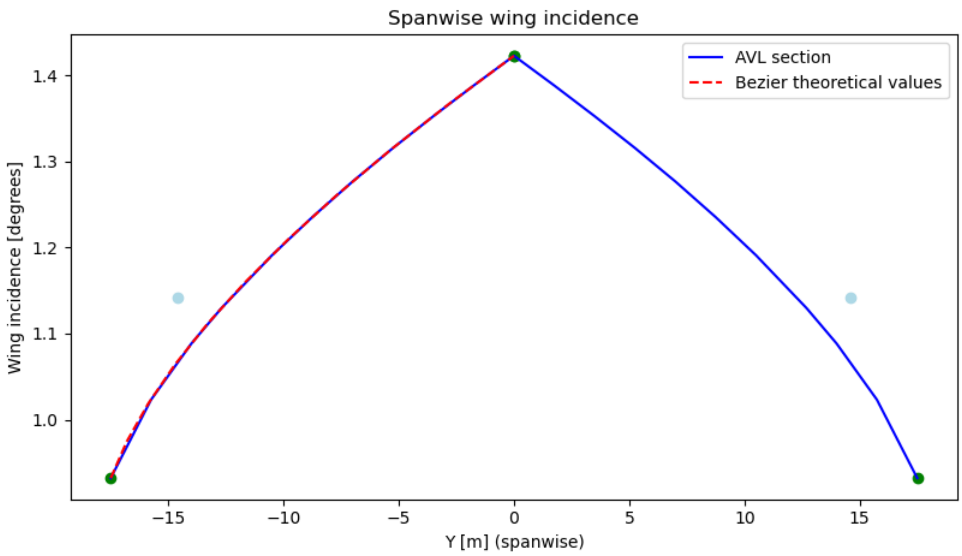

Figure 4.35: Local geometrical incidence distribution through span for wing when the fairing is not counted in total drag

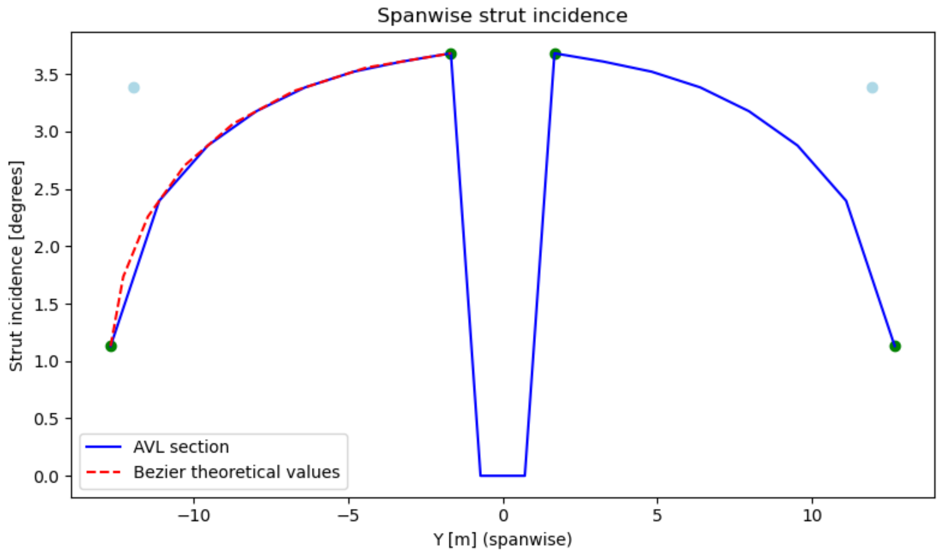

Figure 4.36: Local geometrical incidence distribution through span for strut when the fairing is not counted in total drag

Table 4.17: Aerodynamic coefficients and geometry of the cases with 'LOAD' and 'NOLOAD' conditions applied to fairing surface after optimization process

Property/Parameter	**NOLOAD**	**LOAD**	**Δ Property / Parameter** [%]
S_{ref} $[m^2]$	75.78	75.78	0.00
AoA [degree]	6.36	6.94	11.33
$C_{D_{tot}}$ [drag counts]	952.1	932.50	0.50
C_L [-]	0.80	0.80	0.00
e [-]	0.9675	0.9960	0.79
$C_{D_{ff}}$ [drag counts]	129.3	126.12	-0.73
$C_{D_{vis}}$ [drag counts]	837.6	802.60	-0.91
Wing C_L	0.663	0.640	-0.55
Wing C_{D_i} [drag counts]	63.00	73.00	19.18
Wing $C_{D_{vis}}$ [drag counts]	700.00	654.00	-1.53
Strut C_L [-]	0.137	0.136	0.59
Strut C_{D_i} [drag counts]	52.00	46.00	-8.70
Strut $C_{D_{vis}}$ [drag counts]	138.00	134.00	0.00
Span [m]	35.00	35.00	0.00
Root chord [m]	3.193	3.193	0.00
Taper Ratio [-]	0.374	0.374	0.00
Strut dihedral angle [degree]	10.4	10.5	0.95

Note: It should be noted that in the LOAD case, the sum of the wing and strut lift coefficients does not equal 0.8. This discrepancy arises due to the contribution of the fairing group, which generates lift. To facilitate a meaningful comparison, this contribution has been subtracted from the total lift coefficient.

The negative twist of the wing is necessary to prevent tip stall. The positive twist assigned by the optimizer is primarily a result of the fairing section of the wing generating more lift than it would in reality, as it is assigned a NACA0012 profile. Furthermore, the aerodynamic coefficients show that the fairing has an insignificant effect, as depicted in Figure 4.17. Given that the focus of this thesis does not encompass the influence of the fairing, the Fairing loads are not considered in the total forces. This decision is based on avoiding the unrealistic impact on lift distribution and spanwise local geometrical incidence distribution on the wing, as just a portion of the fairing is considered.

4.9.4 Objective functions effect investigation

In this investigation, the focus is on evaluating the results of the optimization process for two important parameters: the Oswald efficiency factor and the total drag. The restrictions and initial conditions used in the optimization setup are provided in Table 4.18. By analyzing the optimization results, the efficiency of the design configuration can be assessed based on the achieved Oswald efficiency factor or the total drag. These parameters serve as indicators of the aerodynamic performance and overall efficiency of the aircraft design. The results of optimization is given in Table 4.19, and Figures 4.38, 4.39, 4.40, 4.41 and 4.37.

Table 4.18: Objective function investigation initial conditions and restrictions

Variables	**Fixed/Free-Type** (if applicable)	**Initial point**
Wing local geometrical incidence [degree]	Free-Bezier	Tip = -1, Root = 1
Strut local geometrical incidence [degree]	Free-Bezier	-1
Span [m]	Free	32.3
Root chord [m]	Fixed	3.193
Taper Ratio	Free	0.469
Strut dihedral angle [degree]	Free	20
Wing control point for Bezier curve in spanwise axis [-]	Free	0.2
Wing control point for Bezier curve in local geometrical incidence axis [-]	Free	0.2
Strut control point for Bezier curve in spanwise axis [-]	Free	0.2
Strut control point for Bezier curve in local geometrical incidence axis [-]	Free	0.2

Table 4.19: Objective function investigation results

Objective	**Oswald efficiency**		$\mathbf{C_{D_{tot}}}$	
Geometry	Wing	Strut	Wing	Strut
C_L [-]	0.744	0.0554	0.6626	0.137
C_{D_i} [Drag counts]	147	26	63	52
$C_{D_{vis}}$ [Drag counts]	886	34	700	138
$C_{D_{tot}}$ [Drag counts]	1092		952.1	
e [-]	1.0019		0.9675	

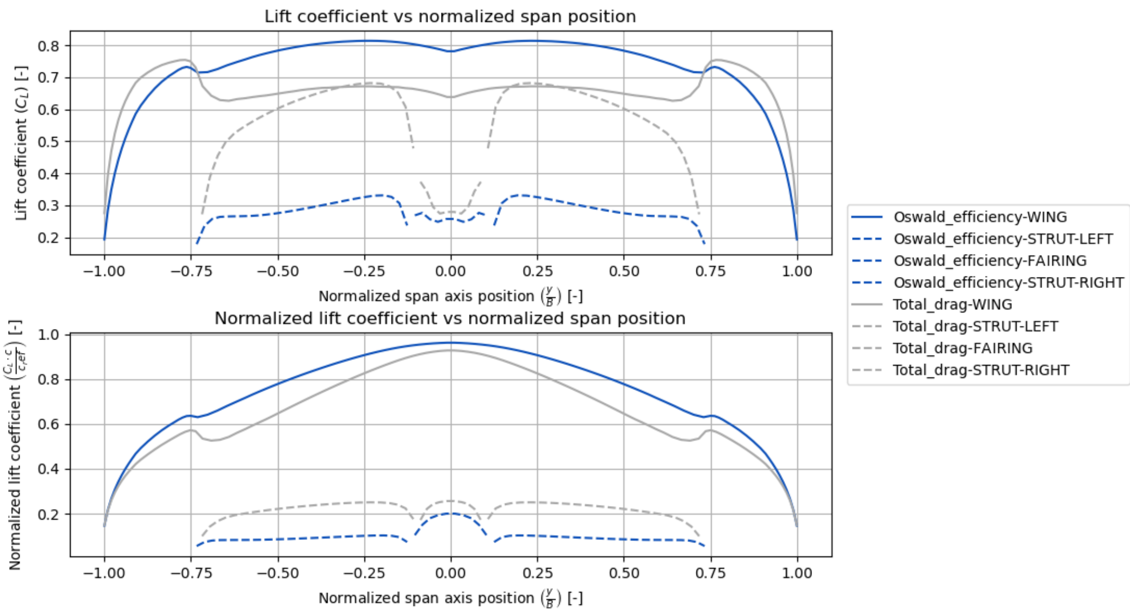

Figure 4.37: Spanwise lift distribution for both objective properties

Upon comparing Figures 4.38 and 4.40, it becomes apparent that the spanwise local geometrical incidence distribution of the wing exhibits a relatively consistent pattern across different optimization runs. This observation suggests that the optimizer strives to attain a similar lift distribution along the span of the wing. However, in Figure 4.40, it can be observed that the spanwise local geometrical incidence distribution of the strut varies between different optimizations. This is because the Oswald factor, which is a measure of the wing's efficiency, is heavily influenced by the lift distribution. The optimizer aims to achieve an elliptical lift distribution for the wing, regardless of the viscous contributions.

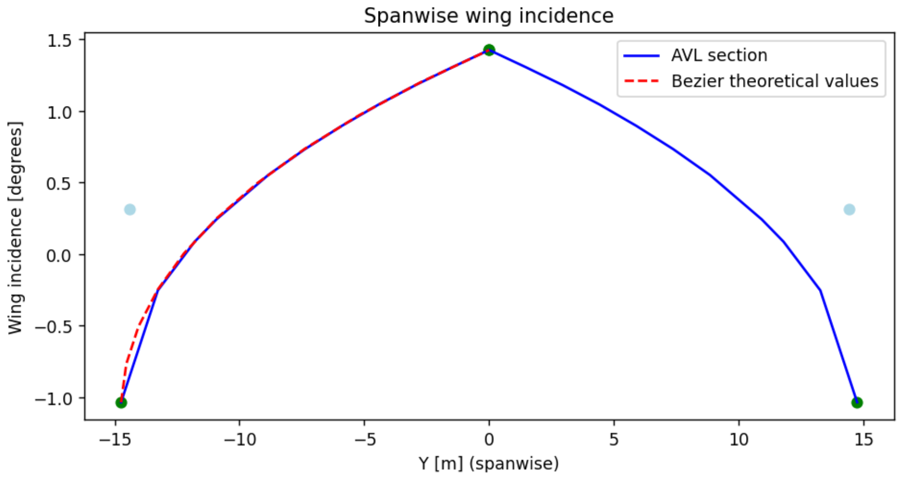

Figure 4.38: Local geometrical incidence distribution through span for wing for Oswald objective

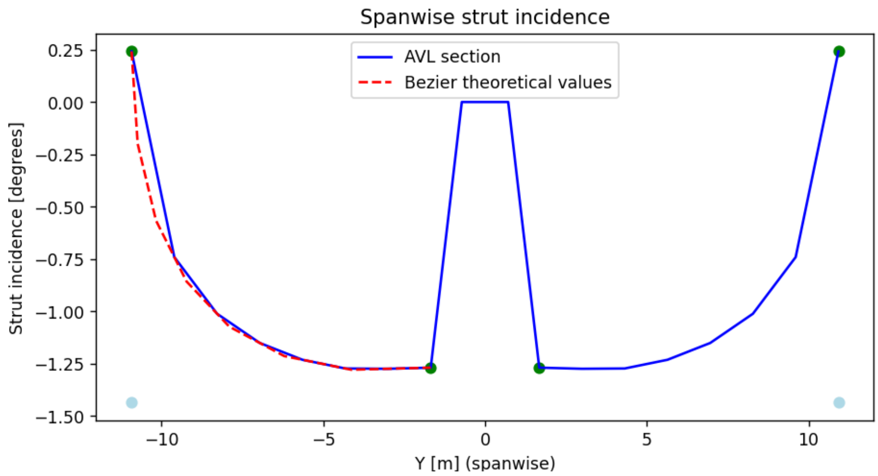

Figure 4.39: Local geometrical incidence distribution through span for strut for Oswald objective

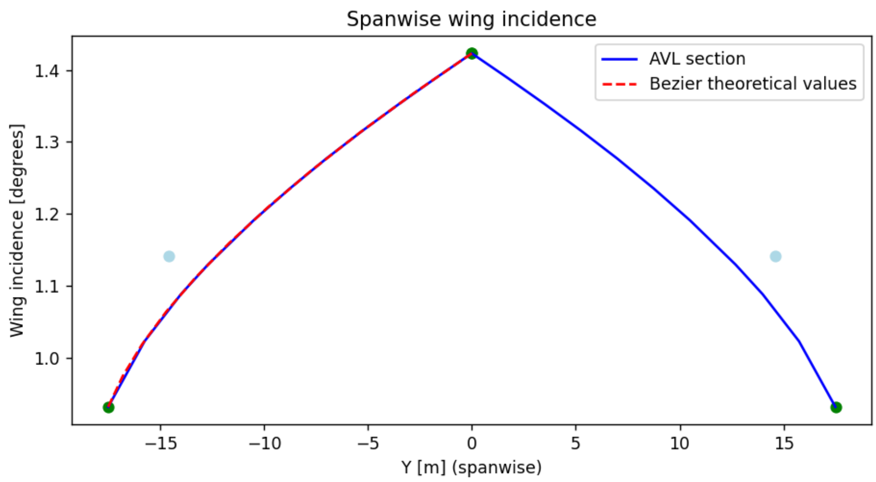

Figure 4.40: Local geometrical incidence distribution through span for wing for total drag objective

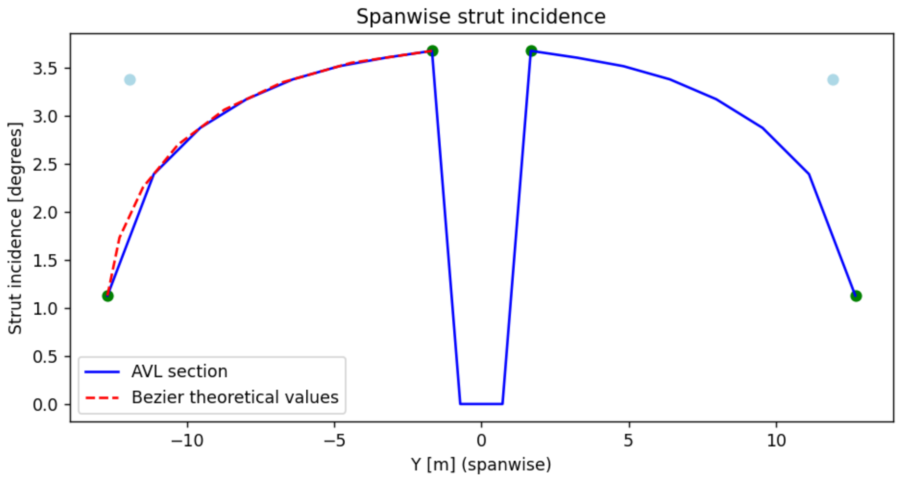

Figure 4.41: Local geometrical incidence distribution through span for strut for total drag objective

In contrast, the optimization process takes into consideration both the lift distribution and the influence of viscous drag when evaluating the total drag. To achieve the optimal total drag, the optimizer adjusts the contribution of lift for both the strut and the wing while considering the impact of viscous drag. Consequently, variations in the spanwise local geometrical incidence distribution of the strut arise as the optimizer seeks to optimize the overall drag of the aircraft by optimizing the contribution of lift for both the strut and the wing.

4.9.5 Summary and selection of design

The purpose of the design selection process is to achieve two primary objectives: minimizing total drag and optimizing the local geometrical incidence distribution of both the wing and strut. In order to assess the effectiveness of the design selection criteria, two distinct cases were examined to identify the configurations that result in the lowest total drag. For each case, specific restrictions and initial points were considered, and their details can be found in Table 4.20. The same optimizer settings, as specified in Table 4.21, were applied consistently across the cases. This approach ensures uniformity and enables meaningful comparisons between the different configurations.

Table 4.20: Restrictions and initial points

Variables	**Fixed/Free-Type** (if applicable)	**Design 1 - Initial conditions**	**Design 2 - Initial conditions**
Wing local geometrical incidence [degree]	Free-Bezier	Tip=-1, Root=1	Tip=-1, Root=1
Strut local geometrical incidence [degree]	Free-Bezier	-1	-1
Span [m]	Free	32.3	32.3
Chord root [m]	Free	3.193	3.193
Taper Ratio [-]	Fixed	0.469	0.469
Strut dihedral angle [degree]	Free	20	20
Wing control point for Bezier curve in spanwise axis [-]	Free	0.45	0.5
Wing control point for Bezier curve in local geometrical incidence axis [-]	Free	0.25	0.5
Strut control point for Bezier curve in spanwise axis [-]	Free	0.8	0.5
Strut control point for Bezier curve in local geometrical incidence axis [-]	Free	0.1	0.5

Table 4.21: Optimizer settings

Variable	**Value**
ftol	1e-5
eps	-0.2

Through an examination of the simulation results obtained for these two cases, the efficacy of the design selection criteria in attaining the desired objectives can be assessed. The total drag, as well as the local geometrical incidence distribution of the wing and strut, serve as crucial performance indicators to determine the optimal design configuration.

4.9.5.1 Design 1

The geometry of the optimized solution for Design 1 is given in Table 4.22. The aerodynamic coefficients and AoA for the initial condition, the optimized condition are given in Figure 4.23. Moreover, local geometrical incidence distribution through the span for both wing and strut is given in Figures 4.42 and 4.43.

Table 4.22: Geometric parameters for Design 1

Variable	**Initial**	**Optimized**
AR [-]	13.77	16.17
S_{ref} $[m^2]$	75.78	75.78
B [m]	32.3	35.00
C_{root} [m]	3.193	3.193
Taper Ratio [-]	0.469	0.36
Strut dihedral angle [degree]	20	10.40
Wing control point for Bezier curve in spanwise axis [-]	0.45	0.977
Wing control point for Bezier curve in incidence axis [-]	0.25	0.022
Strut control point for Bezier curve in spanwise axis [-]	0.8	0.000
Strut control point for Bezier curve in incidence axis [-]	0.1	0.995

Table 4.23: Aerodynamic coefficients for Design 1

Variable	**Initial**	**Optimized**	$\mathbf{\Delta}$**[Unit]**	$\mathbf{\Delta}$[%]
AoA [degree]	8.21	4.90	3.31	-67.63
$C_{D_{tot}}$ [drag counts]	1060.3	959.9	100.4	-10.46
C_L [-]	0.8	0.8	0.00	0.00
e [-]	0.9442	0.9685	-0.02	2.51
C_{D_i} [drag counts]	133.036	129.175	3.9	-2.99
$C_{D_{vis}}$ [drag counts]	932.1	836.4	95.7	-11.44
Wing C_L [-]	0.754	0.663	0.092	-13.85
Wing C_{D_i} [drag counts]	106	69	37	-53.62
Wing $C_{D_{vis}}$ [drag counts]	897	701	196	-27.96
Strut C_L [-]	0.046	0.137	-0.092	66.81
Strut C_{D_i} [drag counts]	22	54	-32	59.26
Strut $C_{D_{vis}}$ [drag counts]	36	136	-100	73.53

Upon analyzing Table 4.23, it becomes evident that the optimization process has had a significant impact on the design. The total drag of the strut braced wing (SBW) configuration has decreased by 10.46%, while the Oswald efficiency factor, which measures the wing's span efficiency, has increased by 2.51%. This demonstrates that the optimizer has effectively influenced the design to improve its aerodynamic performance.

An examination of the lift coefficients reveals an interesting pattern. The contribution from the wing has decreased, while the contribution from the strut has increased. This observation aligns with the discussion presented in Section 4.6, where it was highlighted that the wing's higher lift coefficient results in a relatively higher change in viscous drag, as depicted in Figure 4.22. As a result, the optimizer attempted to reduce the wing's viscous drag by lowering its lift coefficient and, conversely, increasing the strut's lift coefficient.

Specifically, the viscous drag of the wing has decreased by 11.44%, and the induced drag has decreased by 2.99%. In contrast, the strut has experienced a significant increase in both viscous drag (73.53% increase) and induced drag (59.26% increase). Despite this substantial change in the aerodynamic contribution of the strut, the absolute values indicate an overall reduction in total drag, indicating the effectiveness of the optimization process.

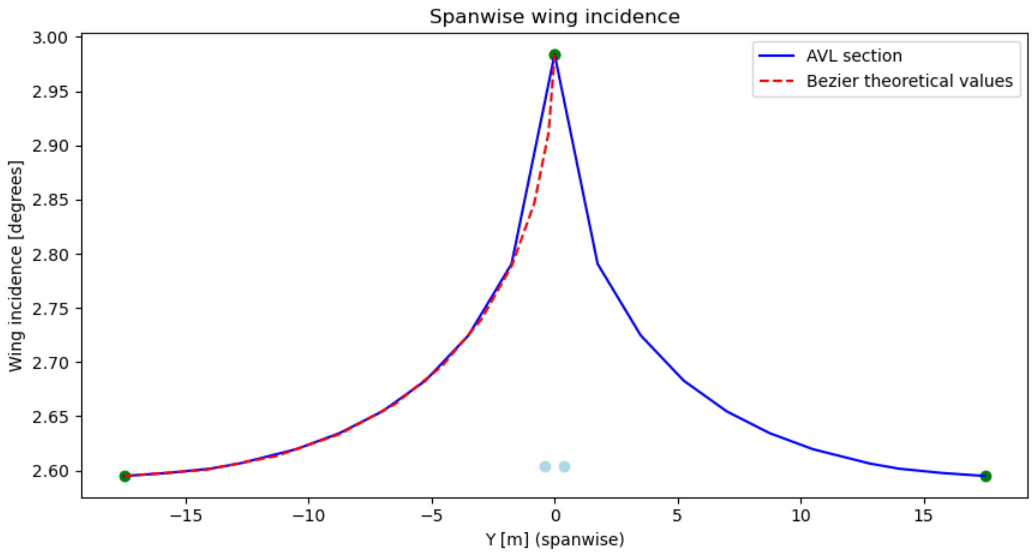

Figure 4.42: Local geometrical incidence distribution through span for wing

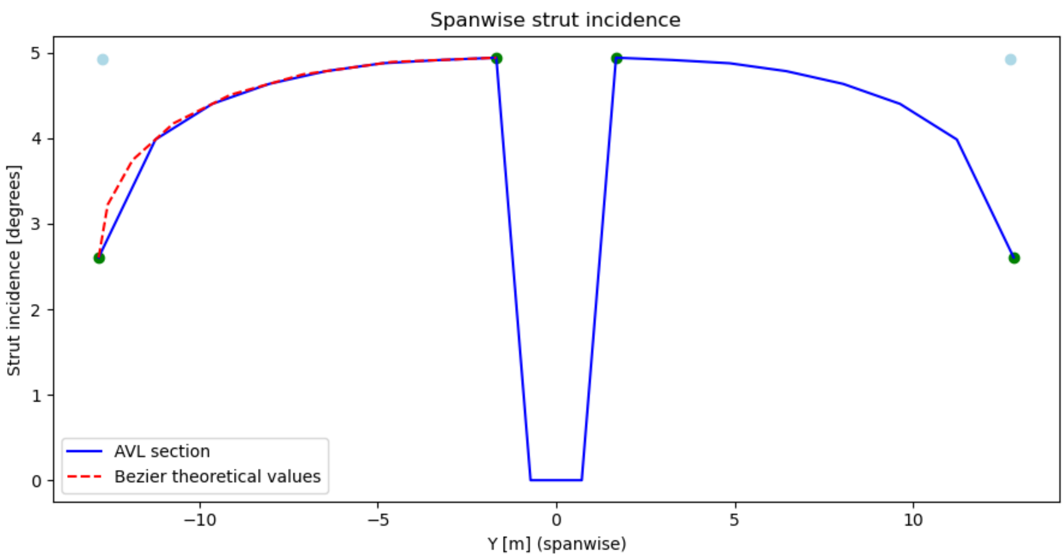

Figure 4.43: Local geometrical incidence distribution through span for strut

An examination of the geometry in Table 4.22 confirms that the optimizer has achieved the expected results in terms of increasing the Oswald efficiency factor.

The aspect ratio, span, and taper ratio of the strut braced wing (SBW) configuration have increased. Furthermore, the dihedral angle of the wing has ended up at 10.4 degrees, consistent with the discussion in Section 4.6.
In Figure 4.42 and Figure 4.43, the spanwise distribution of local geometrical incidence for wing and strut are visualized, the results are aligning with the discussion presented in Section 4.8. The smooth curve of the local geometrical incidence distribution for both the wing and strut indicates a favourable characteristic that can potentially mitigate boundary layer issues such as flow separation. The smoothness of the curve suggests a gradual transition of airflow along the span, promoting better aerodynamic performance and reducing the likelihood of flow separation. This observation highlights the effectiveness of the optimization process in achieving a desirable local geometrical incidence distribution for the wing and strut of the strut braced wing (SBW) configuration.

Overall, the findings demonstrate the optimizer's ability to significantly impact the aerodynamic characteristics of the SBW configuration, resulting in lower total drag and improved Oswald efficiency factor.

4.9.5.2 Design 2

The geometry of the optimized solution for Design 2 is given in Table 4.24. The aerodynamic coefficients and AoA for the initial condition, the optimized condition are given in Figure 4.25. Moreover, local geometrical incidence distribution through the span for both wing and strut is given in Figures 4.44 and 4.45.

Table 4.24: Geometric parameters for Design 2

Variable	Initial	Optimized
AR [-]	13.77	16.17
S_{ref} $[m^2]$	75.78	75.78
B [m]	32.3	35.00
C_{root} [m]	3.193	3.193
Taper Ratio [-]	0.469	0.36
Strut dihedral angle [degree]	20	10.40
Wing control point for Bezier curve in spanwise axis [-]	0.5	0
Wing control point for Bezier curve in incidence axis [-]	0.5	0.99
Strut control point for Bezier curve in spanwise axis [-]	0.5	0
Strut control point for Bezier curve in incidence axis [-]	0.5	1.00

The analysis of the geometry in Table 4.24 confirms that the optimizer has successfully achieved the desired results in terms of increasing the Oswald efficiency factor. The aspect ratio, span, and taper ratio of the SBW configuration have increased, contributing to improved aerodynamic performance. Additionally, the dihedral angle of the wing has reached 10.4 degrees, consistent with the discussion in Section 4.6 as in Design 1.

Table 4.25: Aerodynamic coefficients for Design 2

Variable	**Initial**	**Optimized**	**Δ[Unit]**	**Δ[%]**
AoA [degree]	8.06	4.06	4.00	-98.52
$C_{D_{tot}}$ [drag counts]	1058.7	962.9	95.8	-9.95
C_L[-]	0.8	0.8	0.00	0.00
e [-]	0.945	0.9772	-0.03	3.30
C_{D_i} [drag counts]	132.913	128.137	4.8	-3.73
$C_{D_{vis}}$ [drag counts]	930.7	842.5	88.2	-10.47
Wing C_L [-]	0.7526	0.6778	0.075	-11.04
Wing C_{D_i} [drag counts]	104	62	42	-67.74
Wing $C_{D_{vis}}$ [drag counts]	893	733	160	-21.83
Strut C_L [-]	0.1786	0.1222	0.056	-46.15
Strut C_{D_i} [drag counts]	24	48	-24	50.00
Strut $C_{D_{vis}}$ [drag counts]	38	110	-72	65.45

Upon analyzing Table 4.25, it becomes evident that the optimization process has had a significant impact on Design 2 as well. The total drag of the strut braced wing (SBW) configuration has decreased by 9.95%, while the Oswald efficiency factor has increased by 3.30%. These improvements demonstrate the effectiveness of the optimizer in enhancing the aerodynamic performance of Design 2. Similar to Design 1, the contribution from the wing has decreased, while the contribution from the strut has increased. The optimizer aimed to reduce the wing's viscous drag by lowering its lift coefficient, while increasing the strut's lift coefficient. In terms of specific drag components, the viscous drag of the wing has decreased by 21.83%, and the induced drag has decreased by 67.74%. On the other hand, the strut has experienced a notable increase in both viscous drag (65.45% increase) and induced drag (50% increase). Despite these significant changes in the aerodynamic contribution of the strut, the absolute values indicate an overall reduction in total drag, highlighting the effectiveness of the optimization process in Design 2.

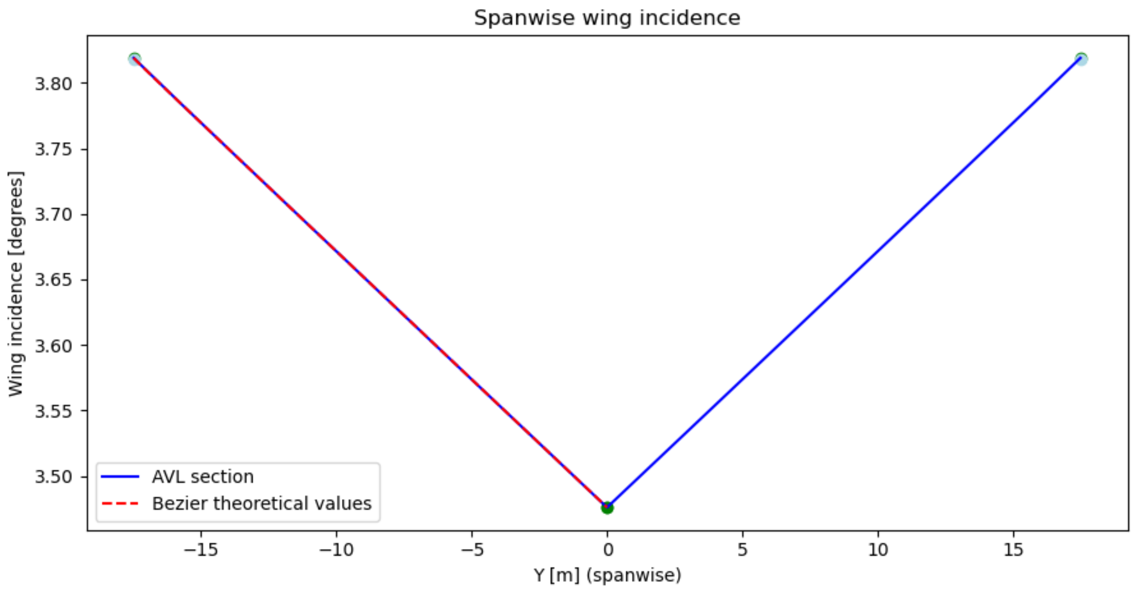

Figure 4.44: Local geometrical incidence distribution through span for the wing

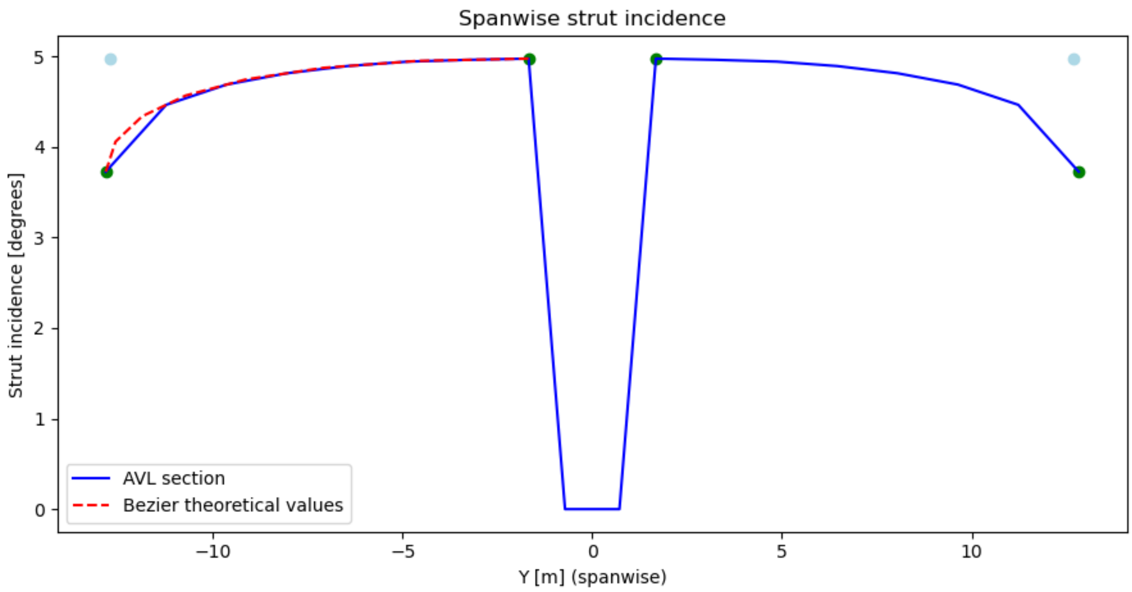

Figure 4.45: Local geometrical incidence distribution through span for the strut

In Figure 4.44 and Figure 4.45, the positions and values of the Bezier curve control points for the strut are depicted, corresponding to the discussion in Section 4.8. However, for the wing, the twist value is positive, which does not align with the discussion in Section 4.8. Moreover, this design exhibits a high risk of tip stall due to the positive twist, resulting in a higher tip local geometrical incidence compared to the root local geometrical incidence.

Overall, the findings underscore the optimizer's capability to significantly impact the aerodynamic characteristics of the SBW configuration, leading to a reduction in total drag and an enhancement in the Oswald efficiency factor, similar to Design 1. However, it is important to address the issue of tip stall associated with the positive twist in the wing design, which may require further optimization and analysis to ensure safe and efficient operation.

4.9.5.3 Comparison of obtained designs

Table 4.26 provides a comparison of the aerodynamic coefficients between Design 1 and Design 2. Design 1 and Design 2 exhibit slight differences in total drag and Oswald factor. However, the main selection criterion for choosing the optimal design is based on the local geometrical incidence distribution along the span of the wing. In Design 2, the risk of tip stall is high due to the positive twist, which can lead to aerodynamic instabilities. As a result, Design 1 is selected as the preferred design for this study. On the other hand, the local geometrical incidence distribution along the span of the strut remains consistent between Design 1 and Design 2. This indicates that the optimizer was able to identify and maintain a consistent trend for the strut under different conditions. However, the behaviour of the wing's Bezier curve in relation to total drag is more scattered as discussed in Section 4.8, which can lead to the optimizer converging to local minimums rather than finding the global optimum.

Table 4.26: Aerodynamic coefficients for Design 1 and Design 2

Variable	**Design 1**	**Design 2**	**Δ[Unit]**	**Δ[%]**
AoA [degree]	4.90	4.06	0.84	17.11
$C_{D_{tot}}$ [drag counts]	959.90	962.90	-3.0	-0.31
C_L[-]	0.80	0.80	0.00	0.00
e [-]	0.97	0.98	-0.01	-0.90
C_{D_i} [drag counts]	129.18	128.14	1.0	0.80
$C_{D_{vis}}$ [drag counts]	836.40	842.50	-6.1	-0.73
Wing C_L [-]	0.66	0.68	-0.015	-2.29
Wing C_{D_i} [drag counts]	69.00	62.00	7	10.14
Wing $C_{D_{vis}}$ [drag counts]	701.00	733.00	-32	4.56
Strut C_L [-]	0.14	0.12	0.015	11.06
Strut C_{D_i} [drag counts]	54.00	48.00	6	11.11
Strut $C_{D_{vis}}$ [drag counts]	136.00	110.00	26	19.12

Figure 4.46 illustrates the lift distribution for both Design 1 and Design 2. It can be observed that Design 2 showcases a more homogeneous lift distribution, resulting in reduced induced drag for both the wing and the integrated wing and strut system. Nevertheless, Design 1 exhibits a competitive edge as it achieves a higher contribution of lift coefficient (C_L) from the strut, thus the viscous drag for this design results be significantly lower for its wing and the integrated wing and strut system.

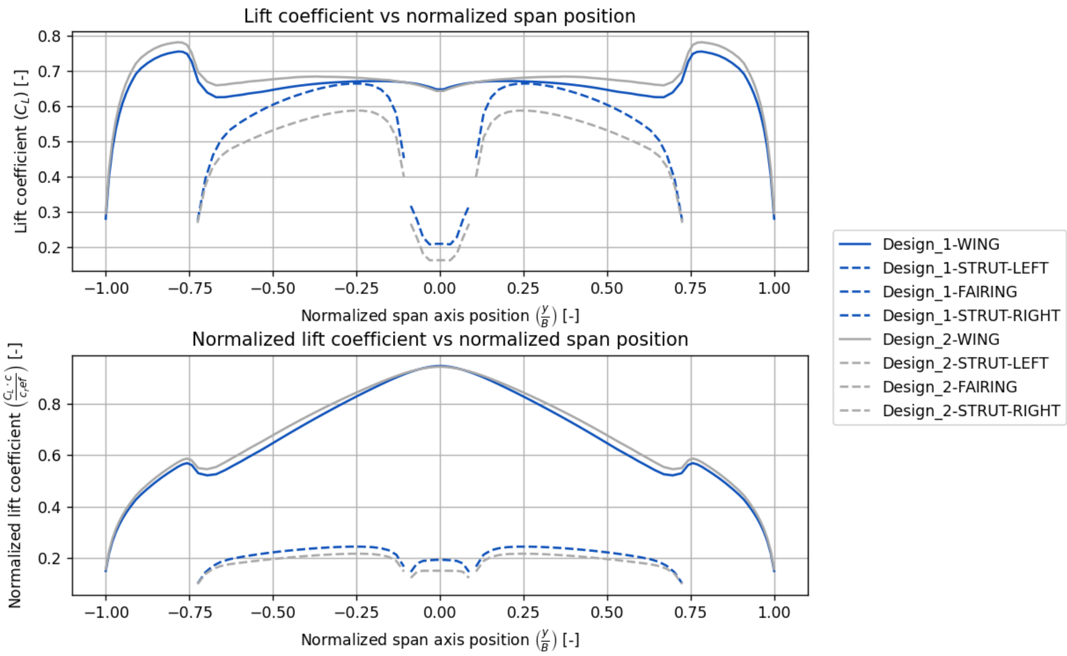

Figure 4.46: Spanwise lift distribution for both SLSQP designs

Furthermore, a study using the LHS method is done for total drag - Bezier curve relation with optimized geometry of Design 1 with 35 m Span, 3.193 m Chord root, 0.36 m taper ratio and 10.4 degree dihedral. The result of the DOE is given in Figure 4.47

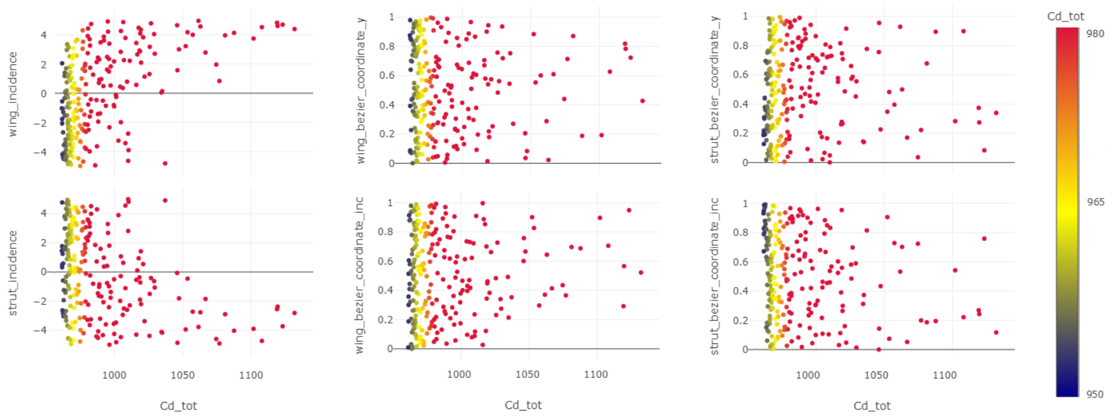

Figure 4.47: DOE for optimized wing. Values in drag counts for drag coefficients, degrees for incidence and unit-less for coordinates

In the DOE study for the optimized wing, it is observed that the lowest total drag achieved is 961 drag counts. This value is higher than the total drag obtained through the optimization process for Design 1, indicating that the optimization has had a significant and positive impact. The fact that the optimization process was able to further reduce the total drag beyond the initial DOE study demonstrates its effectiveness in improving the aerodynamic performance of the wing. This outcome confirms that the optimization process has been successful in achieving the objective of minimizing total drag.

Furthermore, it is worth noting that there are families of potential designs that should be considered, as they yield a drag count of 961. However, it is essential to also take into account other factors, such as tip stall, during this phase of the design process.

4.10 Optimization Investigation for GA

In this section, a concise discussion of the GA optimization strategy will be presented. As explained in Subsection 3.5.5.1, a well-defined penalty function was incorporated into the GA optimization scheme to ensure strict adherence to the prescribed area constraint for the wing. While this approach proved effective in maintaining the integrity of the area definition, it also incurred a substantial increase in computational cost, rendering the GA less efficient. Moreover, the solution attained through the GA approach deviated significantly from the optimal solution achieved by the SLSQP method, as outlined in Section 4.9.5.

Based on the points discussed earlier, the geometric parameters of the wing were determined and held constant throughout multiple iterations of the optimization process. The specific geometric values employed for the GA optimization procedure are outlined in detail in Table 4.27. Furthermore, the configuration settings for the GA, including relevant parameters and constraints, are provided in Table 4.28. Similarly to the approach followed in the SLSQP section, the contribution of Fairing loads was disregarded in this analysis.

Table 4.27: GA analysis fixed variables and values

Variables	**Fixed/Free-Type** (if applicable)	**Initial point**
Span [m]	Fixed	35
Root chord [m]	Fixed	3.193
Taper Ratio [-]	Fixed	0.36

Table 4.28: GA optimizer settings

Variable name	**Value**
Number of generations	40
Population number	40
Mutation probability	0.025
Crossover probability	0.95
Mating pool individuals	2
Evolution type	Binary
Binary string size	30

In Table 4.28, the "number of generations", "population size", and "mating pool individuals" are variables that can significantly influence the convergence to the global minimum in the optimization process. Higher values for these variables generally increase the likelihood of converging to the global minimum. However, it is important to note that increasing these numbers also results in higher computational costs. Therefore, there exists a trade-off between computational power and the convergence probability to the global minimum. It is necessary to carefully select these variables based on available resources and the desired level of optimization within the given constraints.

4.11 Comparison between GA and SLSQP

In this section, both GA and SLSQP algorithms are compared. The Design 1 design from Section 4.9.5 is used for SLSQP results and the GA settings are discussed in Section 4.10. The results of both GA and SLSQP in terms of aerodynamic coefficients are given in Table 4.29.

Table 4.29: Aerodynamic coefficient results for GA and SLSQP

Variable	**GA**	**SLSQP**	**Δ[Unit]**	**Δ**[%]
AoA [degree]	10.55	4.9	5.65	-115.31
$C_{D_{tot}}$ [drag counts]	962.1	959.9	2.2	-0.23
C_L [-]	0.8	0.8	0.00	0.00
e [-]	0.9946	0.9685	0.03	-2.69
C_{D_i} [drag counts]	836.5	836.4	0.1	-0.01
$C_{D_{vis}}$ [drag counts]	125.841	129.175	-3.3	2.58
Wing C_L [-]	0.6583	0.6626	-0.004	0.65
Wing C_{D_i} [drag counts]	83	72	11	-15.28
Wing $C_{D_{vis}}$ [drag counts]	693	701	-8	1.14
Strut C_L [-]	0.1416	0.1374	0.004	-3.06
Strut C_{D_i} [drag counts]	42	54	-12	22.22
Strut $C_{D_{vis}}$ [drag counts]	144	136	8	-5.88

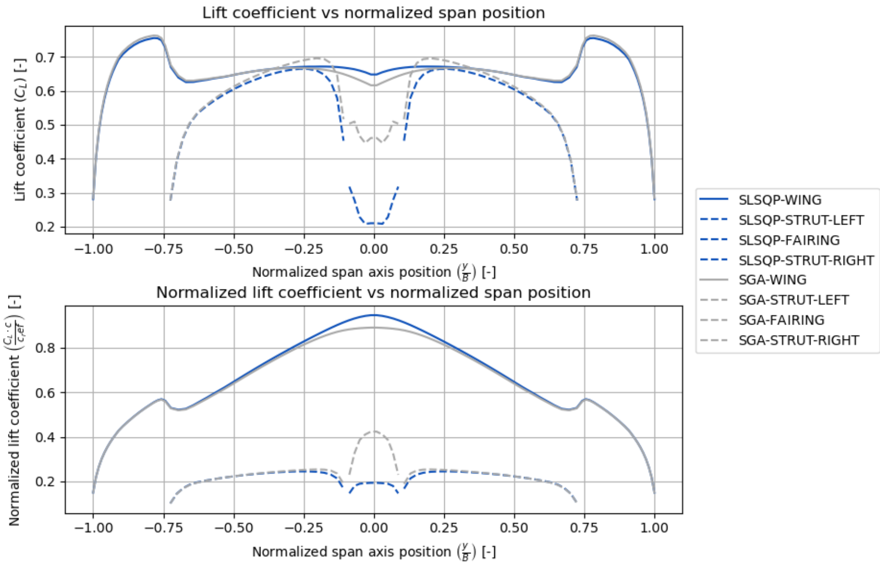

Figure 4.48: SLSQP vs. GA Lift distubution

In Table 4.29, it is evident that the SLSQP algorithm yields slightly better results than the GA algorithm in terms of total drag. The primary source of this difference can be attributed to the induced drag component, as the total viscous drag remains nearly the same between the two algorithms. However, it is noteworthy that the contributions to viscous drag exhibit variations in response to the optimization algorithms. Specifically, the span-wise lift distribution differs between the two algorithms. In the GA solution, less lift is generated near the root of the wing, while slightly more lift is generated near the strut joint, resembling a more distributed lift distribution. As a result, the Oswald factor is 2.76% higher in the GA solution compared to SLSQP. The spanwise lift distribution is given in Figure 4.48.

Furthermore, upon examining the relationship between lift and induced drag for both optimization algorithms, it is apparent that the GA solution generates more drag for nearly the same amount of lift. This indicates that the Oswald efficiency of the wing is inferior in the GA solution. Conversely, it is observed that the strut generates more lift with less induced drag in the GA solution, suggesting that the strut exhibits better Oswald efficiency in the GA solution.

In summary, the SLSQP algorithm exhibits superior performance in terms of minimizing total drag compared to the GA. Conversely, the GA demonstrates higher efficiency in terms of total Oswald efficiency. It is important to note, however, that the GA may necessitate a larger population size and more generations to converge to the optimal solution due to the random initialization of individuals in the first generation. In contrast, the SLSQP algorithm is capable of finding a satisfactory solution with relatively lower computational costs, especially when an appropriate initial point and objective unit are employed. Furthermore, it is crucial to conduct trial and error investigations to determine the suitable initial point and objective unit for the SLSQP algorithm, as these variables are not known in advance. In this context, employing a GA algorithm can provide computational advantages by reducing costs.

4.12 Weight estimation

In this section, a weight estimation is performed specifically for Design 1 of SLSQP, which has been discussed in Section 4.9.5. The weight estimation of the cantilever wing is initially carried out using Raymer's Equation, as presented in Equation 3.12. The specific values employed for the weight estimation of the cantilever wing are provided in Table 4.30. Furthermore, these same values from Table 4.30 are utilized in the weight estimation formula for the strut-braced wing of the Cessna, as described by Equation 3.11.

Table 4.30: Parameters used for Semi-empirical formulas

Parameter	**Value wing**	**Unit**
n_z $(1.5 \cdot Limit\,load\,factor)$	5	-
W_0 (MTOW)	47040	lbf
S_W (Wing reference area)	815.69	ft^2
AR	16.17	-
Sweep angle	0	degree
q_∞ (Dynamic Pressure)	74.2	lbf/ft^2
λ (Taper ratio)	0.359	-
t/c (thickness/chord)	0.12	-

The results obtained from Raymer's semi-empirical formula for the weight estimation of the cantilever wing and Cessna's strut-braced wing formula are presented in Table 4.31. The comparison and analysis of these weight estimation methodologies are discussed in detail in Section 4.12.5.

Table 4.31: Semi-empirical formula results for cantilever and strut-braced wing

Formula	$\mathbf{W_W}$ **[lbf]**	$\mathbf{W_W}$ **[N]**
Cessna-strut-braced	7032.93	31284.03
Raymer	6106.82	27164.49

4.12.1 Bending Moment Results

The values for the variables that were used for Bending Moment calculation are given in Table 4.32 and in Section 3.6.4 for the motor weight and spanwise location.

Table 4.32: Variables used for weight and bending moment calculation

Variable	Value	Unit
ρ_∞ (Density)	0.7708	m^3/kg
h (Altitude)	4572	m
M_∞	0.3	-
q_∞ (Dynamic Pressure)	3553.00	Pa
Cantilever wing mass	2770.00	kg
$W_W/2$ (Half of the wing Weight)	13586.88	N
Weight of the Region 1	973.78	N
Weight of the Region 2	12613.09	N
Position of Weight of the Region 1	-7.39	m
Position of Weight of the Region 2	-5.17	m

Where 'Region 1' and 'Region 2' are the Bending Moment regions discussed in Section 3.6.2.

Table 4.33: Bending moment contributions for Region 1

BMX contribution	**Force [N]**	**BMX (+G condition) [N.m]**	**BMX (-G condition) with Ultimate Loading Factor [N.m]**
Lift	20000.06	37740.70	-56611.05
Weight of the wing	-973.78	13999.78	-20999.67
Weight of motors	0.00	0.00	0.00
Total	**19026.28**	**51740.48**	**-77610.72**

Where BMX is the Bending Moment.

Table 4.34: Bending moment contributions for Region 2

BMX contribution	**Force [N]**	**BMX (+G) [N.m]**	BMX ($\mathbf{n_z = -1}$) **with Ultimate Loading Factor [N.m]**
Lift	81216.97	59894.67	-89842.01
Weight of the wing	-12613.10	77870.14	-116805.21
Weight of the motors	2842.00	-14948.92	22423.38
BMX of Region 1	-	51740.48	-77610.72
Shear force of Region 1	19026.28	78388.27	-117582.41
Total	-	252944.65	-379416.97

Where BMX is the Bending Moment.

4.12.2 Wing weight results

The change between the regions discussed in Section 3.6.2 can be seen in Table 4.35. Therefore, using equation 4.1 the wing weight for a SBW is calculated as 1540.12 kg.

$$W_{wing} = (1 - \boldsymbol{\Delta}_{area}) * W_{W_{Raymer}} \tag{4.1}$$

Table 4.35: BMX for each considered region

Element	Value
Wing and strut joint point [m]	12.82
Area under cantilever wing graph $[N \cdot m^2]$	1410417.80
Area under SBW graph $[N \cdot m^2]$	784256.31
$\boldsymbol{\Delta}_{area}$ [%]	44.40
Wing Weight with applied decrease [kg]	1540.12

4.12.3 Strut weight results

In the calculation of the strut weight, Young's modulus of aluminium alloy Al 7075 is assumed to be 69 GPa. The reaction force on the strut is determined to be -29607 N by dividing the bending moment on the bone by the distance in the "-G" condition. The critical force (P_{cr}) is calculated as -246018 N by dividing the sine of the dihedral of the strut and multiplying it by the safety factor (1.5). The inertia based on buckling criteria is found to be 50130940 mm^4. The assumed beam geometry for the strut and the calculated weight of the strut, including a factor for secondary structures such as brackets, fittings, leading edge, trailing edges, and manufacturing tolerances, are provided in Table 4.36.

Table 4.36: Geometric and material variables of the strut

Geometry	Value	Unit
Length of strut	11780	mm
S (outer surface length of beam)	300	mm
s (inner surface length of beam)	298	mm
t (Thickness of beam)	2.87	mm
I Inertia from geometry	50130940	mm^4
I Inertia from Buckling formula	50130940	mm^4
ρ_{Al} (Aluminum density)	2850	kg/m^3
Factor for secondary structures	1.4	-
Weight of one strut	160.11	kg

4.12.4 Total weight results

Cantilever wing weight, wing weight of SBW and the weight of the strut are summarized in Table 4.37.

Table 4.37: Total weight of cantilever and strut braced wing configuration

Element	Value
$W_{cantilever}$ [kg]	2770.01
W_{wing} [kg]	1540.12
W_{strut} [kg]	320.22
$W_{wing+strut}$ [kg]	1860.34
$\mathbf{\Delta_{weight}}$ [%]	**32.83**

The estimation of the weight of the strut braced wing (SBW) shows a potential decrease of 32.83% compared to the cantilever wing design. This reduction in weight highlights the advantage of optimizing the SBW configuration for total drag, as it also leads to improvements in weight estimation. It is worth noting that employing more Bending Moment Regions in the methodology could enhance the reliability of the results, as the linear approximation used for the two regions may overestimate the decrease in wing weight. However, despite this uncertainty, the SBW design still demonstrates a weight advantage over the cantilever wing design.

4.12.5 Methodology comparison

Cessna‘s strut-braced wing formula and the implemented bending moment and simplified strut methodology are compared in the 4.38.

Table 4.38: Weight methodology comparison Table

Method	Value
$W_{wing+strut}$ BMX [kg]	1860.34
$W_{wing+strut}$ Cessna SBW [kg]	3190.08
$\mathbf{\Delta_{weight}}$ [%]	**41.68**

A significant difference of 41.68% is observed between the weight estimation methodologies. This discrepancy can be attributed to various factors. Firstly, it should be noted that Cessna's strut-braced wing formula used in the weight estimation is based on semi-empirical principles and may have limitations in its applicability to different wing designs not considered in its database. Therefore, the accuracy of the formula for estimating the weight of the strut-braced wing configuration might be compromised. Additionally, the assumptions made in the bending moment and simplified strut methodologies, which are used to estimate weight reduction, may not fully capture the intricate interactions and structural behaviour of the wing and strut. Consequently, these assumptions could introduce deviations in the weight estimation results. It is evident that further research and validation are necessary to refine and enhance the accuracy of the weight estimation methodologies specifically tailored for the strut-braced wing configuration.

5

Conclusion

The achievement of minimizing the aerodynamic effects of the strut during the conceptual design phase is a notable accomplishment. The method employed in this study has proven to be stable, computationally efficient, and capable of providing reasonably accurate solutions for conceptual design and optimization purposes. However, it is important to acknowledge that the assumptions employed in the method may not fully capture the intricate details of the flow. Therefore, it is crucial to validate and fine-tune the results obtained from the final output using higher-fidelity techniques to ensure improved accuracy and reliability.

Nonetheless, the findings from this study provide valuable insights into the interplay and inter-dependencies between the wing and strut, contributing to a deeper understanding of their aerodynamic characteristics and optimization using GA and SLSQP. At the culmination of this research, a comprehensive tool has been developed that enables the creation of a strut-braced wing with a specified area and airfoil profile. The tool incorporates optimization algorithms within predefined bounds and settings to optimize the design. This tool serves as a valuable asset in the conceptual design phase, facilitating the efficient and effective optimization of strut braced wing configurations. Additionally, the weight calculation methodology highlights the potential for further improvement in optimization with weight estimation and underscores the advantages of the strut braced wing design.

5.1 Research Output

Based on the findings of this study, the following recommendations and conclusions are provided for the conceptual design of a strut braced wing, considering a wing with an area of 75.78 m^2, and NACA0012 as the airfoil profile for both wing and strut, and operating at a cruise condition with a C_L of 0.8 and a M of 0.1, within the given bounds:

- Regardless of the selected objective (e.g., total drag), the weight of the wing is observed to decrease.
- It is recommended to carefully select the unit for the objective function. In the case of selecting total drag as the objective, it is suggested to use total drag in drag counts for consistency.
- If sufficient resources and time are available, conducting a Design of Experiments (DOE) study for the local geometric incidence of the wing and strut

is suggested. This study can help clarify the appropriate initial points and bounds for optimization.

- While the Genetic Algorithm (GA) may have higher computational costs, it offers an advantage in seeking global minima compared to the SLSQP method, which can converge to local minima. However, it is important to consider both GA and SLSQP methods as they have a significant impact on the optimization process, taking into account specific requirements and constraints.
- In the case of the NACA0012 airfoil, the change in viscous drag is closely related to the lift contributions from the wing due to the highly non-linear nature of the lift coefficient and its relationship with the viscous drag coefficient in the region where wing lift coefficients exist. Conversely, the strut exhibits a relatively flat and linear relationship between its lift coefficient (CL) and viscous drag. Consequently, an increase in the lift contribution from the wing has a more pronounced effect on the overall viscous drag compared to the strut. It is worth noting that different airfoil profiles can yield different optimization outcomes. For example, if the lift-drag graph exhibits a more linear behaviour near the feasible wing lift coefficients, the impact of changes in viscous drag on the total drag may be less significant. In cases where the lift-drag graph exhibits a more linear behaviour near the feasible wing lift coefficients, reducing the lift contribution from the strut becomes crucial in achieving lower total drag. This is due to the significantly lower Oswald efficiency of the strut and the greater influence of induced drag on the total drag. By minimizing the lift contribution from the strut, the overall induced drag can be reduced, resulting in a more optimized and efficient design with lower total drag.

These recommendations provide guidelines for the conceptual design of strut braced wings, considering key parameters and their effects on aerodynamic performance and weight optimization.

5.2 Future Development

It is believed that there is room for improvement and development of this project as listed below:

- Validation and fine-tuning of the optimization results should be conducted using higher fidelity Computational Fluid Dynamics (CFD) simulations and wind tunnel testing. While the optimization process provides valuable insights and initial improvements, it is crucial to verify the results using more accurate and detailed aerodynamic data. By comparing the optimized design with high-fidelity CFD simulations and wind tunnel measurements, any discrepancies or areas for further refinement can be identified. This validation process ensures that the optimized design aligns with the expected aerodynamic performance and enhances confidence in its effectiveness.
- Weight estimation methodology can be enhanced by exploring alternative approaches, particularly for cantilever wing weight estimation with multiple sections, to more accurately calculate bending moments. Moreover, the Weight estimation methodology could be validated with Finite Element Method (FEM)

analyses for strut braced wings. Additionally, the weight estimation methodology can be integrated into the optimization process, allowing for the simultaneous consideration of weight and total drag. This objective is determined by evaluating the performance implications, taking into account the impact of weight on the range and the effect of total drag on the range. Given the significance of range as a critical limitation in battery-electric aircraft, optimizing both weight and total drag becomes crucial. By incorporating weight estimation and effectively managing the trade-off between weight and total drag, the design can be optimized to achieve the desired range performance.

- The optimization process can be extended to include the fuselage by utilizing AVL's slender-body model for fuselages. This model enables the consideration of fuselage aerodynamics in the optimization process, allowing for a more comprehensive and accurate analysis of the overall aircraft performance. By incorporating the fuselage into the optimization, the design can be further refined to achieve improved aerodynamic characteristics and enhance the overall efficiency of the aircraft.
- Researching and investigating the semi-empirical method with higher-fidelity CFD and wind tunnel data could be useful for estimating interference drag. Implementing this method into the Vortex-Lattice Method and optimization process would enhance the reliability of the results.
- Regarding the tool performance, it might be possible to enable multithreading with the OpenMP library in Python, which can considerably decrease the computational time for both optimization schemes.

Bibliography

[1] “ES-30,” Heart Aerospace. [Online]. Available: https://heartaerospace.com/es-30/. [Accessed: 14-Feb-2023].

[2] V. J. S. Barreda, “Conceptual Design Optimization of a Strut Braced Wing Aircraft ,” thesis.

[3] “Aircraft Technology Roadmap to 2050: IATA,” Docslib. [Online]. Available: https://docslib.org/doc/1789734/aircraft-technology-roadmap-to-2050-iata. [Accessed: 06-Feb-2023].

[4] “CO2 emissions from Commercial Aviation: 2013, 2018, and 2019,” International Council on Clean Transportation, 25-Jan-2022. [Online]. Available: https://theicct.org/publication/co2-emissions-from-commercial-aviation-2013-2018-and-2019/. [Accessed: 06-Feb-2023].

[5] “The change is already underway,” Go to startpage. [Online]. Available: https://www.swedavia.com/the-change-is-already-underway/. [Accessed: 06-Feb-2023].

[6] “Electric aviation - avinor,” avinor.no. [Online]. Available: https://avinor.no/en/corporate/klima/electric-aviation/electric-aviation. [Accessed: 06-Feb-2023].

[7] G. Gardner, “Polishing my crystal ball: Airline traffic in 2050,” International Council on Clean Transportation, 09-Feb-2022. [Online]. Available: https://theicct.org/global-aviation-airline-traffic-jan22/. [Accessed: 24-Feb-2023].

[8] “Nasa N+3 subsonic fixed wing silent efficient low-emissions commercial transport (SELECT) vehicle study - NASA technical reports server (NTRS),” NASA. [Online]. Available: https://ntrs.nasa.gov/citations/20100042399. [Accessed: 24-Feb-2023].

[9] F. Collier, “Concepts and technologies for Green Aviation.” [Online]. Available: https://www.nasa.gov/pdf/395949main_collier.pdf [Accessed: 07-Feb-2023].

[10] R. Duggirala, C. Roy, and J. Schetz, “Analysis of Interference Drag for Strut-Strut Interaction in Transonic Flow,” 47th AIAA Aerospace Sciences Meeting including The New Horizons Forum and Aerospace Exposition, 2009.

[11] Y. Ma, S. Karpuk, and A. Elham, “Conceptual Design and comparative study of strut-braced wing and twin-fuselage aircraft configurations with ultra-high aspect ratio wings,” AIAA AVIATION 2021 FORUM, 20

[12] G. Potter, (2017) “Conceptual Design of a Strut-Braced Wing Configuration.” [PowerPoint Slides] Available: https://www.utias.utoronto.ca/wp-content/uploads/2017/09/Potter-Strut_Braced_Wing.pdf [Accessed: 13-Feb-2023]

[13] F. H. Gern, A. H. Naghshineh-Pour, E. Sulaeman, R. K. Kapania, and R. T. Haftka, “Structural wing sizing for multidisciplinary design optimization of a strut-braced wing,” Journal of Aircraft, vol. 38, no. 1, pp. 154–163, 2001.

[14] M. K. Bradley and C. K. Droney, “Subsonic Ultra Green Aircraft Research: Phase II – Volume II – Hybrid Electric Design Exploration .”

[15] “Investigation of a strut-braced wing configuration for future Commercial Transport” [Online]. Available: https://www.researchgate.net/publication/256842181_Investigation_Of_A_Strut-Braced_Wing_Configuration_For_Future_Commercial_Transport. [Accessed: 09-Feb-2023].

[16] “CS-25,” EASA, 18-Dec-2008. [Online]. Available: https://www.easa.europa.eu/en/document-library/certification-specifications/cs-25. [Accessed: 09-Feb-2023].

[17] “Advisory and rulemaking committees,” Advisory and Rulemaking Committees – Transport Airplane Crashworthiness and Ditching Working Group Recommendation Report, 20-Sep-2011. [Online]. Available: https://www.faa.gov/regulations_policies/rulemaking/committees/ documents/index.cfm/document/information/documentID/3743. [Accessed: 08-Mar-2023].

[18] A. Abramowitz , T. G. Smith , T. Vu , and J. Zvanya , “William J. Hughes Technical Center | Federal Aviation AdministrationVertical Drop Test of an ATR 42-300 Airplane,” Vertical Drop Test of an ATR 42-300 Airplane. [Online]. Available: http://www.tc.faa.gov/its/worldpac/techrpt/ar0556.pdf. [Accessed: 08-Mar-2023].

[19] A. Abramowitz, “Vertical drop test of a shorts 3-30 airplane - FAA fire safety.” [Online]. Available: https://www.fire.tc.faa.gov/2001Conference/files/ CrashAirframeStructure/AAbramowitzSLIDE.pdf. [Accessed: 08-Mar-2023].

[20] O. Gur, J. A. Schetz, and W. H. Mason, “Aerodynamic considerations in the design of truss-braced-wing aircraft,” Journal of Aircraft, vol. 48, no. 3, pp. 919–939, 2011.

[21] J. M. Grasmeyer, “Multidisciplinary design optimization of a strut-braced wing aircraft with Tip-Mounted Engines,” thesis, Virginia Tech, 1998.

[22] N. R. Secco and J. R. Martins, "Rans-based aerodynamic shape optimization of a strut-braced wing with overset meshes", Journal of Aircraft, vol. 56, no. 1, pp. 217–227, 2019.

[23] H. Gagnon and D. W. Zingg, "Euler-equation-based drag minimization of unconventional aircraft configurations" Journal of Aircraft, vol. 53, no. 5, pp. 1361–1371, 2016.

[24] A. Variyar, T. D. Economon, and J. J. Alonso, "Multifidelity conceptual design and optimization of strut-braced wing aircraft using physics based methods" 54th AIAA Aerospace Sciences Meeting, 2016.

[25] M. Drela, H. Youngren, "XFOIL", Software Package, Version 6.99. [Online]. Available: https://web.mit.edu/drela/Public/web/xfoil/ [Accessed: 21-Feb-2023].

[26] M. Drela, H. Youngren, "AVL", Software Package, Version 3.40b. [Online]. Available: http://web.mit.edu/drela/Public/web/avl/ [Accessed: 21-Feb-2023].

[27] SciPy, "Fundamental algorithms for scientific computing in Python", Version 1.10.1. [Online]. Available: https://scipy.org/ [Accessed: 21-Feb-2023]

[28] Python Software Foundation, "Python", Software Package, Version 3.9.16. [Online]. Available: https://www.python.org/ [Accessed: 21-Feb-2023].

[29] Lars Davidson, Fluid mechanics, turbulent flow and turbulence modeling, Course material for TME226 Mechanics of Fluids and MTF271 Turbulence Modeling at Chalmers University of Technology. [Online]. Available: https://www.tfd.chalmers.se/ lada/postscript_files/solids-and-fluids_turbulent-flow_turbulence-modelling.pdf

[30] J. D. Anderson, Fundamentals of aerodynamics. New York, NY: McGraw-Hill Education, 2017.

[31] P. Miltén and C. Svensson, "Design and evaluation of UAV system to support naval search and rescue - Full design cycle of blended wing body unmanned aerial vehicle, ranging from initial sizing to windtunnel evaluation," thesis, 2022.

[32] XFLR5, Documentation, theoretical background, XFLR5 lecture notes. [Online]. Available: http://www.xflr5.tech/xflr5

[33] J. D. Anderson, Modern compressible flow: with historical perspective. McGraw Hill Education, 2021, isbn: 9781260570823

[34] A. JOHANSSON, "Aerodynamic Databank Modeling for Development of a Short-Haul Electric Airliner," thesis, 2022.

[35] "OpenVSP", Software Package, Version 3.31.1. [Online]. Available: http://openvsp.org/ [Accessed: 21-Feb-2023].

[36] Vortex-lattice utilization, Hampton, VA, USA, 1976. Accessed: May 3 2022. [Online]. Available: https://ntrs.nasa.gov/api/citations/19760021075/ downloads/19760021075.pdf.

[37] M. Drela, Flight vehicle aerodynamics. Cambrdge, MA: MIT Press, 2014.

[38] F. Yu, J. Bartaseviciusand M. Hornung, "COMPARING POTENTIAL FLOW SOLVERS FOR AERODYNAMIC CHARACTERISTICS ESTIMATION OF THE T-FLEX UAV". figshare, 01-Dec-2022, doi: 10.6084/m9.figshare.21656960.v1.

[39] S. Gudmundsson, "General Aviation Aircraft Design", Second Edition, Reston: Butterworth-Heinemann, 2021.

[40] M. Drela, "XFOIL: An analysis and design system for low Reynolds number airfoils," Lecture Notes in Engineering, pp. 1–12, 1989.

[41] D. P. Raymer, "Aircraft design: A conceptual approach", Reston: American Institute of Aeronautics and Astronautics, 2021.

[42] L. Liu and X. Yu, "A study on aerodynamic interference for truss braced wing configuration," Proceedings of the International Conference on Aerospace System Science and Engineering 2020, pp. 129–152, 2021.

[43] M. H. Sadraey, Aircraft Design: A Systems Engineering Approach. John Wiley & Sons, 2013.

[44] Definition of Streamlines. NASA Glenn Research Center, Accessed on: April 24, 2023. [Online]. Available: https://www1.grc.nasa.gov/beginners-guide-to-aeronautics/definition-of-streamlines/

[45] S. F. Hoerner, Fluid-Dynamic Drag: Practical Information on Aerodynamic Drag and Hydrodynamic Resistance, 2nd ed. New York: Hoerner Fluid Dynamics, 1965.

[46] B. W. McCormick, Aerodynamics, Aeronautics, and Flight Mechanics, 2nd ed. New York: John Wiley & Sons, Inc., 1979, p. 24. ISBN 0-471-03032-5.

[47] S. Boyd and L. Vandenberghe, Convex Optimization, Cambridge: Cambridge University Press, 2004.

[48] N. Andréasson, A. Evgrafov, and M. Patriksson, An Introduction to Optimization: Foundations and Fundamental Algorithms, 3rd ed. London: Dover Publications, 2020.

[49] M. Wahde, Biologically Inspired Optimization Methods: An Introduction, WIT Press, 2008. [Online]. Available: 10.2495/978-1-84564-344-7.

[50] M. Bierlaire, Optimization: Principles and Algorithms, 2nd ed. EPFL Press, 2018. [Online]. Available: https://transp-or.epfl.ch/books/optimization/html/

[51] M.D. McKay, R.J. Beckman, and W.J. Conover, "A Comparison of Three Methods for Selecting Values of Input Variables in the Analysis of Output from a Computer Code," Technometrics, vol. 21, no. 2, pp. 239-245, May 1979, doi: 10.2307/1268522.

[52] A. Olsson, G. Sandberg, and O. Dahlblom, "On Latin hypercube sampling for structural reliability analysis," Structural Safety, vol. 25, no. 1, pp. 47-56, Jan. 2003, doi: 10.1016/S0167-4730(02)00039-5.

[53] Z. Liang, G. Zheng, and J. Li, “Automatic parking path optimization based on bezier curve fitting,” 2012 IEEE International Conference on Automation and Logistics, 2012.

[54] I. H. Abbott, A. E. Von Doenhoff, Theory of Wing Sections, Dover edition. Dover Publications Inc., 1959.

[55] SIEMENS, "Simcenter STAR-CCM+", Software Package, Version 2022.1.1, Available: https://plm.sw.siemens.com/en-US/simcenter/fluids-thermal-simulation/star-ccm/ [Accessed: 21-Feb-2023].

[56] "pyDOE: The experimental design package for python", Version 0.3.8. [Online]. Available: https://pythonhosted.org/pyDOE/ [Accessed: 28-Apr-2023].

[57] “Scipy.optimize.nonlinearconstraint” scipy.optimize.NonlinearConstraint - SciPy v1.10.1 Manual. [Online]. Available: https://docs.scipy.org/doc/scipy/reference/generated/scipy.optimize.NonlinearConstraint.html. [Accessed: 26-Apr-2023].

[58] G. P. Chiozzotto, “Wing weight estimation in conceptual design: A method for strut-braced wings considering static aeroelastic effects,” CEAS Aeronautical Journal, vol. 7, no. 3, pp. 499–519, 2016.

[59] C. Ladson, "Effects of independent variation of Mach and Reynolds numbers on the low-speed aerodynamic characteristics of the NACA 0012 airfoil section", NASA Langley Research Center, USA, Virginia, Hampton, NASA Technical Memorandum 4074 Available: https://ntrs.nasa.gov/citations/19880019495 [Accessed: 04-May-2023].

[60] " 2D NACA 0012 airfoil validation," NASA. [Online]. Available: *https : //turbmodels.larc.nasa.gov/naca*0012$_v$*al.html*.[*Accessed* : 04 − *May* − 2023].

[61] Munk, M. M. (n.d.). The minimum induced drag of aerofoils - NASA technical reports server (NTRS). NASA. Retrieved March 16, 2023, from https://ntrs.nasa.gov/search.jsp?R=19930091456

[62] M. Niță and D. Scholz, "Estimating the Oswald factor from basic aircraft geometrical parameters," Semantic Scholar, https://www.semanticscholar.org/paper/Estimating-the-Oswald-Factor-from-Basic-Aircraft-Ni%C8%9B%C4%83-Scholz/58fa4289901bf976f75b5d04962cd5388a4d170f (accessed May 26, 2023).

A

Appendix 1

A.1 Mesh dependency study

Table A.1: Mesh dependency table for Trapezoidal Wing

$\mathbf{N_{chord}}$	$\mathbf{N_{span}}$	#	$\mathbf{C_L}$ [-]	$\mathbf{C_{D_{ff}}}$ [-]	$\mathbf{C_{D_{ff}}}$ [Drag counts]	**e** [-]
5	40	200	0.8	0.0146889	146.889	1.0128
20	40	800	0.8	0.0146893	146.893	1.0128
10	20-15-10-5-5-5...	1450	0.8	0.0150674	150.674	0.9875
20	140	2800	0.8	0.0149633	149.633	0.9944
20	20-15-10-5-5-5...	2900	0.8	0.0150675	150.675	0.9875
40	100	4000	0.8	0.0149198	149.198	0.9972
30	20-15-10-5-5-5...	4350	0.8	0.0149657	149.657	0.9942
50	100	5000	0.8	0.0149198	149.198	0.9972
30	25-20-15-5-5-5..	5100	0.8	0.0149716	149.716	0.9938
30	30-20-15-5-5-5...	5250	0.8	0.0149724	149.724	0.9937
30	25-20-20-5-5-5...	5400	0.8	0.0149727	149.727	0.9937
40	140	5600	0.8	0.0149633	149.633	0.9943

Table A.2: Mesh dependency table for Elliptical Wing

$\mathbf{N_{chord}}$	$\mathbf{N_{span}}$	#	$\mathbf{C_L}$ [-]	$\mathbf{C_{D_{ff}}}$ [-]	$\mathbf{C_{D_{ff}}}$ [Drag counts]	**e** [-]
40	140	5600	0.8	0.0150636	147.064	0.9878
50	100	5000	0.8	0.0150166	146.594	0.9909
30	20-15-10-5-5-5...	4350	0.8	0.0150676	147.104	0.9875
40	100	4000	0.8	0.0149198	145.626	0.9972
20	20-15-10-5-5-5...	2900	0.8	0.0150675	147.103	0.9875
20	140	2800	0.8	0.0150636	147.064	0.9878
10	20-15-10-5-5-5...	1450	0.8	0.0150674	147.102	0.9875
20	40	800	0.8	0.0147681	144.109	1.0074
5	40	200	0.8	0.0147679	144.107	1.0074

Table A.3: Mesh dependency table for Rectangular Wing

$\mathbf{N_{chord}}$	$\mathbf{N_{span}}$	#	$\mathbf{C_L}$ [-]	$\mathbf{C_{D_{ff}}}$ [-]	$\mathbf{C_{D_{ff}}}$ [Drag counts]	**e** [-]
40	140	5600	0.8	0.015771	157.709	0.9436
50	100	5000	0.8	0.015726	157.263	0.9463
30	20-15-10-5-5-5...	4350	0.8	0.01576	157.595	0.9443
40	100	4000	0.8	0.015726	157.263	0.9463
20	20-15-10-5-5-5...	2900	0.8	0.015759	157.594	0.9443
20	140	2800	0.8	0.015771	157.708	0.9436
10	20-15-10-5-5-5...	1450	0.8	0.015759	157.59	0.9444
20	40	800	0.8	0.015489	154.888	0.9607

Table A.4: Mesh dependency table for Strut Wing

$\mathbf{N_{chord}}$	$\mathbf{N_{span}}$	#	$\mathbf{C_L}$ [-]	$\mathbf{C_{D_{ff}}}$ [-]	$\mathbf{C_{D_{ff}}}$ [Drag counts]	$\mathbf{C_{D_i}}$ [Drag counts]
20	60	1200	0.8	0.015619	156.191	30
10	60	600	0.8	0.015619	156.191	30
20	10	200	0.8	0.01554	155.404	30
5	10	50	0.8	0.015529	155.286	30

A.2 Tool comparison dC_P graphs

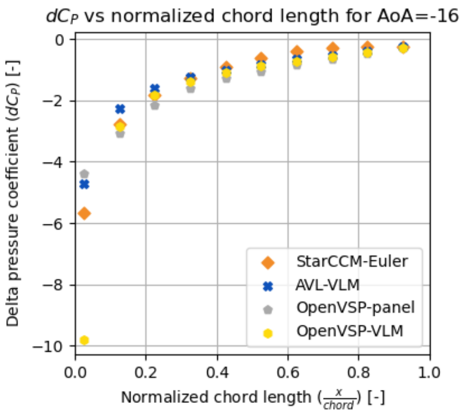

Figure A.1: dCp for different tools

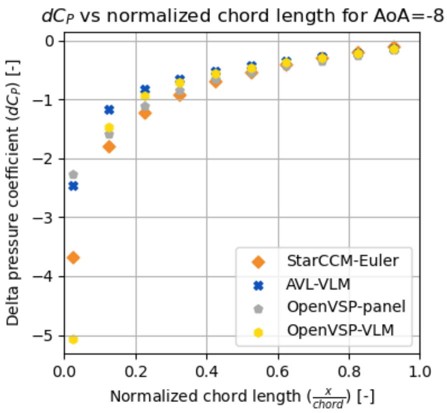

Figure A.2: dCp for different tools

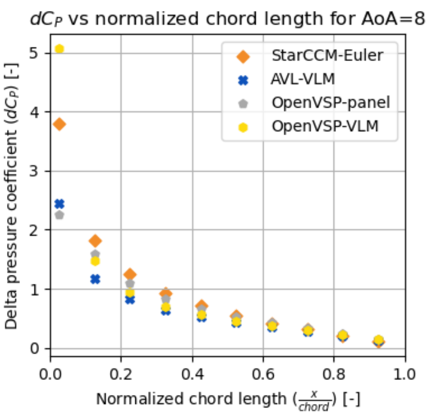

Figure A.3: dCp for different tools

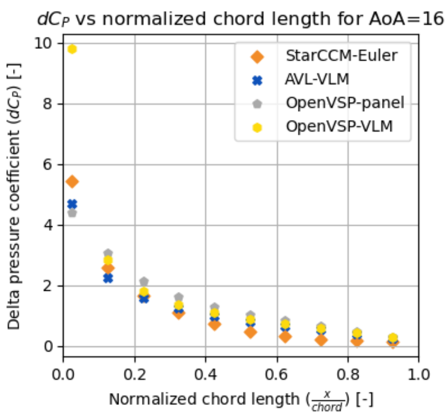

Figure A.4: dCp for different tools

A.3 Strut dihedral and local AoA influence

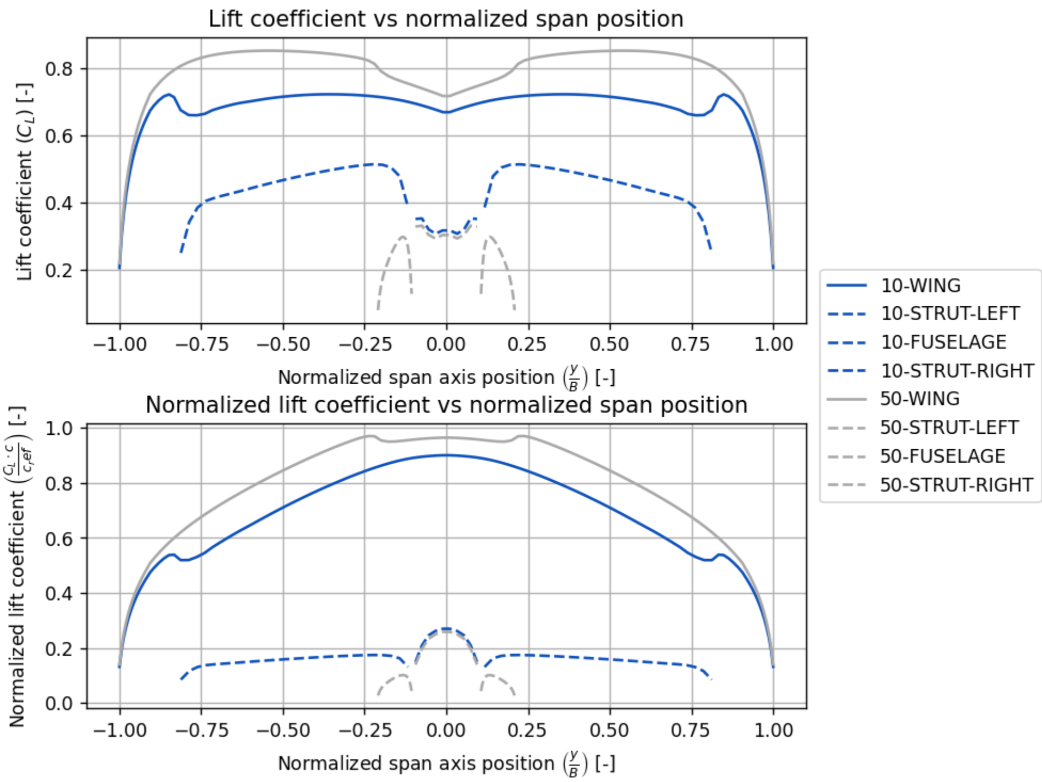

Figure A.5: Lift distribution when the dihedral angle of the strut is 10 and 50 degrees for the case $C_L = 0.8$

A.4 Further discussion about Oswald efficiency

This section presents various methodologies used to calculate the Oswald efficiency and compares them with the results obtained from AVL.

Raymer Oswald efficiency estimation for the straight wing is given in [39, Equation A.1].

$$e = 1.78\left(1 - 0.045AR^{0.68}\right) - 0.64 \tag{A.1}$$

Where AR is the aspect ratio.

Gudmundsson Lifting line theory estimation of Oswald efficiency is given in [39, Equation A.2].

$$e = 1/(1 + \delta) \tag{A.2}$$

Where δ is the induced drag factor.

The induced drag factor is defined in Figure A.6.

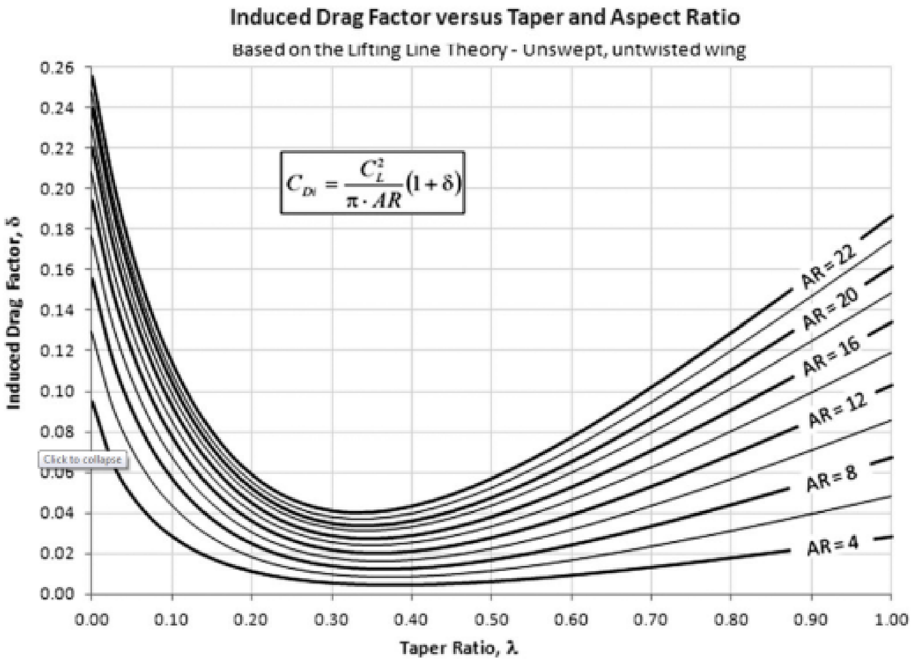

Figure A.6: Induced drag factor [39]

Brandt's estimation of Oswald efficiency is given in [39, Equation A.3].

$$e = \frac{2}{2 - AR + \sqrt{4 + AR^2\left(1 + \tan^2 \wedge_{t\,\max}\right)}} \tag{A.3}$$

Where AR is the aspect ratio, $\wedge_{t\,\max}$) is the sweep angle at the maximum wing thickness line (degree).

The results of the different methodologies to estimate the Oswald efficiency are given in Table A.5.

Table A.5: Oswald efficiency estimation for different Wings and methodologies

Property	**Case 1**	**Case 2**	$\Delta_{\mathbf{Case1-Case2}}$ [%]
Span [m]	39.55	27.92	-
AR [-]	20	10	-
λ [-]	0.2	0.7	-
δ (induced drag factor) [-]	0.055	0.04	-
e (Raymer A.1) [-]	0.526	0.757	-43.907
e (LLT A.2) [-]	0.948	0.962	-1.442
e (Brandt A.3) [-]	0.952	0.910	4.472
e (AVL) [-]	0.966	0.990	-2.453
Δe LLT - AVL [%]	**1.877**	**2.845**	-
Δe Brandt - AVL [%]	**1.398**	**8.063**	-

In Table A.5, it is evident that the Raymer equation yields different results compared to the other three methods, primarily due to its omission of the taper ratio effect. The Lifting Line Theory (LLT), Brandt, and AVL methods exhibit similar absolute values, with Brandt showing more discrepancies as the aspect ratio decreases, also due to the exclusion of the taper ratio effect. The most closely aligned methodologies are LLT and AVL, with a percentage difference of 1-3% and only a 1% variation between cases. Although AVL still produces higher results compared to LLT, this consistency can be considered in line with LLT. Additionally, it is worth noting that LLT accounts for the effect of the taper ratio, as demonstrated in Figure A.6. A further comparison with different methodologies and proposals for Oswald efficiency estimation can be found in [62].

DEPARTMENT OF SOME SUBJECT OR TECHNOLOGY
CHALMERS UNIVERSITY OF TECHNOLOGY
Gothenburg, Sweden
www.chalmers.se

AVANCEZ
1829
CHALMERS
UNIVERSITY OF TECHNOLOGY